The Key Laboratory of Weak Light Nonlinear Photonics,
Ministry of Education

Annual Report 2008

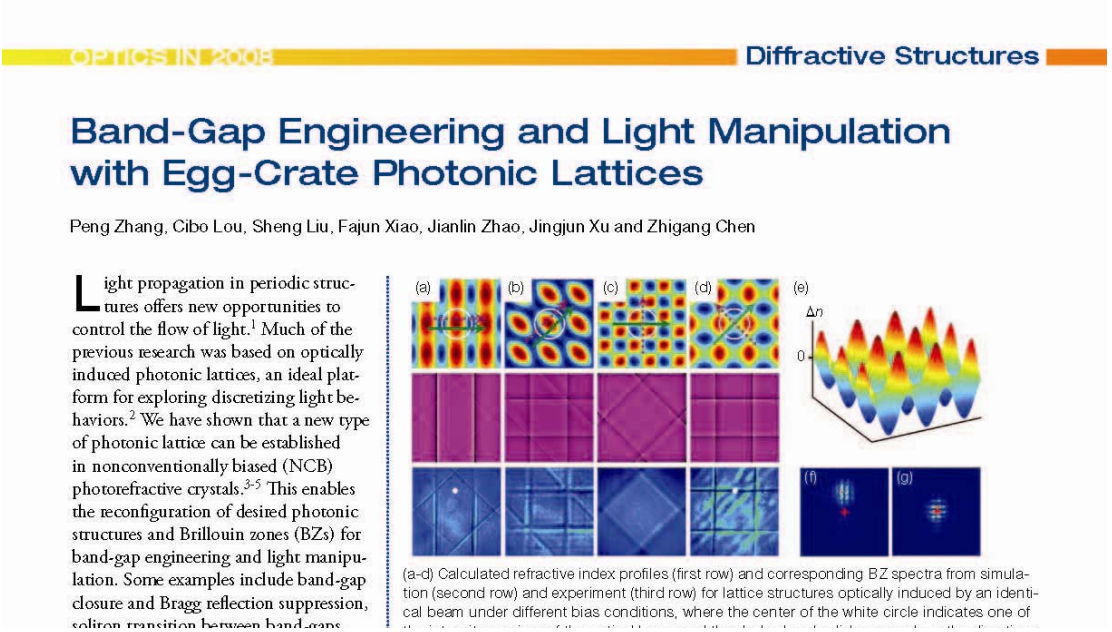

OPTICS IN 2008 Diffractive Structures

Band-Gap Engineering and Light Manipulation with Egg-Crate Photonic Lattices

Peng Zhang, Cibo Lou, Sheng Liu, Fajun Xiao, Jianlin Zhao, Jingjun Xu and Zhigang Chen

Light propagation in periodic structures offers new opportunities to control the flow of light.[1] Much of the previous research was based on optically induced photonic lattices, an ideal platform for exploring discretizing light behaviors.[2] We have shown that a new type of photonic lattice can be established in nonconventionally biased (NCB) photorefractive crystals.[3-5] This enables the reconfiguration of desired photonic structures and Brillouin zones (BZs) for band-gap engineering and light manipulation. Some examples include band-gap closure and Bragg reflection suppression, soliton transition between band-gaps

(a-d) Calculated refractive index profiles (first row) and corresponding BZ spectra from simulation (second row) and experiment (third row) for lattice structures optically induced by an identical beam under different bias conditions, where the center of the white circle indicates one of

南开大学弱光非线性光子学

教育部重点实验室

Annual Report 2008

The Key Laboratory of Weak Light Nonlinear Photonics,
Ministry of Education

南开大学弱光非线性光子学

教育部重点实验室

“2007 中国光学重要成果”发布会在上海隆重召开，楼慈波、许京军、陈志刚等发表在 *Physics Review Letters* 上的关于“光诱导光子晶格中非线性空间频谱整形和带隙孤子串的实现”的工作名列其中。

◀▼科技部副部长曹建林等颁奖嘉宾为获奖代表颁奖，楼慈波博士（左图中）代表研究小组参加了颁奖仪式并做学术报告。

（2008.3.18）

▼ 2008 discrete optics workshop 在泰达应用物理学院举行。

（2008.6.12-13）

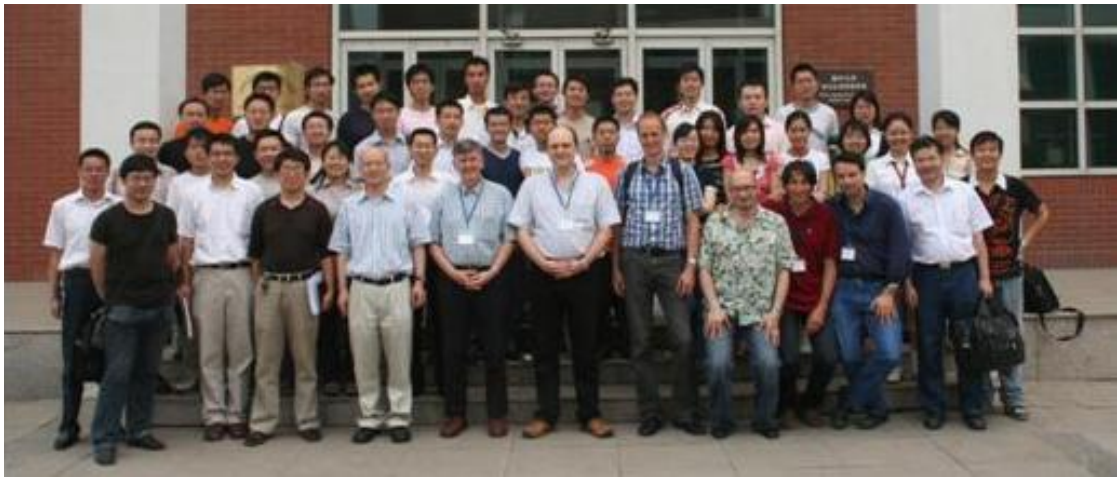

▼ 第十四届全国凝聚态光学性质学术会议合影。

（2008.7.24-27）

▼ 由国家自然科学基金委主办，南开大学承办的《先进光子学材料与技术讲习班》在泰达应用物理学院举行。许京军副校长出席了开学仪式并致欢迎辞，来自国内外的十九位专家进行了授课并与学员进行了热烈的讨论。

（2008.7.27-8.8）

◀ 斯洛文尼亚 Stefan 研究所 Miha Devetak 博士来访。

（2008.8.26-9.5）

▶▼ 法国梅兹大学 Germano Montemezzani 教授来访并做学术报告。

（2008.10.2-10）

◀ 美国俄克拉荷马州立大学 Daniel R. Grischkowsky 教授访问我院并做学术报告。

（2008.10.31）

▶ 瑞士苏黎世联邦工业大学（ETH）Peter Gunter 教授访问我院，并做了题为：“Highly Integrated Optics”的学术报告。

（2008.11.2-7）

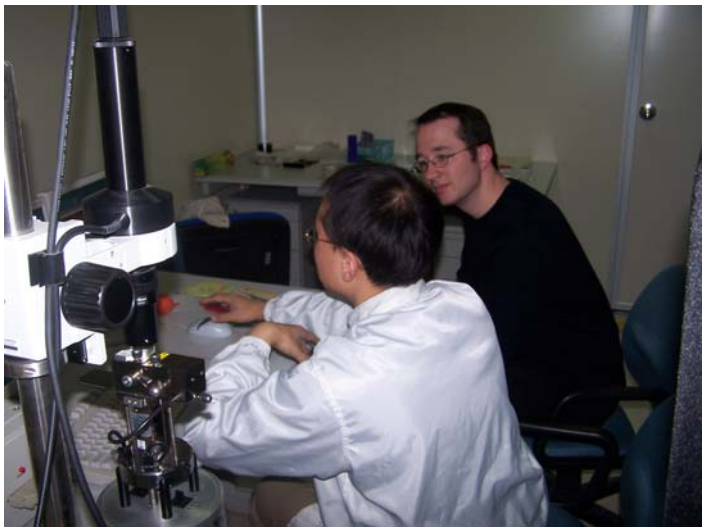

◀ 德国 Clausthal 工业大学 Christian Erwin Rüeter 博士来我院进行合作研究

（2008.11.17-23）

前　言/Preface

In 2008, the work at our lab was mainly focused on photonics materials and advanced fabrication techniques, weak-light nonlinear optics and quantum coherent optics, spectral characterization and sensing technology, nonlinear physics and new photonics devices, semiconductor quantum photonics materials and devices. In this report, we present a short summary of the results achieved in each line of activity of 2008.

All the activities summarised here have been done in the frame of international projects, cooperation agreements, and contracts with NSFC, MOE, MOST and Tianjin Municipal government. Without their supports, the progress in our research and education will never occur. Thank all these sponsors for their strong supports.

In addition, our staff and students spent some of their sleeping hours besides their waking hours on their research work and often made personal sacrifices in order to make our research better and faster. Thank you for your contributions to our own lab due to your wonderful research works.

We also benefit a lot from our colleagues from other units all over world, who provide us advices and supports. Many thanks.

Even though this preface is routine and has no big change as before, here I would like to stresss that actually our research work has been not going along well in 2008 and was a bit frustrated in our main stream. Also our hard-working tradition could not be well kept and developed, maybe due to the world-finance storm. I DO hope that we can keep on our good tradition and come on in 2009. And we are confident that we can catch up and will achieve more in 2009.

Prof. Dr. Jingjun Xu 

Director,

The Key laboratory of Weak-Light Nonlinear Photonics

目　录/Contents

人员结构/Organization

实验室主任/Director

许京军　教　授

实验室副主任/Deputy Directors

张国权　教　授

孙　骞　教　授

学术秘书/Academical Secretary

禹宣伊　副教授

研究方向负责人/Research Group Leaders

弱光非线性及量子相干光学	许京军　教　授
非线性物理与光子技术	田建国　教　授
光子学材料及先进制备技术	孔勇发　教　授
光谱表征及传感技术	臧维平　教　授
半导体生长技术和半导体器件	舒永春　教　授

学术委员会/Academic Committee

主　任/Chairman

王占国　院　士

委　员/ Committee Members

沈德忠　院　士

薛其坤　院　士

姚建年　院　士

陈志刚　教　授

龚旗煌　教　授

陆　卫　研究员

田建国　教　授

王慧田　教　授

徐现刚　教　授

许京军　教　授

许宁生　教　授

资　剑　教　授

外籍学术顾问委员

D. Kip	教　授	德国 Cauthburge 大学
L. Hessenlink	教　授	美国斯坦福大学物理系
R. A. Rupp	教　授	奥地利维也纳大学实验物理所
T. Volk	教　授	俄罗斯国家晶体研究所
Y. Tomita	教　授	日本电气通信大学

杰出人才/Intelligent Staff

教育部“长江奖励计划”特聘教授
1999　许京军
2006　陈志刚

国家杰出青年基金获得者
1998　许京军
2001　田建国

教育部“优秀青年教师资助计划”入选者
2002　张国权
2003　宋　峰

教育部“跨世纪优秀人才培养计划”入选者
1998　许京军
2000　田建国
2001　孙　骞
2002　孔勇发

教育部“新世纪优秀人才支持计划”入选者
2004　张国权
2004　宋　峰
2005　臧维平
2005　李宝会
2006　徐章程
2007　孙甲明
2008　张心正

首批新世纪百千万人才工程国家级人选
2004　田建国

国家海外青年学者合作研究基金获得者
2005　陈志刚

“天津市授衔专家”称号获得者
2005　许京军
2005　田建国

教育部“长江学者和创新团队发展计划”创新团队基金资助

弱光非线性光子学重点实验室人员名录/Name List

研究人员/Scientific Staff（40 人）

王占国　许京军　田建国　Romano A. Rupp　陈志刚　张国权　孔勇发　孙　骞　宋　峰
臧维平　舒永春　徐章程　姚江宏　赵丽娟　刘士国　张　玲　朱　箭　曹亚安　孙甲明
张天浩　李玉栋　徐晓轩　张心正　周文远　乔海军　邢晓东　禹宣伊　余　华　吴　强
孙同庆　武　莉　楼慈波　高　峰　唐柏权　刘智波　李祖斌　薄　方　王振华　齐继伟
叶　青

技术人员/Technical Staff（3 人）

黄自恒　陈绍林　马玉祥

行政人员/ administrative Staff（1 人）

梁　建

博士生/Ph.D Students（61 人）

宋道红　胡　毅　叶卓艺　郭　贺　孔凡磊　赵立华　孙立萍　郝志强　涂燕飞　刘建彬
祁轶舲　齐新元　窦宜领　许宁宁　翟召辉　潘雷霆　李　威　蔡　卫　李　俊　王　喆
边　飞　王俊俏　张学智　任梦昕　向吟啸　陈树琪　程　化　郝召锋　鄢小卿　李建威
张校亮　刘　欣　栗建兴　应翠凤　王文杰　刘富才　师丽红　张雅婷　李燕丽　曹永强
翟晓辉　王恩君　裴子栋　冯页新　董江舟　袁继翔　张新星　周凯迪　叶志诚　李俊梅
刘海旭　袁志翔　张新星　周凯迪　明成国　王青如　于晓晨　韩　琳　刘加东　施曙东
吴　限

硕士生/M.S. Students（131 人）

王慎之　钱学波　谢　楠　高光宇　胡金霞　祁国春　张文定　段长莎　辛非非　刘　泽
孙海峰　刘龙昌　李　辉　谭信辉　石　凡　金妮娜　李　建　李　祥　李海燕　陈宗强
陈子坚　郭尚雨　胡　皓　徐　燕　杨　冉　刘　泽　杨一宏　付世鹏　邢　冲　张校亮
李　行　南晓宇　惠王伟　张墨林　马雅盛　赵子宇　余　璇　梅剑春　惠王伟　杨晓玲
李亚东　徐　建　刘世松　史　烁　赵　欣　李　艳　刘博洋　李西峰　孟翔峰　何　嵩
孔祥天　阚颖慧　高洪利　寇大勇　杨　熹　韩　榕　刘张骞　马海梅　安旭东　胡　茜
窦树岗　李昕睿　陈喜杰　王磊磊　平维杰　杨　东　胡　欣　高冬子　匡元江　刘　刚
詹　鹤　周　波　崔　磊　王利忠　吕　玮　周晓东　于晓明　孙建成　季鸣元　侯春霄
宋令枝　陈　凯　曾　浩　田　甜　陈金金　杨晓丹　王海涛　韩文卿　董印锋　陈　猛
陈　鸿　田　澍　梁启锐　胡　男　陈　晨　崔　楠　罗青青　曹　雪　张威威　张新霞
杨　阳　张俊杰　王静密　程　辉　王　醉　朱鸿雁　康　培　姚惠梓　李　洁　卢志璐
王红亚　侯春霄　宋令枝　陈　凯　弭志强　郑一凡　胡　男　胡承学　张宇佳　朴文益
于　音　蔡莹莹　郭　宁　程振洲　骆兰军　曲菲菲　王文涛　赵红艳　樊学芳　李　伟
李　腾

承担课题/Projects under Researching

序号	项 目 名 称	项 目 来 源	起止时间	负责人
1	纳/微结构非线性光学、光调控与器件应用研究	973 项目	2007.5-2012.8	许京军
2	人工结构材料的能带设计、制备和效应的基础研究	973 项目	2007.7-2008.12	陈志刚
3	介观光学与新一代纳/微光子器件研究	973 项目	2007.1-2011.12	孙骞
4	硅基发光材料与光互联的基础研究（南开部分）	973 项目	2007.7-2012.12	孙甲明
5	氧化物介观薄膜原子尺度可控制备与超快紫外器件研究（南开部分）	973 项目	2007.5- 2011.4	孔勇发
6	光诱导人工光学结构及光传播特性研究	973 项目	2007.7-2011.12	陈志刚
7	光泵浦 1064nm 半导体垂直外腔表面发射激光器芯片材料的制备	863 项目	2006.12-2008.12	舒永春
8	四价掺杂铌酸锂晶体	863 新材料技术	2007.12-2010.11	孔勇发
9	基于掺镁近化学比铌酸锂的波长可调高速全光波长转换器	863 项目	2006.1-2008.12	陈云琳
10	关联光子学微结构阵列的光传输与调控研究	国家重大科学研究计划	2007.01-2011.12	田建国

11	光强与时间控制的光学图像和信息处理器件的原理及技术研究	国家自然科学基金	2006.1-2008.12	张春平
12	光感应二维非线性光子晶体及其性能的研究	国家自然科学基金	2006.1-2008.12	孔勇发
13	卟啉有机超分子激发态光学非线性研究	国家自然科学基金	2006.1-2008.12	田建国
14	高活性可见光催化剂界面光生电荷转移的原位瞬态分析	国家自然科学基金	2006.1-2008.12	曹亚安
15	980nm InGaAs 亚单层量子点激光器	国家自然科学基金	2006.1-2008.12	徐章程
16	用宽带荧光上转换飞秒时间分辨光谱技术研究 CdS 纳米体系中超快弛豫过程	国家自然科学基金	2006.1-2008.12	赵丽娟
17	基于一维光自带隙结构的光限制效应研究	国家自然科学基金	2007.1-2009.12	臧维平
18	弱关联光子晶格体系中飞秒光传播特性及其导致的非线性光学效应	国家自然科学基金	2007.1-2009.12	吴强
19	光学相干周期微结构系综的光学性质	国家自然科学基金	2007.1-2009.12	张国权
20	光折变非线性表面光波导及其应用研究	国家自然科学基金	2007.01-2009.12	张天浩
21	电场调制下纳米硅微晶和 Er 离子耦合系统的发光特性和高效率场致发光	国家自然科学基金	2008.1－2010.12	孙甲明
22	掺 Er 磷酸盐玻璃陶瓷的发光和激光特性	国家自然科学基金	2008.1－2010.12	宋峰
23	聚合物/无机量子点红外复合材料的非线性和超快光谱研究	国家自然科学基金	2008.1－2010.12	徐章程

24	Er^{3+}离子掺杂钨酸镧钾晶体的生长和性质研究	国家自然科学基金	2008.1－2010.12	孙同庆
25	有机超分子材料的光学非线性调控及其应用研究	国家自然科学基金	2008.1－2010.12	刘智波
26	非线性光学机制研究	教育部新世纪优秀人才支持计划	2006.1-2008.12	臧维平
27	近红外有机/无机量子点复合材料和器件	教育部新世纪优秀人才支持计划	2007.1-2009.12	徐章程
28	高效率的硅 MOS 电致发光器件	教育部新世纪优秀人才支持计划	2008.1-2010.12	孙甲明
29	新型激光自倍频晶体基质材料五磷酸镧二钾的生长与性质研究	教育部高等学校博士点新教师基金	2008.01-2010.12	孙同庆
30	Er 掺杂的富硅 SiO_2 MOS 结构的高效率场效应电致发光	教育部高等学校博士点新教师基金	2008.01-2010.12	孙甲明
31	新型硼酸盐发光材料结构与性能研究	教育部高等学校博士点新教师基金	2008.01-2010.12	武莉
32	有机超分子材料光学非线性研究	教育部高等学校博士点新教师基金	2008.01-2010.12	刘智波
33	亚波长结构光传播性质的研究	教育部高等学校博士点新教师基金	2008.01-2010.12	李祖斌
34	光泵浦 980nm 半导体垂直外腔表面发射激光器芯片的制备	天津市重点基金项目	2006.4-2008.12	舒永春
35	矿石检测小型化激光拉曼光谱仪	天津市科技支撑计划重点项目	2007.4－2009.10	徐晓轩
36	若干新型弱光非线性效应及其应用的研究	天津市国际科技合作项目	2006.4-2009.3	张国权

37	弱光非线性光学新效应和机制	天津市科技创新能力与环境建设平台项目	2006.7-2009.6	孙骞
38	用相位编码方法在铌酸锂表面构造亚微米金属微结构	天津市自然科学基金	2007.4-2009.9	张心正
39	长江学者启动基金	985	2006.3-2009.2	陈志刚
40	离散体系对瞬态量子相干的影响	教育部留学回国人员科研启动基金	2008.08-2009.08	张心正
41	聚合物/无机量子点红外复合材料中的载流子动力学	中科院上海技物所红外物理国家重点实验室开放课题	2007.6-2009.6	徐章程
42	微流体系光动力学的基础研究	南开大学创新基金	2007.1-2008.12	禹宣伊
43	掺锆铌酸锂晶体抗光折变性能研究	南开大学创新基金	2007.1-2008.12	刘士国
44	若干掺杂铌酸锂晶体的研制	横向课题	2008.8-2010.7	张玲

仪器设备/Facilities

仪器设备名称	规格型号	购置时间
激光器工作站	899-29	2005.09
飞秒激光器	VF-T2S	2000.08
皮秒激光器	PY61	2003.11
纳秒激光器	Panther OPO	2003.11
光纤激光器	PLY-20-M	2003.11
可调频再生放大器	Spitfire F-1K	2000.04
时间分辨光谱及瞬态吸收光谱系统	Spectrapro.300i	2000.04
光谱分析仪	AQ6315A	2005.09
显微拉曼光谱仪	MKI2000	1998.09
分子速外延生长炉	Riber Compact 21T	2003.09
提拉法晶体生长炉	研制	2002.04
晶体切割研磨抛光系统	Logitech 系列	2001.06
扫描探针显微镜	Nanoscope ⅢIa	2006.08

注：除开放基金外，所有仪器设备均为有偿使用

研究工作报告/Scientific Report

非线性物理与光子技术/ Nonlinear Physics and Photonics Techniques

负责人：田建国

本方向涉及有机材料光学非线性、亚波长微结构、生物光子学、以及非线性表面波等方面。本年度发表论文 9 篇；申请发明专利 7 项。在研课题经费 424.38 万元。2008 年度“非线性物理与光子技术”方向主要在以下方面取得了进展：

In this field, we mainly focused on optical nonlinearities of organic materials, sub-wavelength microstructure, bio-photonics, and nonlinear surface waves. 9 papers have been published in international academic journals, and 7 patents applicanted. The total reasearching founds are 4.2438 millions. This year, we obtained some important results as following:

在有机材料光学非线性方面，我们在卟啉修饰碳纳米管和卟啉修饰石墨烯的光限制效应研究的研究中，取得了较大的进展，我们对三种不同卟啉共价连接修饰的碳纳米管和卟啉直连石墨烯结构的光限制效应进行了研究，发现卟啉修饰后的碳纳米管和石墨烯的光限制效应有较大提高，如图 1 和图 2。通过对这三种卟啉修饰碳纳米管和卟啉修饰石墨烯结构的紫外吸收和荧光特性的研究，我们认为光限制效应的提高除了反饱和吸收和非线性散射两种光限制机制的结合外，还可能有来自卟啉与碳纳米管或石墨烯之间光致电子转移效应的贡献。此外，我们对一类二苯基卟啉中心的金属化和外侧 meso 位的溴化进行了结构与光学非线性关系的研究。通过溴化和金属化可以获得非线性吸收在饱和吸收与反饱和吸收之间的转变。最后，我们研究了各项同性介质中，三阶非线性的各项性异性导致的光束偏振态和介质光学非线性的变化，非线性吸收和非线性折射的变化依赖于光束椭圆度的改变。

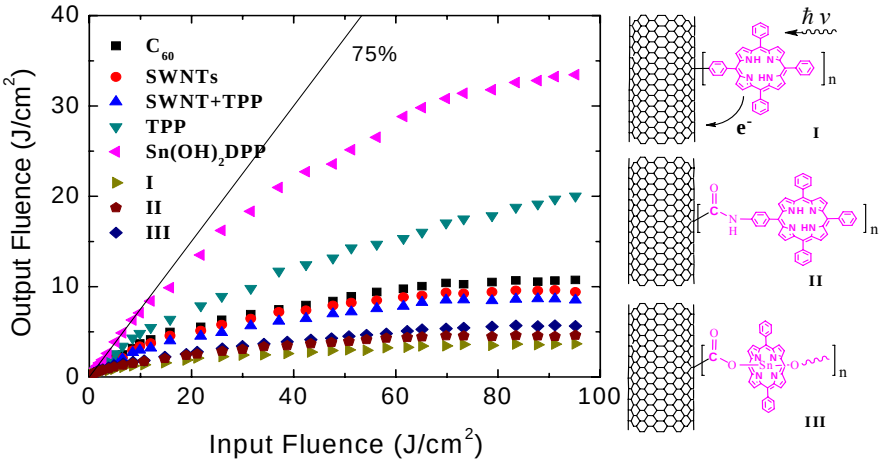

图 1 卟啉修饰单壁碳纳米管的光限制效应

Fig. 1 Optical limiting of porphyrin-SWNT supramolecular system

Optical nonlinearities of organic materials, such as porphyrin, graphene, have been measured. Firstly, in the studies of porphyrin-SWNT and porphyrin-Graphene supramolecular system, three kinds of the porphyrins covalently functionalized SWNTs and Graphene offered superior performance to C60, the individual SWNT/ or Graphene and porphyrins by combination of

nonlinear mechanism of reverse saturable absorption and nonlinear scattering, and the photoinduced electron or energy transfer between porphyrin moiety and SWNT (or Graphene) also play an important role in improvements of optical limiting effect. Secondly, Nonlinear refraction and nonlinear absorption of diphenylporphyrins with bromination and metallization were studied by Z-scan technique. Results show that both metallization and bromination of diphenylporphyrins can cause the regular change of magnitude and sign of nonlinear absorption. The transition between saturable absorption and reverse saturable absorption happens as bromine increases and metal ion changes. The evolutions of polarization and nonlinearities in an isotropic medium induced by anisotropy of third-order nonlinear susceptibility were studied experimentally and theoretically. The changes of nonlinear refraction and nonlinear absorption depending upon the ellipticity of polarization ellipse are also presented.

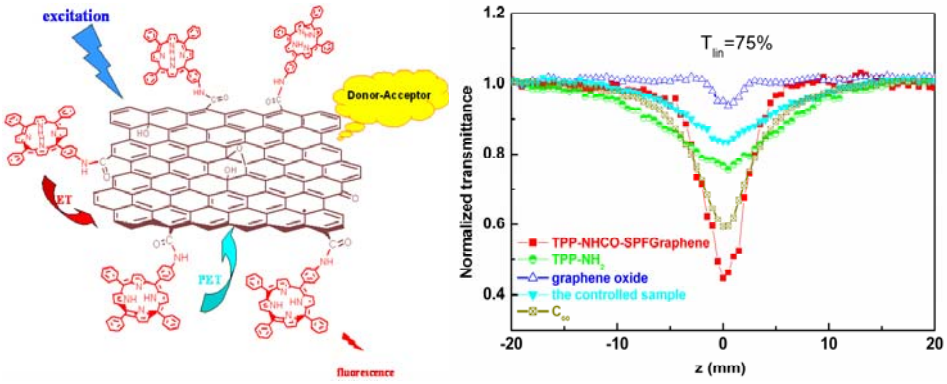

图 2 卟啉修饰石墨烯的光限制效应

Fig. 2 Optical limiting of porphyrin-Graphene supramolecular system

在一维带隙材料光束传播方面，我们提出了一种新的数值计算方法。对于基于一维带隙材料的应用研究，通常需要对麦克斯韦方程直接求解。常用方法为时域有限差分的方法，因为有限差分是一个显格式技术，它的时间步长受 CFL 稳定条件限制。基于 Pade 近似和多步法，我们给出一个高阶无条件稳定隐格式算法。甚至对于大的时间步长，数值色散和耗散也可以保持相当小。同时，我们提出了一个新的分析一维非线性光子带隙材料 Z-scan 理论。计算结果表明对于非线性折射的带隙材料，其表现类似于一个同时具有非线性折射和吸收的体材料。缺陷材料的 z-scan 特性主要来自于缺陷模的非线性。

For application of one dimensional photon crystal, we need to solve the Maxwell's equations. The well-known class of algorithms to solve Maxwell's equation is base on the finite-difference time-domain method.Since the FDTD method is an explicit scheme, its time step is limited by CFL. We present an implicit high-order unconditionally stable complex envelope algorithm to solve the TDME based on the Pade approximation and multistep method. Even for large steps the numerical dispersion and dissipation remain very small. Meanwhile, We propose a novel Z-scan theory for one-dimensional nonlinear photonic band gap materials also. Results show that the Z-scan curves for photonic band gap materials with nonlinear refraction are similar with those of the uniform materials with nonlinear refraction and nonlinear absorption simultaneously. The nonlinear optical properties of the defect material are the main contribution to the Z-scan results near the defect mode frequency.

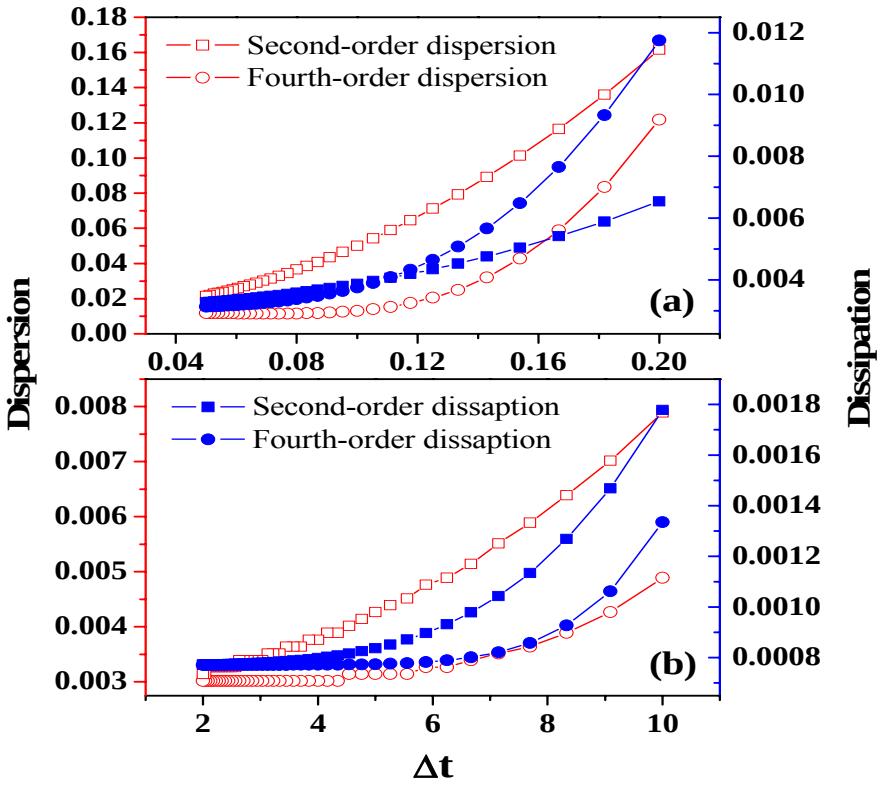

图 3、不同阶情况下的数值色散和耗散。（a）Kole 的方案，（b）我们的方案。

Fig 3. Numerical dispersion and dissipation error in different orders in time, (a) Kole' method, (b) our scheme.

在亚波长微结构的增透特性方面，我们研究了亚波长狭缝在电介质结构离开金属表面时的增强透射现象。电介质结构激发的表面等离子体与入射光共振导致透射的增强，当电介质结构离开或接触表面时，由于不同表面波的作用得到了不同波长下的透射峰。我们讨论了这两种情况下增强透射的异同。另外，将电介质结构换成金属结构得到了同样的结果。同样的电介质结构，在离开或接触金属表面时产生了完全不同的增强透射谱，这些结果可能在表面等离子体传感器方面有一定应用价值。

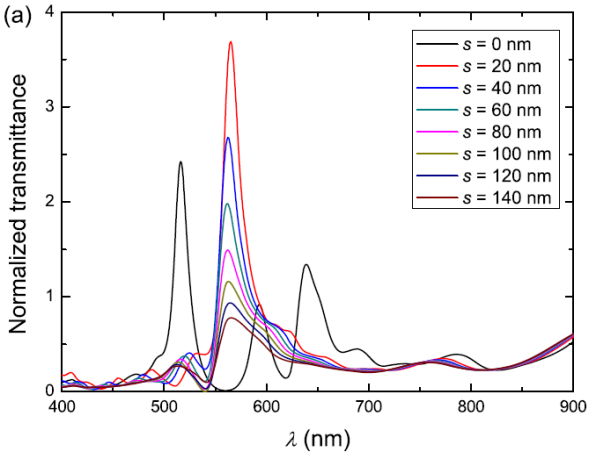

图 4 不同 s 值下的归一化透过率光谱

Fig. 4 The normalized transmission spectra as a function of s

By setting periodic dielectric bars above the incident surface of the metal film, we study the enhanced transmission through a single subwavelength slit. The surface plasmon excited by the bars is resonant with the incident light, which leads to transmission enhancement. With dielectric bars on or above the film surface, the behaviors of the surface waves excited by the bars are different, which leads to transmission peaks at different incident wavelengths. The similarities and differences of the enhancement of these two cases are discussed. In addition, we change the dielectric bars to silver and a similar enhanced transmission is obtained. With same dielectric structures on or above the metal surface, the transmission spectra through the subwavelength slit present very different properties. These results will be helpful for the applications of surface plasmon based sensors.

在生物光子学方面，我们利用双光束作用下干涉条文的强度分布研究了有机光色材料乙基红等的非线性透射特性以及光开关特性。研究了生物组织表面的粗糙度对利用表面漫反射测量和拟合获得其光学性质的影响。

In the studies of bio-photonics, using the intensity distribution of interference fringes formed by a capillary filled with transparent liquid, we measured variations in RI of ethyl red (ER) solution excited by a 535-nm-15 mW-laser, and found that the change of RI is 0.00504 and the corresponding effective index of refraction is 1.06×10-9, for which the order of magnitude is same as that measured by Z-scan. The reduced scattering and absorption coefficients of the nylon bar with different surface roughness for the smooth and rough surface of the incident region respectively were determined by a spatially resolved steady-state diffuse reflection technique.

光子学材料及先进制备技术/ Photonics Materials and Advanced Fabrication Techniques

负责人：孔勇发

本方向涉及非线性光学晶体、微晶玻璃陶瓷、光子学微结构、纳米光子学、低维功能材料等方面。本年度发表论文12篇，其中Appl. Phys. Lett. 4篇；申请发明专利3项，在研课题经费409万元。取得的代表性成果如下：

In this field, we mainly focused on the nonlinear optical crystals, micro-crystal glass ceramics, photonic microstructure, nano-photonics, and nanoparticulate films. Twelve papers were published in international academic journals, including four papers in Appl. Phys. Lett., and three patents applicanted. The total reasearching founds are more than 4 millions. This year, we obtained some important results, they are mainly shown as following:

我们发明了锆铁双掺铌酸锂晶体(LN:Fe,Zr)，在保持30%以上饱和衍射效率的同时，其光折变响应时间仅有2s，因此光折变灵敏度达到了12 cm/J以上。研究表明，当掺锆量超过阈值后，LN:Fe,Zr晶体中的$Fe^{2+/3+}$离子仍然占锂位，并没有象在LN:Fe,Mg晶体中那样改变晶格占位，因此当掺杂量超过阈值后LN:Fe,Zr晶体具有比LN:Fe,Mg晶体更高的饱和衍射效率、更快的光折变响应时间。而LN:Fe,Zr晶体具有比LN:Fe,Hf晶体更佳的光折变性能的原因是晶体中含有浓度更高的Fe^{2+}离子。该研究结果表明锆铁双掺铌酸锂晶体是一种性能优异的光折变存储材料。

表 1. 锆铁双掺铌酸锂晶体的光折变性能。入射光波长 532 nm，单束光强 250mW/cm^2。$LiNbO_3$:Fe、$LiNbO_3$:Mg,Fe 和 $LiNbO_3$:Fe,Hf 的数据作为对比也一并列出。

Table 1. Photorefractive properties of LN:Fe,Zr crystals. Incident light is at 532 nm with intensity of a single beam approximately 250mW/cm^2. The data for $LiNbO_3$:Fe, $LiNbO_3$:Mg,Fe and $LiNbO_3$:Fe,Hf crystals were also listed for comparison.

	Doping concentrations				Photorefractive properties			
Sample	Fe (wt %)	Mg (mol %)	Hf (mol %)	Zr (mol %)	η_{sat}(%)	τ_r (s)	S (cm/J)	σ_{ph} (Ω^{-1} cm^{-1})
LN:Fe	0.01				70	160		
LN:Fe,Mg_2	0.01	2			70	60		
LN:Fe,Mg_6	0.01	6			15	15		
LN:Fe,Hf_2	0.03		2		68.0	17.2	3.99	1.31×10^{-13}
LN:Fe,Hf_5	0.03		5		55.4	10.7	5.23	1.78×10^{-13}
LN:Fe,Zr_1	0.03			1	25.5	2.2	13.46	2.52×10^{-12}
LN:Fe,Zr_2	0.03			2	32.0	1.8	12.87	2.91×10^{-12}
LN:Fe,Zr_3	0.03			3	32.7	1.8	13.48	2.72×10^{-12}
LN:Fe,Zr_4	0.03			4	32.5	1.8	13.40	3.10×10^{-12}
LN:Fe,Zr_5	0.03			5	42.2	2.2	12.61	3.04×10^{-12}

在近化学计量比掺镁铌酸锂晶体中实现了周期极化反转（如Fig. 1）；研究了掺锆铌酸锂晶体周期极化反转条件，优化了工艺参数；研究了高掺锆铌酸锂晶体的相位匹配条件，在室温至230℃范围内未找到该晶体的相位匹配温度；与德国Technical University of Clausthal的Detlef Kip教授合作，完成了同成分掺铁铌酸锂晶体扩Ti波导层的表面周期极化（如Fig. 2）。

The main target is domain reversal on $LiNbO_3$ in this year. We processed the periodical domain reversal in the near-stoichiometric magnesium-doped lithium niobate crystal (as shown in Fig. 1), and studied of the zirconium-doped lithium niobate crystal polarization inversion cycle with optimizing the process parameters, and researched the highly Zirconium-doped lithium niobate crystal phase matching temperature at room temperature to 230 ºC not found within the

framework of the phase-matching crystal temperature. With the cooperation of Prof. Detlef Kip, Technical University of Clausthal in Germany, we prepared the periodical poled surface waveguide in the congruent iron-doped lithium niobate crystal with Ti indiffusion (as shown in Fig. 2).

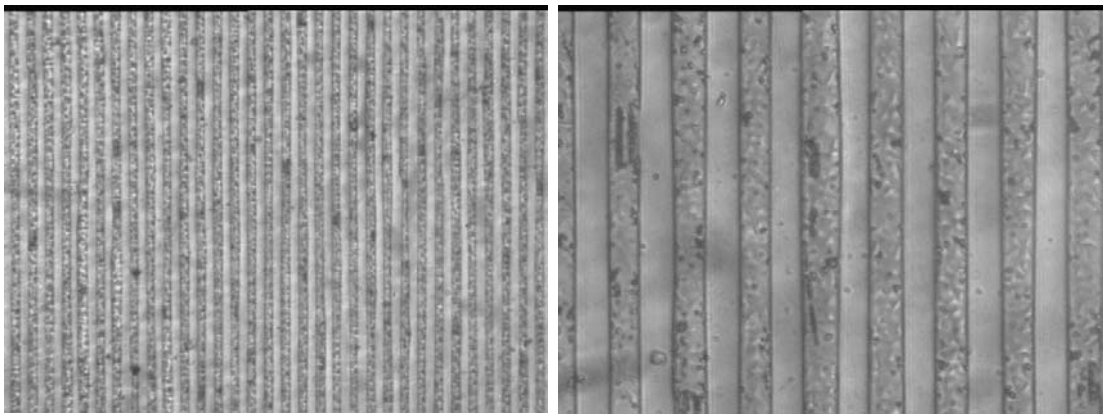

(a) (b)

图 1. 近化学计量比掺镁铌酸锂晶体的周期极化

Fig. 1 The image of periodical poled Mg:NSLN. (a)×10 object lens. (b) ×40 object lens.

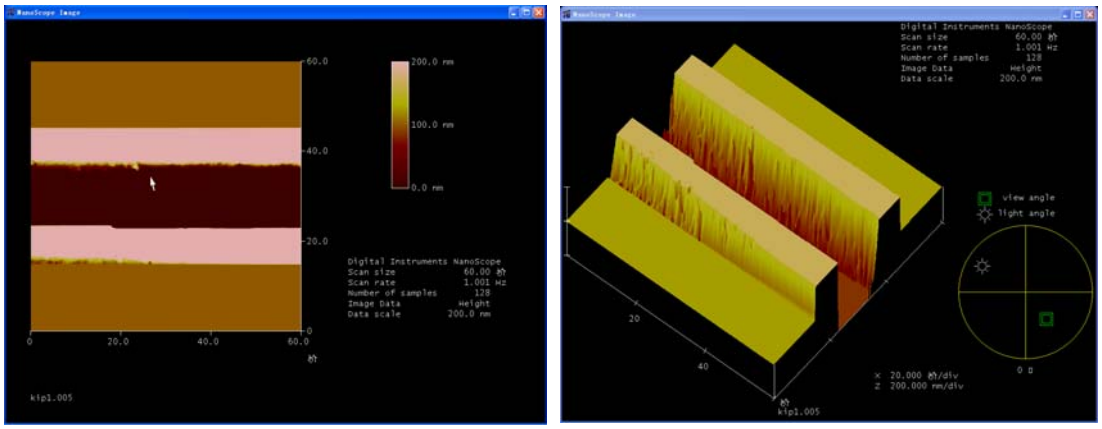

(a) (b)

图 2. 掺铁铌酸锂晶体钛扩散波导表面的周期极化

Fig. 2 The surface of periodical poled Fe:CLN with Ti indiffusion

采用提拉法生长出铒镱离子共掺的钨酸镧钾晶体，并探讨了生长工艺对晶体质量的影响。晶体吸收谱被测量，根据J-O理论计算了能级寿命、荧光分支比、强度参数、吸收截面等重要光谱参数。在975nmLD泵浦下，测量了晶体在1540nm附近处的荧光光谱和荧光衰减曲线，并计算了晶体的荧光寿命和跃迁发射截面。利用高温固相反应法合成Er^{3+}、Yb^{3+}掺杂的KLa(WO4)2粉体，研究了掺杂离子浓度对Er3+激活离子的1.55μm受激辐射强度的影响。结果表明，当Er^{3+}和Yb^{3+}掺杂浓度分别为1.5%和10%时，Er^{3+}:Yb^{3+}:$KLa(WO_4)_2$具有最大的荧光强度。同时尝试了钨酸镧钾的水热合成。

$KLa(WO_4)_2$ crystals codoped with Er^{3+}, Yb^{3+} ions have been successfully grown by CZ method in our works. The absorption spectrum of Er^{3+}:Yb^{3+}:$KLa(WO_4)_2$ crystal were measured, and spectral parameters including the absorption cross section, the lifetimes of energy levels, the

branch ratios of fluorescence and the intensity parameters have been analyzed based on the J-O theory. We measured the fluorescence spectrum near 1.5μm of Er^{3+}:Yb^{3+}:$KLa(WO_4)_2$ pumped by 975nm LD, and the fluorescence lifetime and the emission cross section were calculated. $KLa(WO_4)_2$ powders doped with Er^{3+}, Yb^{3+} have been synthesized by high temperature solid-state reaction, and the influence of doped ions concentration on the fluorescence spectra were studied. The results showed that the fluorescence emission near 1.5μm was the strongest when the concentrations of Er^{3+}, Yb^{3+} were1.5% and 10% separately. Hydrothermal synthesis of $KLa(WO_4)_2$ powders were attempted.

对新硼酸盐化合物$NaSrB_5O_9$和$Na_3SrB_5O_{10}$进行Eu离子掺杂，研究其光致发光性质。并对掺杂后样品进行结构精修，从结构变化分析其发光机理。研究发现，两个五硼酸盐特殊的结构可以在无还原气氛的条件下，稳定Eu^{2+}离子，使其替代Sr^{2+}离子在晶格中的位置。对固熔体系化合物$NaSrxBa_{4-x}B_3O_9$进行Eu^{3+}，Ce^{3+}离子掺杂，发现在x不同的情况下，色度连续改变。研究了K_2O-MgO-B_2O_3体系固相线下相关系，并用粉末从头算法对新化合物$KMgBO_3$进行了结构解析。该化合物为旋光晶体，在结构解析过程中，可直接解出两种对映异构体的结构。虽然结构炯异，该化合物与$NaMgBO_3$有一定的固熔度。由于非线性化合物$KSr_4(BO_3)_3$与同类型化合式的$NaSr_4(BO_3)_3$有截然不同的晶体结构，对$KSr_4(BO_3)_3$的K位置进行部分Na离子取代，研究其结构变化，从而深入了解化合物的形成机制，以发现新的非线性光学材料。

Photoluminescence of Eu^{3+} doped $NaSrB_5O_9$ and $Na_3SrB_5O_{10}$ were investigated, and the structures of the doped samples were refined by Rietveld method. It was found that the Eu^{2+} could be stabilized without reducing atmosphere because of the special structures of the two compounds, and the results of refinement showed that the Eu^{2+} occupied the Sr^{2+} positions. $Eu^{3+}$and Ce^{3+}doped solid solution compounds $NaSrxBa_{4-x}B_3O_9$ were studied. It was found that the red color changed continuously with variable x values. The subsolidus phase relations of K_2O-MgO-B_2O_3 were investigated by powder diffraction, and the structure of novel compound $KMgBO_3$ was solved by SDPD (Structure Determination from Powder Diffractometry) method. It is a chiral crystal. The enantiomorphous structure can be solved directly from the powder diffraction data. It was found that $KMgBO_3$ and $NaMgBO_3$ were partial soluble, even they have different structures. Because the nonlinear orthorhombic compound $KSr_4(BO_3)_3$ had a completely different structure from the cublic $NaSr_4(BO_3)_3$, series samples of $K_{1-x}Na_xSr_4(BO_3)_3$ were synthesized to study the change of the structures, in order to find novel nonlinear optical materials.

我们采用时间分辨光致发光谱技术，研究了S-K 自组织量子点与亚单层(SML)沉积的InGaAs/GaAs量子点中激子的辐射寿命。我们发现S-K 量子点体系中由于与分立的量子点态相连的连续态的存在，激子的辐射寿命在室温下超过了5.5 ns, 如图3所示。这是SK 量子点激光器增益低下的物理原因. 但是，SML量子点中激子的中心限制在2维平面上，激子的辐射寿命在90 ps 左右（图4），所以SML 量子点激光器具有高增益的特性。

The exciton radiative lifetime in SK and SML InGaAs/GaAs quantum dots (QDs) was studied by using time-resolved PL technique. We found that, due to the continuum states connected with the discrete energy levels in SK QDs, the exciton radiative lifetime is longer than 5.5 ns, as shown in Figure 3. This is the physical reason for the low gain in SK quantum dot lasers. However, the exciton radiative lifetime in SML QDs is around 90ps at 10K (Figure 4), which manifests itself in the high modal gain in SML QD lasers.

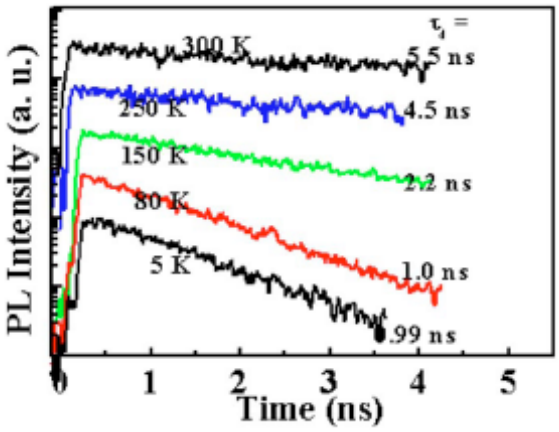

图 3. SK InGaAs/GaAs 量子点在不同温度下 PL 衰减曲线

Fig. 3 PL decays of SK InGaAs/GaAs quantum dots at different temperatures

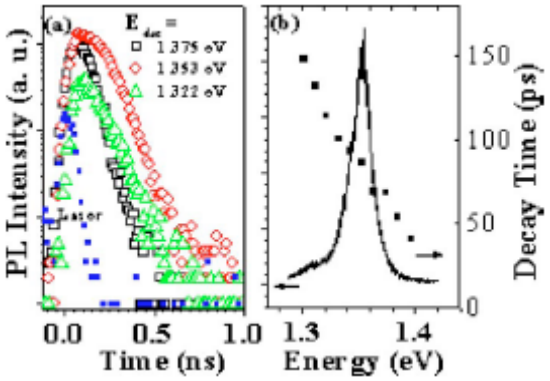

图 4. SML InGaAs/GaAs 量子点在 10 K 下的 PL 衰减曲线

Fig. 4 PL decays of SML InGaAs/GaAs quantum dots at 10 K

采用准原位PL谱技术，直接观测到了从MEH-PPV到PbS 量子点的Dexter 能量转移率随量子点尺寸的变化。实验上证明了光学禁止跃迁会影响Dexter能量转移率。

Using quasi-In-situ PL technique, we observed the size dependence of Dexter energy transfer from MEH-PPV to PbS quantum dots. The optically quasi-forbidden transitions play an important role in the rate of Dexter energy transfer.

以高活性可见光催化剂为目标，对氯苯酚为降解的目标污染物，采用溶胶-凝胶法、分步水解法和掺杂复合技术，研制出新型结构高活性WO_3/TiO_2、ZrO_2/TiO_2和 ZnO/TiO_2纳米复合薄膜催化剂和纳米结构TiO_2-Sn/TiO_2-N、SnO_2/TiO_2-N可见光催化剂，研究了催化剂的精细结构、能带结构和掺杂方式，复合界面能带结构和光生载流子转移，分析了紫外-可见光催化机理。为进一步的研制高性能、高效率纳米可见光催化剂奠定了基础。

In order to prepare TiO2 catalysts with high visible light photocatalytic activity, sol-gel method, hydrolysis step by step method and doping technology were employed to fabricate nano-WO_3/TiO_2、ZrO_2/TiO_2 ZnO/TiO_2 composite films photocatalysts, TiO_2-Sn/TiO_2-N doped and composite film photocatalysts and SnO_2/TiO_2-N doped and composite photocatalysts with high photocatalytic activity. The fine structures, energy band structures on composite interface, transfer of photogenerated carrier were investigated. The photocatalystic mechanisms under ultraviolet and visible light were discussed. This study laid a foundation for fabricating high activity and high

efficiency photocatalysts. The results was published in “Acta Chimica Sinica” and “Acta Physico-Chimica Sinica”.

采用浓碱-水热法两步预掺杂制备出In离子掺杂二氧化钛纳米管可见光催化剂。该TiO_2纳米管具有高的可见光催化活性。XRD, XPS和SPS结果表明，In离子取代晶格Ti的位置形成$In_xTi_{1-x}O_2$取代式掺杂结构，In离子的5S5P轨道与Ti离子的3d轨道形成混合价带, 使禁带变窄, 增强了可见光响应。随着In离子掺杂浓度的增加，同时在$In_xTi_{1-x}O_2$纳米管表面生成In_2O_3, 形成$In_xTi_{1-x}O_2/In_2O_3$纳米管复合结构。该复合结构有效地增加可见光响应，促进了光生载流子的分离, 提高了光生载流子在固/液界面参加光催化反应的利用率，使纳米管催化剂可见光催化活性显著提高。

In doped TiO_2 nanotubes were fabricated by concentrated alkaline hydrotherm, two steps pre-doped method. It is found that the TiO_2 nanotube with In doped exhibited high photocatalytic activity on the photocatalytic degradation of 4-chlorophenol under visible light. Based on XRD, XPS and SPS, it can be inferred that when the doped content is low, the Indium ion substitutes Ti into the TiO_2 lattice formed the $InxTi_{1-x}O_2$ structure and the In 5s5p states narrow the band gap by mixing with Ti 3d states. With the increasing of the doped content, In_2O_3 comes up on the surface of $In_xTi_{1-x}O_2$ nanotube and forms the $In_xTi_{1-x}O_2/In_2O_3$ composite structure. This composite structure efficiently enhances the visible light response, promotes photogenerated carriers separation and increases the utilization of photogenerated carriers in photocatalytic reactions at the solid/liquid interface, resulting in the higher photocatalytic activity under visible light.

利用自组装－表面沉积法，制备出CuO二维表面纳米结构薄膜(图5)。功能性实验表明，该结构具有紫外和可见光光致超疏水、超亲水转换性能(图6)。XRD结果表明，该纳米结构薄膜具有单一晶面有序生长的特点，通过SEM研究了Cu_2O到CuO的纳米结构生长过程，并分析讨论了超疏水、超亲水光致转换机理。

The CuO nano-films with 2-dimensional surface nanostructure were fabricated by self-assemble surface deposited method (Figure 5). In the functionality experiment, the transform between Superhydrophobicity and Superhydrophilicity induced by both ultraviolet and visible light were found (Figure 6). The film owned the feature of growth in order along the special crystal plane from XRD and the growth process from Cu_2O to CuO was probed by SEM. The mechanism of transform between Superhydrophobicity and Superhydrophilicity was investigated.

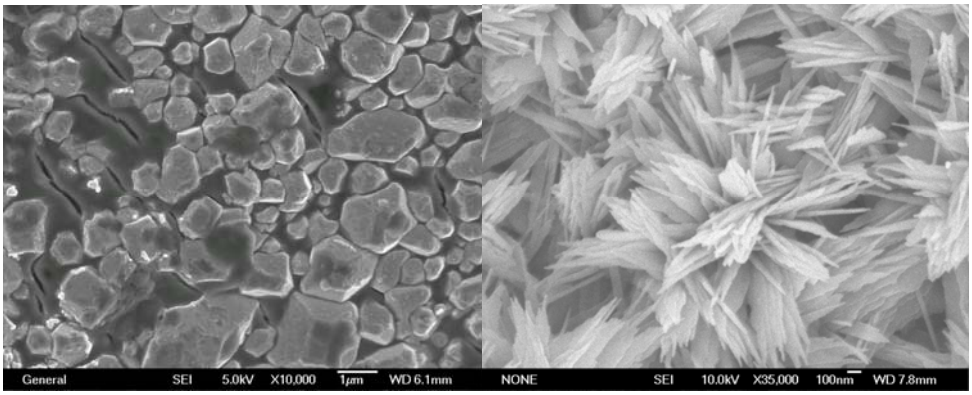

(a) (b)

图 5. (a) Cu_2O 薄膜和(b) CuO 薄膜的 SEM 照片

Fig. 5 SEM images of Cu_2O film surfaces (a) and the CuO film surfaces oxided from the Cu2O(b).

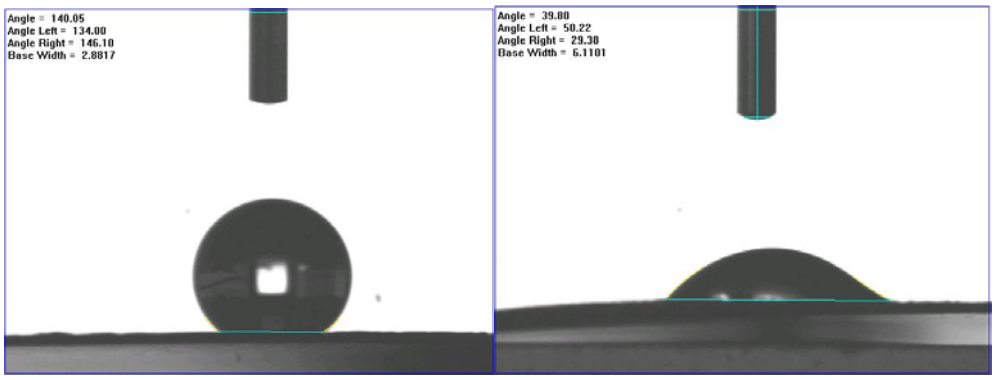

(a) (b)

图 6. 水滴在 CuO 薄膜表面的形状图，(a)光照前，(b)光照后

Fig. 6 Photographs of water droplet shape on the CuO films，(a)before (CA=140.95°) and (b) after vis-light irradiation (CA=39.80°)

弱光非线性及量子相干光学/ Weak Light Nonlinear Optics and Quantum Coherent Optics

负责人：许京军

本方向主要开展微/纳结构制备、微/纳非线性光调控、量子非线性光学与调控、飞秒超快探测技术以及光折变材料与新效应等方面的研究。2008 年度本方向共发表论文 21 篇，主要取得如下进展：

The main research topics in this group are fabrication of micro/nano-structure, nonlinear optical manipulation in micro/nano-structure, quantum nonlinear optics, ultrafast detection and analysis by using fs technology and photorefractive nonlinear optics. We published 21 papers in various academic Journals. The main research progresses in 2008 are as follows.

我们研究掺镁、掺锌和掺铟同成分铌酸锂晶体的紫外－红光双色全息存储性能，发现在掺杂浓度超过抗光折变阈值的铌酸锂晶体中，均可实现非挥发全息存储，双色记录响应时间均比单色记录时明显缩短，双色记录灵敏度大幅度提高，在掺镁 5 mol.%的晶体中可达到 1.1 cm/J。但是，在掺镁、锌样品中，深、浅能级中心上的光栅反相，而在掺铟样品中则表现为同相。这是由于掺杂离子的种类不同，在铌酸锂晶体中形成的缺陷中心也不同所引起的。

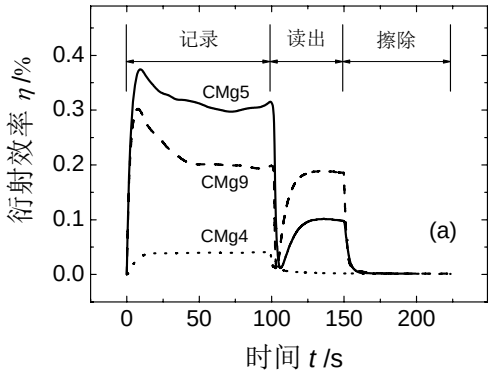

图 1. 掺镁铌酸锂晶体双色全息存储的衍射效率时间演化曲线。镁离子掺杂浓度为 5mol % (CMg5), 9 mol % (CMg9), 和 4 mol % (CMg4)。记录条件为 I_{UV}=120 mW/cm^2，I_R=I_S=122.9 mW/cm^2，Λ＝1.1 μm。

Fig. 1 The temporal evolution of the two-color holographic recording in Mg-doped lithium niobate crystals with doping concentrations of 5 mol % (CMg5), 9 mol % (CMg9), and 4 mol % (CMg4). The recording conditions are I_{UV}=120 mW/cm^2，I_R=I_S=122.9 mW/cm^2，Λ＝1.1 μm.

We studied the ultraviolet-red two-color holographic storage performances of Mg, Zn and In-doped lithium niobate crystals and found that nonvolatile holographic storage was achieved in the crystals with doping concentrations above the damage-resistant threshold value. The response times of the two-color recording was shorten as compared to that of one-color recording, and the two-color recording sensitivity was improved significantly, and was measured to be 1.1 cm/J in the crystal doped with Mg of 5 mol.%. It is also found that gratings on the deep centers and the shallow centers were out of phase in Mg- or Zn-doped lithium niobate, while those in In-doped lithium niobate were in phase. We considered that different defects induced by different dopants

must be responsible for the observed results.

我们研究了热处理对近化学计量比铌酸锂晶体在中心波长为 365-nm 的非相干紫外光敏化下的双色全息存储性能的影响，发现还原处理有利于晶体双色全息存储性能的提高，而氧化处理则会降低晶体双色全息存储性能。当非相干紫外敏化光强度为 0.2 W/cm^2，半导体 780-nm 记录光强度为 0.25 W/cm^2 时，经还原处理后的 2.2-mm 厚的近化学计量比铌酸锂晶体中双色全息记录灵敏度 S 和动态范围 M/#分别可达 4×10^{-3} cm/J 和 0.12。我们认为这主要是由于热还原处理之后晶体中小极化子寿命变长，同时晶体在敏化光波段的吸收增强所致。

Nonvolatile two-color holographic recording gated by incoherent ultraviolet lights centered at 365 nm was investigated in near-stoichiometric lithium niobate crystals under different thermal treatment. The results show that thermal reduction tends to improve the two-color recording performance, whereas thermal oxidation degrades the two-color recording. With an incoherent ultraviolet gating light of 0.2 W/cm^2 and a semiconductor recording laser at 780 nm of 0.25 W/cm^2, a two-color recording sensitivity of 4×10^{-3} cm/J and a recording dynamic range characterized by M/# of 0.12 were achieved in a 2.2-mm thermally reduced near-stoichiometric lithium niobate crystal. We attribute the improvement to the prolonged lifetime of small polarons and the increased absorption at the gating wavelength due to thermal reduction.

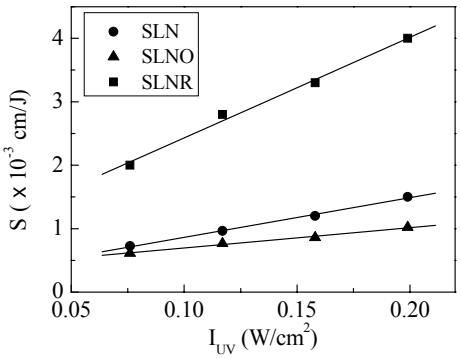

图 2 生长态（SLN）、氧化处理（SLNO）还原处理（SLNR）近化学比铌酸锂晶体的双色全息记录灵敏度 S 随非相干敏化紫外光的变化。其中光栅间距Λ和记录光强 I_r 分别为 1.4 μm 和 0.25 W/cm^2。

Fig. 2 Dependences of the sensitivity S on the gating intensity for SLN (solid circles), SLNO (solid triangles) and SLNR (solid squares). The experimental parameters for Λ and I_r were 1.4 μm and 0.25 W/cm^2, respectively.

通过建立非传统偏置光折变效应的理论模型,我们在理论上系统地研究了均匀和周期介质中光的非线性传播过程。发现在非传统偏置光折变晶体中根据光场方向的不同可以表现出自聚焦和自散焦非线性效应。基于该新型非线性系统，可以在不改变外电场的情况下实现亮、暗孤子，以及离散和带隙孤子间的光学转换（Opt. Lett. 33, 878 (2008)）(Fig. 3)；不仅如此，非传统偏置所引起的各项异性的增强使得控制孤子光斑形变的能力大大加强。比如我们在实验上仅通过变化外电场方向和大小就可以实现椭圆离散孤子的椭圆度和长短轴方向可控性调制（Opt. Express 16, 3865 (2008)）(Fig. 4)。

With an anisotropic photorefractive model, we have theoretically investigated nonlinear

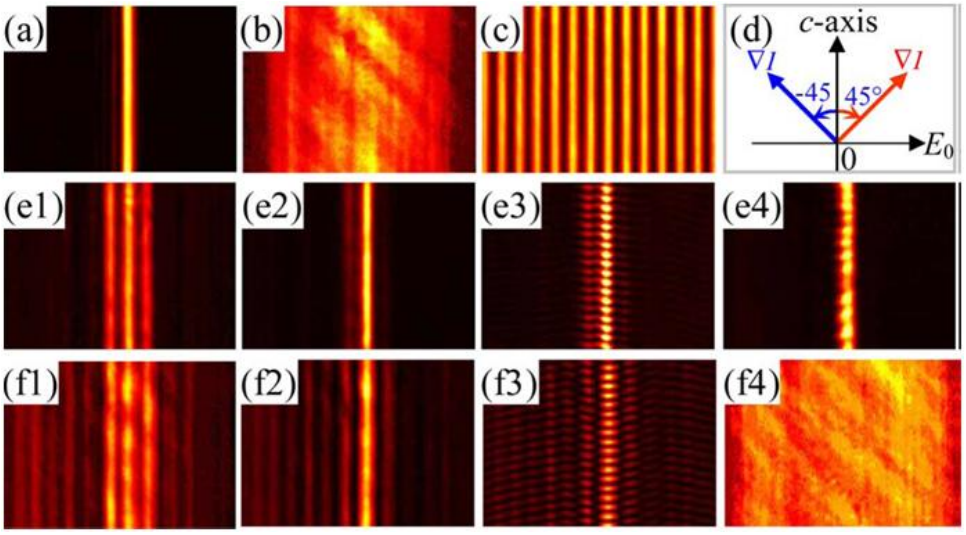

Fig. 3. (Color online) Experimental results. (a) and (b) Input and linear output probe beam pattern without lattice; (c) lattice beam pattern; (d) geometry of beam orientation; (e)–(f) probe-beam output pattern for (1) discrete diffraction, (2) self-trapping, (3) interference of soliton output, and (4) nonlinear output without lattice for (e) I=45° and (f) −45° at E0c, respectively.

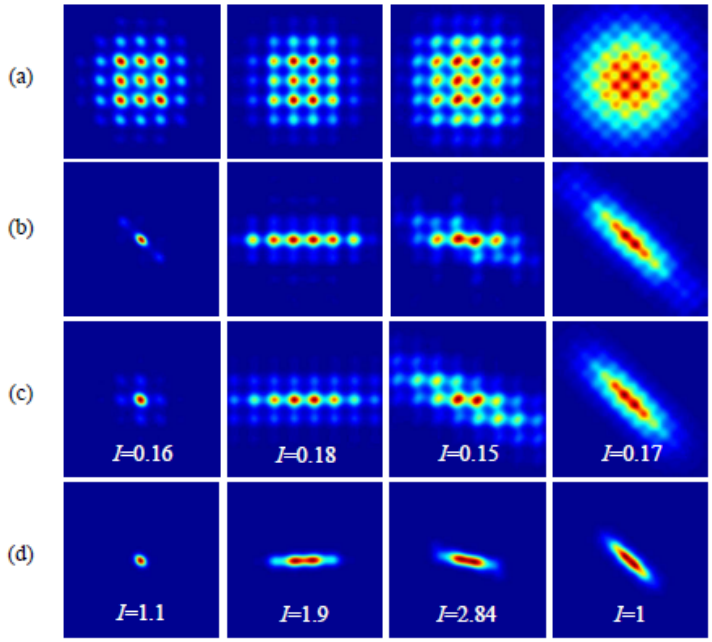

Fig. 4. Numerical results for discrete diffraction and self-trapped states. (a)-(b) are the output patterns of the probe beam under linear (a) and nonlinear (b) propagation obtained by beam propagation method. Animations show the corresponding evolution dynamics. (c)-(d) show soliton solutions at different peak intensities obtained with iteration method.

beam propagation in both homogeneous and periodic media under the NCB condition. We found that a self-focusing and -defocusing nonlinearity can exist simultaneously in the same material depending solely on the orientation of the probe beam, remarkably different from the conventional bias condition. This “hybrid nonlinearity” enables a transition between discrete and gap solitons without the need of bias reversal, as observed in our experiment. In addition, under the NCB

condition, the enhanced anisotropy and nonlocality lead to unusual index structures for reshaping soliton beams. For example, an elliptical discrete soliton can be created experimentally with its ellipticity and orientation controlled by reconfiguring the lattice structures without changing the soliton beam itself.

基于新型混合非线性系统，首次提出了离子型光子晶格的概念，并建立了适用于描述离子型光学周期结构布拉格反射的几何结构因子。利用光诱导的离子型晶格成功地实现了对光子带隙、光波传输以及布里渊区谱的操控。包括带隙截至、布拉格反射抑制、不同带隙孤子转变、正常和反常衍射、折射控制等。（OPN December 2008 | 25）(这一工作被美国光学学会评为 2008 年年度新闻 Optics in 2008)

Recently, we have shown that a new type of photonic lattices, such as an egg-crate structure not so amenable to fabrication, can be established in nonconventionally biased (NCB) photorefractive crystals. This new setting enables the reconfiguration of desired photonic structures and Brillouin Zones (BZs) for band-gap engineering and light manipulation. Some typical examples include Band-gap closure and Bragg reflection suppression, soliton transition between different band-gaps, and interplay between normal and anomalous diffraction/refraction under identical excitation condition.

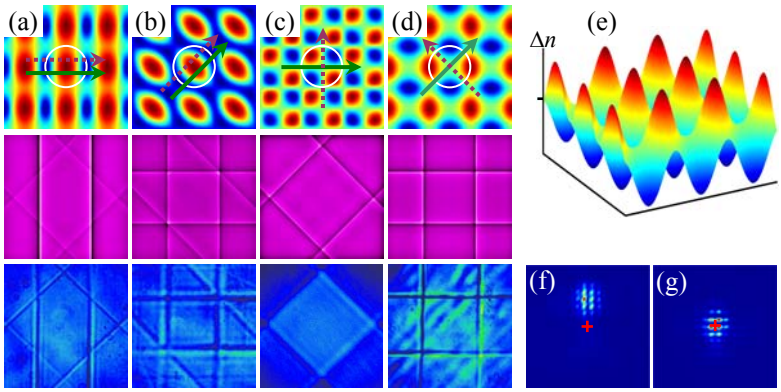

Fig.5 (a-d): Calculated refractive index profiles (1st row) and corresponding BZ spectra from simulation (2nd row) and experiment (3rd row) for lattice structures optically induced by an identical beam under different bias conditions, where the center of the white circle indicates one of the intensity maxima of the optical beam and the dashed and solid arrows show the directions of the *c*-axis and bias field, respectively. (e): 3D display of index pattern of (d) showing a typical egg-crate lattice structure. (f, g): Observed output patterns of a tilted probe beam with its excitation location in *k*-space marked by a white dot in (a, d), respectively, showing tunneling (f) and Bragg-reflection (g) in lattices. The red cross in (f, g) indicates the input position of the probe beam

利用混合非线性，可以实现依赖于空间转动的带系孤子间和带内孤子间的转换。仅仅改变入射探测光的方向，我们在二维离子型光子学晶格中证实了对应不同带边和次带边 Bloch 模式的孤子串的选择激发，由此观察到了孤子串在带系之间和带内之间的转换。我们得到的实验结果 (Fig. 7) 和理论预测(Fig. 6)符合得相当好.(submitted to OL)

Supported by hybrid nonlinearity, we can realize orientation-dependent transitions of in-gap and in-band soliton trains. we have demonstrated selective excitation of soliton trains associated

with Bloch modes from different band-edges as well as from sub-band-edges of the first Bloch band in a 2D ionic-type photonic lattice solely by changing the orientation of an input probe beam. Using a unique excitation scheme, we observed gap-to-gap and band-to-band transitions of the soliton trains supported by the hybrid self-focusing and –defocusing nonlinearity under the NCB condition. Our experimental observations (Fig. 7) of in-gap and in-band soliton trains agree well with our theoretical predictions (Fig. 6).

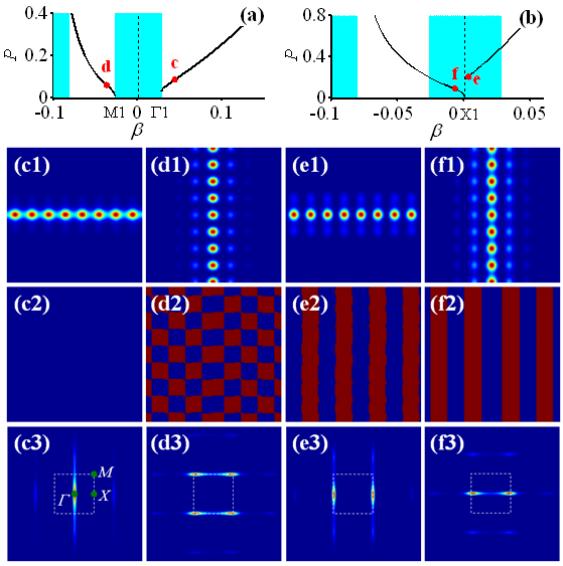

Fig. 6. Existence curves for soliton trains bifurcated from band-edges (a) and sub-band-edge (b) of the first Bloch band, where the Bloch bands are shaded; (c)-(f) Soliton solutions at the marked points in (a) and (b), where (1)-(3) are corresponding to intensity pattern, phase structure, and spectrum, respectively. The squares shown in (c3)-(f3) depict the boundary of the 1st Brillouin zone.

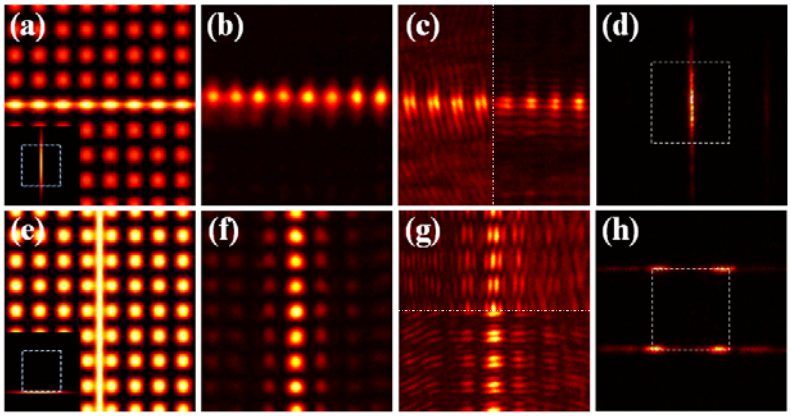

Fig. 7. Experimental demonstration of optically induced transition between discrete and gap soliton trains. (a)-(d) are for soliton trains bifurcated from Γ1 point; (e)-(h) are for that from M1 point. Left to right is corresponding to excitation condition, intensity pattern, interferogram, and spectrum of the soliton trains, respectively, where the dashed square depicts the boundary of the 1st Brillouin zone.

在二维自散焦骨架型光子晶格中我们首次在实验上实现以正入射激发拓扑数为一的稳态涡旋带隙孤子(Fig. 8 顶行)。当拓扑数改为二时，涡旋光在这种非线性光子中不再稳定，

将演化为准稳涡旋或是四极子(Fig. 8 底行)。通过对空间频谱、干涉图样和理论模拟分析进一步证实我们的结果。（OPTICS EXPRESS Vol. 16, 10110(2008)）

We report the first experimental demonstration of 2D gap vortex solitons by on-axis excitation of a single vortex beam in a self-defocusing “backbone” photonic lattice. We show that a singly-charged vortex can evolve into a gap vortex soliton, but a doubly-charged vortex tends to turn into quasi-vortex or quadrupole-like structure. The k-space spectra and interferograms (with a plane wave) of the self-trapped vortices from both experiments and numerical simulations are presented, and their stability is also studied. Our theoretical analysis finds good agreement with experimental observations.

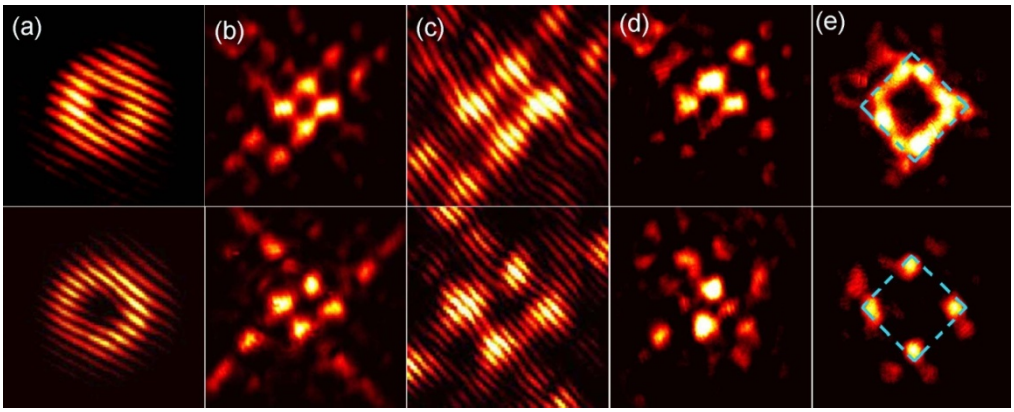

Fig.8: Experimental results of self-trapping of single-charged (top) and double-charged (bottom) vortices in a defocusing photonic lattice. (a) Interferograms showing the phase of the input vortex beams（zoomed), (b) intensity patterns of self-trapped vortex beams at lattice output, (c, d) interferograms between (b) and a tilted plane wave（zoomed) (c) and an on-axis Gaussian beam (d), respectively, and (e) the k-space spectra of (b) where the dash squares mark the first Brillouin-zone of the square lattice.

系统地研究了磁场对掺铁铌酸锂晶体弱光非线性效应的影响：在前面的研究中我们已经研究了磁场对光折变二波耦合的影响，发现通过外加磁场能够有效地改变掺铁铌酸锂中写入光栅的衍射效率。在此基础上，我们研究了磁场对光折变光栅擦除过程的影响。通过对四种不同配置的研究发现磁场对掺铁铌酸锂晶体的擦除过程影响很大，能够对擦除时间进行有效的调控。提供了一种有效调控光折变介质暗电导，从而有效调控光全息存储寿命及擦除时间的方法；另外还发现了磁场对扇形光散射的延迟作用。相关结果发表在 Journal of Applied Physics 和物理学报上，并在第十四届全国凝聚态光学性质学术研讨会（OPCM’ 2008）青岛做口头报告。

Systematic study of the influence of magnetic field on non-linear low-light effects of the iron-doped lithium niobate crystal: in front of the study, we have studied the influence of the magnetic field on the photorefractive two-wave coupling, and found that through the magnetic field can effectively changes the diffraction efficiency of the grating written in iron-doped lithium niobate. On this basis, we study the influence of magnetic field on the erasure process of the photorefractive grating. Through four different configurations of the study, we found that the influence of magnetic field on the erasing process is great, with this we can regulate and control the erasing time of the photorefractive grating effectively. This provides an effective method to

control the dark conductivity of the photorefractive medium and thus effectively control optical holographic storage life and erase time. We also found that the applying of a magnetic field can delay the fanning light-scattering effect effectively. Results published in the Journal of Applied Physics and Physics, and in the 14th session of the National Symposium on optical properties of condensed matter (OPCM '2008) Qingdao to do an oral report.

表面等离子基元的制作和研究：研究了磁场对表面等离子激元激发的影响。另外，在不同材料上，如磁性材料、光折变材料和超导材料等介质上镀金属膜激发表面等离子激元，并研究等离子激元的激发特性以及与材料本身非线性性质的相互作用。相关结果在第十四届全国凝聚态光学性质学术研讨会（OPCM’ 2008）青岛做口头报告。

The production and research of the SPP: Study the influence of magnetic field on the excitation of the SPP. In addition, plate metal-film on different materials, such as magnetic materials, photorefractive materials and superconducting materials, then excite the SPP and study the interaction of SPP and non-linear properties of the materials. Results are report in the 14th session of the National Symposium on optical properties of condensed matter (OPCM '2008) Qingdao.

制作微纳尺度的光纤并对其性质进行研究以及纳米尺度波导、定向耦合器光耦合的计算：已经制作出微纳尺度的硅光纤和微米尺度的 PMMA 光纤。对光在微纳尺度光纤中的传播特性进行了研究，并且若干利用微纳尺度光纤制作激光器、传感器以及探测器的研究正在进行中。另外，我们还研究了纳米波导阵列和亚波长布拉格光栅的光传播特性。相关结果发表在南开大学学报，在第十四届全国凝聚态光学性质学术研讨会（OPCM’ 2008）青岛 做口头报告。

Production and study of micro-nano fiber, as well as the calculation of nano-scale waveguide, optical directional coupler: We have produced silicon micro-nano scale fiber and micron-scale PMMA optical fiber. The light transmission properties of micro-nano scale fibers have been studied, and a number of methods to use the micro-nano fiber, such as make lasers and sensor detectors are developed in progress. In addition, we also studied optical transmission properties of the nano-arrays of the sub-wavelength waveguide and sub-wavelength scale Bragg grating. Results published in Nankai Journal, in the 14th session of the National Symposium on optical properties of condensed matter (OPCM '2008) Qingdao to do an oral report.

对光镊对不同种类的球形粒子的光俘获作用的研究：强吸收球形粒子、线性吸收球形粒子、有吸收双层球形粒子在高斯光束及环形光束中的光俘获的理论模拟研究。相关结果发表在 J. Opt. A 、物理学报以及南开大学学报上。

Research on the capture characteristic of optical tweezers for different types of spherical particles: The capture characteristic of strong absorbing spherical particles, the linear absorbing spherical particles and spherical particles are captured in the double-Gaussian beam and ring beam are simulated theoretically. Results published in J. Opt. A, NanKai Journal and Acta Physica Sinica.

光外差干涉测量技术的研究：对基于马赫-曾德尔外差干涉仪的光偏振态测量技术进行了详细的研究。相关结果发表在激光技术上。

Study on optical heterodyne interferometry technology: a heterodyne interferometer based on Mach - Zehnder interferometer used for optical polarization measurement technology was studied in detail. Results published in Laser Technology.

光谱表征及传感技术/Spectral Charaterization and Sensing Techniques

负责人：臧维平

本方向涉及激光器，上转换发光材料，光纤器件，稀土掺杂发光材料，应用光谱学和光谱仪器等方面。本年度发表论文 16 篇；申请发明专利 2 项，申请实用新型专利 1 项；在研课题经费 172 万元；结题项目 2 项。取得的代表性成果如下：

In this field, we mainly focused on the laser ,up conversion luminescent material ,fiber optic, rare earth dope glass , applied spectroscopy and spectral instrument . 16 papers were published in international academic journals, and three patents applicanted. This year, we obtained some important results, they are mainly shown as following:

1.新型超短长度高增益光纤器件的研究

取得的成果主要有：

(1) 对 Er/Yb 共掺玻璃材料的发光及激光特性进行了较为深入的系统研究。 建立起对 Er 离子上能级荧光寿命进行精确测量的实验装置，该装置立足于本实验室已有条件，结构简单成本较低，测量精度高。

(2) 利用有限差分光束传播法模拟了泵浦光和信号光在超短长度 Er/Yb 共掺磷酸盐玻璃高增益光纤中的传输状况，分析了 Er^{3+}浓度、Yb^{3+}浓度、光纤长度、泵浦光功率、信号光功率对放大器增益的影响，并与单掺 Er^{3+}的光纤做了比较，证实了 Yb^{3+}的掺入能在很大程度上提高泵浦光的吸收效率。

(3) 设计并制作了自动光纤拉制设备。利用单片机及步进电机，实现了拉丝过程的计算机调速控制，用衍射法在拉丝过程中对光纤直径进行动态测量，计算机自动调整电机转速，达到实时控制拉丝速度从而自动控制光纤直径。现已拉出直径在 100—130μm 的普通光纤，并利用光纤专用紫外固化涂料及高压汞灯紫外光源，在拉丝过程中给光纤加涂敷保护。

(4) 国内首次利用长度为 12cm 的高增益 Er/Yb 共掺磷酸盐玻璃光纤实现了功率达 170mW 的激光连续运转。中心波长为 1534.2nm，光谱半宽度为 0.053nm。

(5) 首次观测了长度为 10.4cm 的高增益 Er/Yb 共掺磷酸盐玻璃光纤在 976nm 半导体激光器抽运下的超荧光发光现象。

1. The novel ultra-short high gain fiber devices

(1) The spectrum and laser emission characteristics of the Er^{3+}-Yb^{3+} co-doped glass materials has been studied systematically and deeply. The experimental instruments have been set for the accurate measurement of fluorescence lifetime of Er^{3+}. This device is set based on our laboratory original conditions, with simple structure, lower cost, and high measurement accuracy.

(2) The finite difference beam propagation method (FD-BPM) has been used to simulate the propagation properties of pump and signal light in the ultra-short Er^{3+}-Yb^{3+} co-doped phosphate glass high gain fiber. We analyzed the influence of Er3 + concentration, Yb3 + concentration, fiber length, pump power, the signal optical power on the amplifier gain.

Through the comparison with the Er-doped glass fiber; we confirmed that the Yb3+ can improve the absorption efficiency of the pump light effectively.

(3) Designed and fabricated an automatic optical fiber pulling machine. The fiber diameter can be measured on line and the speed of the fiber pulling can be controlled real-time. Ordinary optical fiber of 100-130μm in diameter,can be drawn and the UV curing coatings and high-pressure mercury lamp UV light source in the drawing process were used to coat the optical fiber for protection.

(4) The continuous operation of a length of 12cm high-gain Er / Yb co-doped phosphate glass fiber with 170mW laser power was demonstrated. The center wavelength was 1534.2nm, spectral half width 0.053nm.

(5) For the first time, the superfluorescence has been demonstrated from a 10.4 cm high gain Er / Yb co-doped phosphate glass fiber with 10.4 cm in length. under the 976nm semiconductor diode-pumped laser.

2.玻璃陶瓷的研究

Er/Yb 磷酸盐玻璃具有储能大、能量传递效率高等突出优点，在上转换发光方面，1.54um 激光方面具有重要应用。但是其具有玻璃本身的一些弱点，比如热导率不够高、机械强度稍差等，使得应用受到限制。玻璃陶瓷则可以将玻璃与晶体的优点结合起来。目前已经制备出了掺 Er 氟化物玻璃陶瓷，但是磷酸盐玻璃陶瓷由于属于立方晶系，难以制备出透明玻璃陶瓷，所以掺 Er 磷酸盐玻璃陶瓷几乎未见报道。我们尝试了很多种配比和各种公益方法，终于制备出了透明的掺铒玻璃陶瓷，取得的具体成果有：

2. Glass Ceramics

Er / Yb phosphate glass has advantages of large energy storage and high energy transfer efficiency, which has important applications in the upconversion and 1.54um laser. However, the glass itself has some weaknesses, such as the low thermal conductivity ,weak mechanical strength, which make the applications of the materials limited. Glass-ceramic combines the advantages of glass and ceramic. Now Er-doped fluoride glass-ceramic can be prepared already, but the phosphate glass-ceramic as that belonging to cubic crystal system, is difficult to prepare to be transparent glass-ceramic, so there has been almost no Er-doped phosphate glass-ceramic research so far. We tried a variety of methods of proportion and a variety of techniques, and finally prepared erbium-doped transparent glass ceramics. Detailed achieves are:

(1) 通过多种原料配比，进行热处理析晶，成功制备出了透明的掺铒玻璃陶瓷，下图为配比（30-x）Li_2O- 10CaF_2-60 P_2O_5- xTiO_2（x=0，0.2，0.4，0.6，0.8）的 XRD 图。可见，微晶颗粒未 $LiPO_4$.

Through a variety of raw material ratio, heat treatment crystallization successfully prepared transparent erbium-doped glass-ceramic, the next picture shows the ratio of （30-x）Li_2O- 10CaF_2-60 P_2O_5- xTiO_2（x=0，0.2，0.4，0.6，0.8） the XRD diagram, from which the microcrystalline particles of $LiPO_4$ can be found.

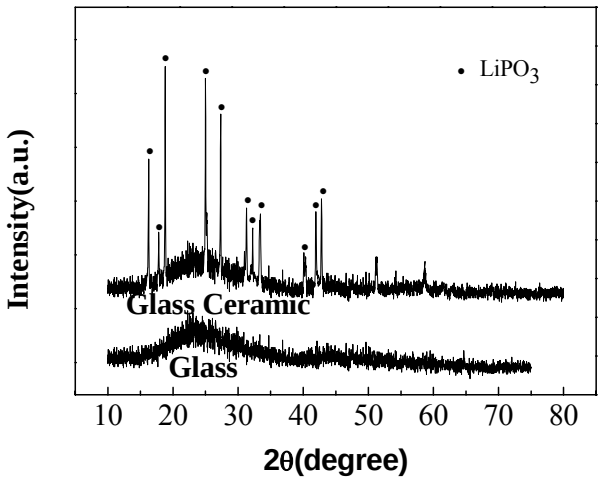

图 1 玻璃和玻璃陶瓷的 XRD 图。

Fig.1 The XRD of glass and glass ceramic.

(2) 测量了玻璃陶瓷的发光光谱。图 2 是玻璃与玻璃陶瓷的吸收谱对比。说明 Er^{3+}周围的晶体场环境已经发生了变化。

Measurement of the luminescence spectra of glass-ceramic. Figure 2 is the comparison of absorption spectrum of glass and glass-ceramic. This shows that the crystal-field environment around Er^{3+} has been changed.

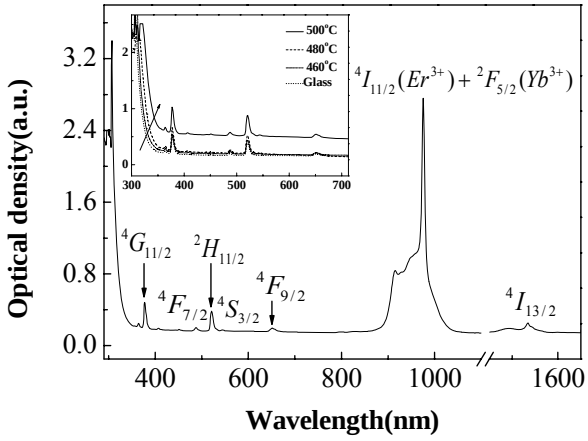

图 2 不同温度处理下的玻璃陶瓷与玻璃样品的吸收谱对比。

Fig.2 The comparison of absorption spectrum of glass and glass-ceramic.

(3) 图 3 是玻璃和微晶玻璃在 975nmLD 光源激发下的上转换发光谱。微晶玻璃中的上转换发光有了很大程度的提高，其中以绿光的发射最强。而且随着热处理温度的增加，上转换绿光发射强度有了明显的增加（图 5）。

Figure 3 is the up-conversion excitation spectra of glass and glass-ceramic under 975nm LD excitation. The upconversion luminescence of glass ceramics has been greatly

increased, with the strongest green light. Moreover, with the heat treatment temperature increases, up-conversion green emission intensity increased significantly (Figure 5).

(4) 图 4 是 975nmLD 激发下玻璃与不同热处理条件下得到的玻璃陶瓷的近红外荧光光谱。可以看出，热处理后的玻璃陶瓷的发光强度有了一定程度的增强，且出现了一定的劈裂。

Figure 4 is the near-infrared fluorescence spectroscopy of glass-ceramics excited by 975nm LD with different heat treatment conditions. We can see that the heat-treated glass ceramic luminous intensity has been enhanced to some extent, and also we can notice the emergence of a certain amount of splitting.

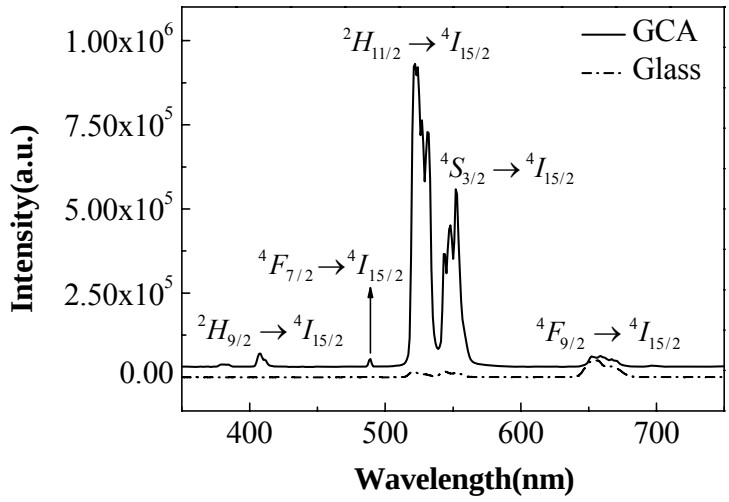

图 3　975nmLD 泵浦下的 Er/Yb 双掺玻璃和玻璃陶瓷上转换发射光谱。

Fig.3 The up-conversion excitation spectra of glass and glass-ceramic under 975nm LD excitation.

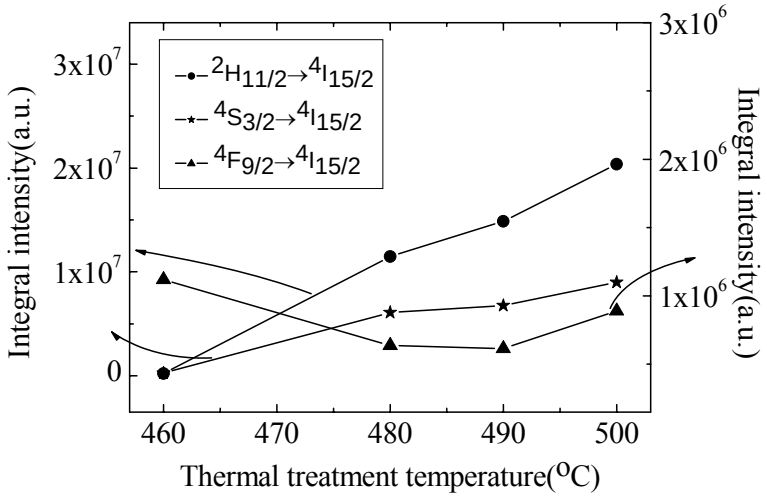

图 4 上转换绿光和红光的发射强度随热处理温度的变化关系。

Fig.4 The near-infrared fluorescence spectroscopy of glass-ceramics excited by 975nm LD with different heat treatment conditions.

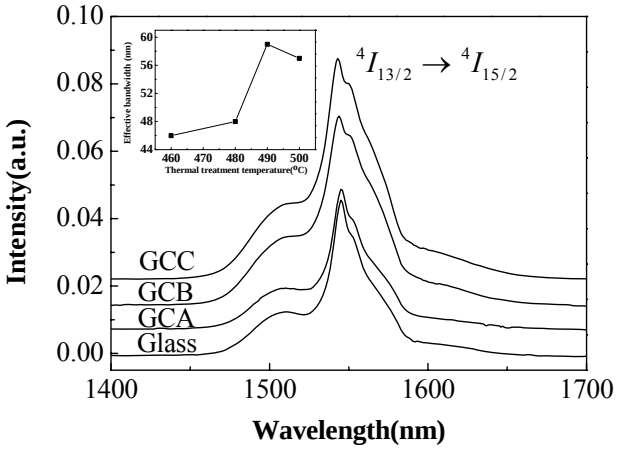

图 5　975nmLD 泵浦下的 Er/Yb 双掺玻璃和玻璃陶瓷近红外发射光谱。

Fig.5 The near-infrared fluorescence spectroscopy of Er / Yb phosphate glass and glass-ceramics excited by 975nm LD

3. 氟氧化物玻璃陶瓷的相关研究

在传统氟氧化物玻璃陶瓷研究的基础上，采用“热诱导-腐蚀”法获得玻璃网状结构中热诱导产生的纳米颗粒。水相纳米颗粒保持了在玻璃中的发光和结构特性，这为纳米颗粒的制备开辟了新的途径。

在工艺上研究了玻璃陶瓷中微晶产生过程与工艺参数之间的依赖关系。研究结果显示：热处理温度影响微晶的生长尺寸，而热处理时间则会对微晶的数目产生较大的影响。

在 Tm/Yb 共掺的玻璃陶瓷中获得明亮的蓝光。在蓝光上转换过程分析中发现 Tm/Yb 之间存在着反向能量传输通道，该反向能量传输通道与基质声子能量有着密切的联系。在玻璃中较容易发生，而在微晶中很难起到实质性的作用。

3. The oxyfluoride glass ceramics

An innovative route is reported to fabricate nano-particles in aqueous solution from oxyfluoride glass by the thermal induction and corrosion treatment. β-(Pb,Cd)F_2:Er^{3+},Yb^{3+} nano-particles in aqueous solution were prepared by means of thermal induction to produce nano-particles in glass matrix and corroding the glass host by hydrofluoric acid. The nano-particles in aqueous solution have the same structure and luminescent properties as nano-particles existing in glass matrix. Although thermal induction and corrosion treatment were used to prepare β-(Pb,Cd)F_2:Er^{3+},Yb^{3+} nano-particles in aqueous solution, it may directly apply to any other silicate glass ceramics doped with other RE ions and embedded various composition of nano-particles, since the preparation method is based on a fundamental consideration.

The oxyfluoride glass ceramics are an important up conversion luminescent materials. Er^{3+}/Yb^{3+}-codoped transparent oxyfluoride glasses were prepared by melt-quenching and subsequently heat-treated with different time and temperature, and the crystallization process of fluoride nanocrystals from the glass was investigated for the first time. X-ray diffraction (XRD) and fluorescence spectra investigation reveal that fluoride nanocrystals are distributed

homogeneously among the glassy matrix for the sample doped with Er^{3+}/Yb^{3+}. The crystallization process indicates that heat-treated temperature influences the size of fluoride nanocrystals, while heat-treated time influences the quantity of them. Moreover, the red emission intensities increase due to the incorporation of Er^{3+}/Yb^{3+} into the fluoride nanocrystals under different heat-treated methods, which are researched by fluorescence spectra.

Two series of $Tm^{3+}$and Yb^{3+}codoped oxy-fluorosilicate glass ceramics which components are $30SiO_2$-(20-x-y)Al_2O_3-$40PbF_2$-$10CdF_2$ –xTm_2O_3-yYb_2O_3 were prepared and characterized. The up-conversion spectra of these samples were investigated and the up-conversion luminescence mechanisms of Tm^{3+}/Yb^{3+} system were analyzed. The effects of Tm^{3+} and Yb^{3+} concentration on up-conversion luminescence spectra were systematically studied. The results suggest that blue up-conversion emission intensities decrease when Tm^{3+} concentration increases due to the cross relaxation interaction between Tm^{3+} ions. The optimum Tm^{3+} concentration is 0.025mol%; Three photons process and Yb^{3+} ions cooperative up-conversion energy transfer process co-exist in the Tm^{3+}/Yb^{3+} up-conversion luminescence system. When Yb^{3+} concentration increases, due to the energy back transfer process of $^3H_4(Tm^{3+})\rightarrow{}^2F_{5/2}(Yb^{3+})$, the blue up-conversion emission intensities would decrease. With the help of Yb^{3+} ions cooperative up-conversion energy transfer, in fact, the blue up-conversion emission intensities increase, which are in accord with the experimental results.

4.光谱表征领域和仪器领域

光谱学仪器方面，利用体光栅外腔调制，成功将半导体激光器输出带宽压缩到0.1个nm，这种方法结构可靠，价格低廉，可以用于拉曼光谱仪器中，尤其是近红外波段785nm或808nm激光器，具有广泛应用前景。

光谱表征领域，研究了InGaAs/GaAs单量子阱PL谱的温度变化特性，指出了其低温状态下的发光主要来源于激子发光的特性，另外还对金属-砷化镓界面进行了调制光谱研究和拉曼光谱研究。

4. Spectral characterization and spectral instrument

In the spectral instrument field , we compress the laser line width of semiconductor laser diode to 0.1nm using the volume grating and external cavity modulation. This kind laser could using in the Raman spectrometer , specially in the NIR band , example of 785nm or 808nm laser .

In the spectral characterization field , we research the temperature dependence of PL spectrum in researching InGaAs/GaAs single quantum well, and point out the lighting on the low temperature are mostly from the excition. Otherwise , we research the modulation spectral and Raman in the interface of GaAs and metal.

半导体生长技术和半导体器件/ Semiconductor Growth and Devices

负责人：舒永春

2008 年度本方向主要在以下方面取得了进展:

This year, we obtained some important results, they are mainly shown as following:

（1）成功地将反射 Z 扫描技术应用到 $GaAs/Al_xGa_{1-x}As$ 多周期结构的非线性吸收研究中，并提出一个可以半定量计算非线性吸收系数的模型。实验和理论结果表明，在一定范围内，z=0 时的入射光强是决定非线性吸收系数大小的主要因素。此外，该模型也展示了不同 Al 组分 x 对此多周期结构非线性吸收系数的影响，这在之前的研究中还未见报道过。

（2）利用拉曼光谱研究了 InGaAs/InP、InGaP/GaAs 材料的穿透深度、内应力和有序度。得出拉曼穿透深度与 In 组分 x 基本满足线性关系，$In_xGa_{1-x}As$ 的拉曼信息仅来源于外延层，对于 $In_xGa_{1-x}P$，穿透深度要远大于 100nm 厚的外延层。根据内应力分析，对于基本匹配（$x=0.485$）的 InGaP/GaAs，拉曼光谱类 GaP LO 模的峰位基本是一个常数，当 In 的组分 x<0.485 时，拉曼光谱峰位频移量 $\Delta\omega$<0，外延层受张应力并随 In 组分的减小而增大；当 x>0.485 时，$\Delta\omega$>0 外延层受压应力并随 In 组分的增大而增大。对于 InGaAs/InP 材料体系，从拉曼光谱峰位频移可以得出同样的内应力分布规律。对于有序度研究，实验结果表明有序度的增加具体主要表现在两个方面：LO_2 模的峰位发生蓝移以及 b/a 值的减小。并得出随着Ⅴ/Ⅲ束流比的增加，其有序度先增大后减小。

（3）利用传输矩阵方程求解并分析了垒在阱中和阱在阱中的载流子隧穿特性。指出阱在阱中的结构比垒在阱中、单阱、单垒都好的隧穿特性。改变中间量子阱的宽度的透射特性模拟结果中发现，其中的一个透射峰基本不发生变化。另外的两个能级，一个随着阱宽的增加逐渐增加，一个逐渐减小。在对内阱非对称性的模拟结构中发现，较宽的小阱，能级变化幅度比较大，由于限制的减弱，能级向低能方向偏移。第一激发态的能级也轻微的向低能方向偏移，移动的幅度小，第二激发态与第一激发态之间的耦合对能级的漂移也起着重要作用。

（1）The room-temperature third order nonlinearities in GaAs/AlGaAs multiple quantum wells have been studied using reflection Z-scan technique. A model to calculate the absorption coefficient of quantum wells in the nonlinear regime is presented. The nonlinear absorption intensity dependence was presented both theoretically and experimentally: the weaker the input optical intensity at z=0, the bigger the nonlinear absorption coefficient. Besides, the model presented the effect of Al content on the nonlinear absorption coefficient, which hasn't been reported.

（2）The penetration depth, internal stress and the degree of InGaAs/InP, InGaP/GaAs semiconductor material system were researched by Raman spectroscopy. The values of Raman penetration depth and In composition x are basically satisfied with a linear relationship. The excitation light can't penetrate through the epitaxial layers of InGaAs/InP. However the penetration depth of InGaP/GaAs is far greater than the thickness of epitaxial layer, which is in the thickness of 100nm. For the internal stress of InGaP/GaAs, when In component <0.485, the shift of peak location of TO mode in Raman spectroscopy $\Delta\omega$ >0, the epitaxial layer is subjected to pressure stress and the larger with In component decreasing; And when In component >0.485, $\Delta\omega$ <0, the epitaxial layer is subjected to tensile stress and the larger as In component increasing; And for InGaAs/InP is almost same in internal stress.For the ordering of InGaP/GaAs, with the increasing of Ⅴ/Ⅲ beam ratio, the ordering degree first increases and then

degreases, and the quality of materials is better when Ⅴ/Ⅲ beam ratio is near 8~9.

（3）A Schrodinger equation is solved numerically for a barrier in a quantum well and a quantum well in another well structure by the transfer matrix technique. Effect of structure parameters on the transmission probabilities is investigated in detail. The results suggest that symmetry plays an important role in the coupling effect between the quantum wells. The relationship between the width of the inner well and the resonant energy levels in well-inwell structures is also studied. It is found that the ground state energy and the second resonant energy decrease with increasing width of the inner well, while the first resonant energy remains constant.

（4）建立起了光致发光和电致发光的综合测试系统，在现有的光谱测量基础上，利用项目的设备经费进口了一台 Keithley2410 高精度电流源表，购买了高灵敏度红外探测器。自己动手组装了微型电致发光器件显微光纤探测终端，为器件的光电特性的分析做好了准备。按计划完成了电致发光器件的标准 MOS 工艺流程和掩模版图设计和制版。利用 AutoCAD 和 L－ediit 软件根据标准的 MOS 加工工艺要求设计了一套硅 MOS 结构发光器件的光刻掩模版，其中含尺寸为 2 微米－3 毫米的器件阵列和各种形状。电致发光器件的标准 MOS 工艺流程，包含，硅片 SCA1－SCA2 清洗－H2O2+H2SO4 腐蚀－LOCOS 工艺－热氧化－Si 离子注入－高温退火形成纳米颗粒－Er 离子注入－退火－SiON 沉积－ITO 沉积等 20 余道工序。 其核心制备工艺如下：

（4）We have finished the preparation of several projects on silicon optoelectronics, including setting up the electrical and optical measurement system as in fig.1, device processing and mask design for the MOSLEDs as in fig.2. The first set of the EL devices were processed by the clean room facilities in Forschungszentrum Dresden Rossendorf in Gemany.

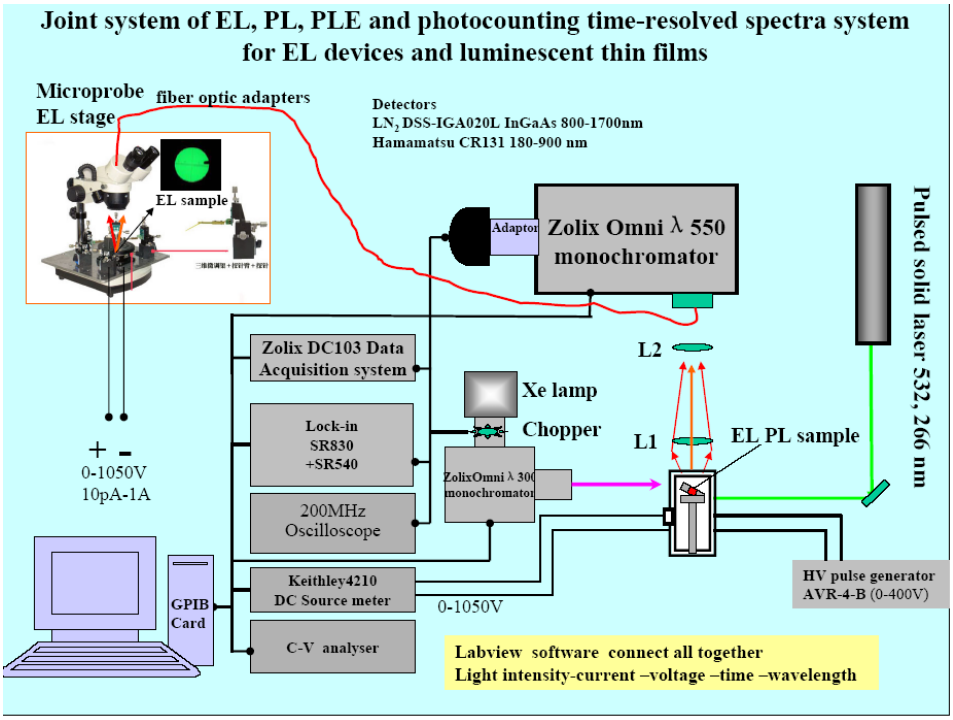

图 1. 项目组建的电致发光、光致发光、I-V/CV，L－I－V 综合测量系统方框图

Fig.1 Joint system of EL,PL,PLE and photocounting time-resolved spectra system for EL devices and luminescent thin films

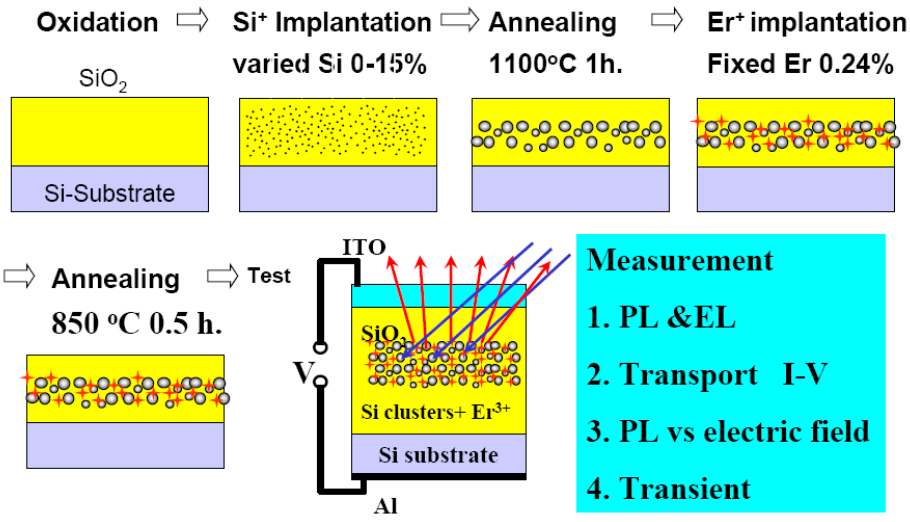

图 2 器件制备的核心工艺流程图

Fig.2 The processing of device preparation

（5）利用德国 Rossendorf 研究中心的工艺线进行了工艺验证，获得了首批 SiO_2：Er一纳米硅电致发光样品。器件的中硅和 Er 离子注入参数及其深度分布如图 3 所示，器件结构示意图和制备的 4-inch wafer 照片如图 4 所示。为了增加光耦合输出效率，表面电极采用 100nm 的透明 ITO 导电层。利用 Er 和硅离子共注入热氧化 SiO2 薄膜的方法制备出 Er 离子掺杂的含纳米硅微晶的 SiO2 发光薄膜，在此基础上制备出 ITO/SiON/Si-rich SiO2:Er/Si MOS 结构电致发光器件，分别获得了来自纳米硅和 Er 较强的光致发光， 在微弱电流下，观测到来自 Er 的红外电致发光。这一结果验证了前期工艺设计的可靠性。比较研究了硅微晶密度的变化对于 MOS 结构的电致发光和光致发光特性的影响。随着纳米硅微晶的增多，Er 离子在 1.54μm 处的红外光致发光显著增强，显示出纳米硅微晶对 Er 离子光致发光的敏化作用。相反，对于电致发光来说，增加纳米硅微晶数量的同时也增加了 SiO2 薄膜中的电子俘获陷阱，电子在纳米硅微晶之间的隧穿降低了过热电子的数量和平均能量，因而降低了碰撞激发 Er 离子产生的电致发光效率。

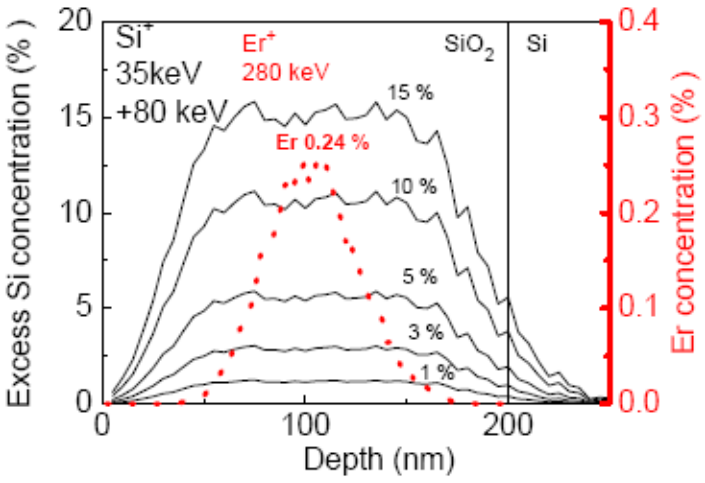

图 3 利用 Trim98 模拟的离子注入的首批 SiO2：Er一纳米硅电致发光样品中单质硅和 Er 的深度分布。

Fig.3 The depth distribution of silicon and Er in SiO2:Er samples.

（5）Er-doped SiO_2 films containing silicon nanocrystals were prepared by the Er and Si co-implantation into thermally oxidized SiO_2 films showed in fig.3 and in fig.4. Electroluminescence was studied with a metal-oxide-semiconductor structure of indium-tin-oxide/ SiON/Si-rich SiO_2 : Er/Si. The different effect of silicon nanocrystal concentration was studied on the mechanisms of electroluminescence and photoluminescence. The 1.54 μm PL peak of Er^{3+} in the infrared region dramatically increased with increasing the density of silicon nanocrystals under photoluminescence excitation, which indicated that silicon nanocrystals play an important role in the sensitization in the photoluminescence excitation. Contrary to PL, due to the electron tunneling between silicon nanocrystals and the electron trapping at the surface of silicon nanocrstals, the average energy and the population of hot electrons decreased in the electroluminescence excitation, thus the EL efficiency of Er^{3+} decreased dramatically with the increase of silicon nanocrystals.

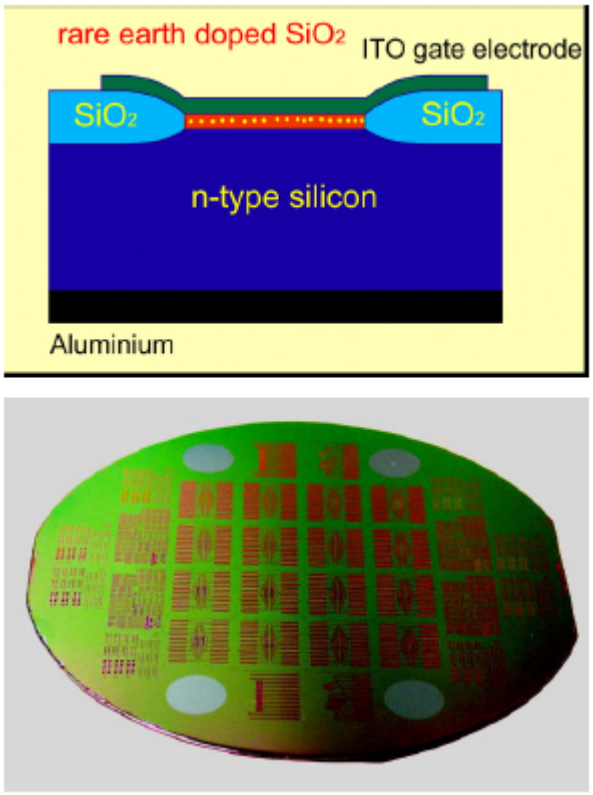

图 4　器件结构示意图和制备的 4-inch wafer 照片。

Fig.4 The schematic diagram of device and the picture of 4-inch wafer.

发表论文/Publications in Journal

1. Rong Dong, Christian E. Rüter, Detlef Kip, Ofer Manela, Mordechai Segev, Chengliang Yang, and Jingjun Xu, "Spatial Frequency Combs and Supercontinuum Generation in One-Dimensional Photonic Lattices", *Phys. Rev. Lett.* 101, 183903 (2008).*
2. Guoquan Zhang, Fang Bo, Feng Gao, Rong Dong, Yanfei Tu, and Jingjun Xu, "*Slow and fast lights with moving and stationary refractive index gratings in solids at room temperature*", *International Journal of Modern Physics* B 22(5), 447-468 (2008). (**invited review paper**) *
3. Zhi-Bo Liu, Jian-Guo Tian, Zhen Guo, Dong-Mei Ren, Feng Du, Jian-Yu Zheng, and Yong-Sheng Chen, Enhanced Optical Limiting Effects in Porphyrins Covalently Functionalized Single-Walled Carbon Nanotubes, *Adv. Mater.* 20(3), 511-515(2008).*
4. Leiting Pan, Xinzheng Zhang, Kun Song, Xian Wu, Jingjun Xu, "Exogenous nitric oxide-induced release of calcium from intracellular IP3 receptor-sensitive stores via S-nitrosylation in respiratory burst-dependent neutrophils", *Biochemical and Biophysical Research Communications* 377(4) 1320-1325 (2008).
5. Feng Gao, Jingjun Xu, Guoquan Zhang, Fang Bo, and Haixun Liu, "Paraxial energy transport of a focused Gaussian beam in ruby with nondegenerate two-wave coupling-like mechanism", *Appl. Phys. Lett.* 92, 021121 (2008).*
6. Shuanggen Zhang, Jianghong Yao, Qing Shi, Yange Liu, Weiwei Liu, Zhangchao Huang, Fuyun Lu, and Enbang Li, Fabrication and characterization of periodically poled lithium niobatewaveguide using femtosecond laser pulses, *App.Phys.Lett.*, 92(23):11061- 11063 (2008).
7. Yong-Fa Kong, Sheng-Qing Wu, Shi-Guo Liu, Shao-Lin Chen, and Jing-Jun Xu, "Fast photorefractive response and high sensitivity of Zr and Fe codoped $LiNbO_3$ crystals", *Appl. Phys. Lett.* 92, 251107 (2008).*
8. Zhang-Cheng Xu, Ya-Ting Zhang, and Jørn M. Hvam, "Long luminescence lifetime in self-assembled InGaAs/GaAs quantum dots at room temperature", *Appl. Phys. Lett.* 93, 183116 (2008). *
9. Ya-Ting Zhang, Zhang-Cheng Xu, "Direct observation of the size dependence of Dexter energy transfer from polymer to small PbS quantum dots", *Appl. Phys. Lett.* 93, 083106 (2008).
10. Zhang-Cheng Xu, Ya-Ting Zhang, Tackeuchi Atsuchi, Horikoshi Yoshiji and Jørn M. Hvam, "Short exciton radiative lifetime in sub-monolayer InGaAs/GaAs quantum dots", *Appl. Phys. Lett.* 92, 063103 (2008).
11. Feng Song, , Zhen-zhou Cheng, Chang-guang Zou, Lin Han, Xiao-chen Yu, Jia-xiang Zhang, Xue-ping Jiang , Pei-ze Han, and Jian-guo Tian , "Compact high power broadband Er^{3+}−Yb^{3+}- codoped super fluorescent fiber Source", *Appl. Phys. Lett.* 93, 091108 (2008).*
12. J.M.Sun, L.Rebohle, S.Prucnal, M.Helm, and W.Skorupa, "Giant stability enhancement of rare-earth implanted SiO_2 light emitting devices by an additional SiON protection layer", *Appl. Phys. Lett.* 92, 071103 (2008).

* 选录论文/Selected papers

13. Lin Han, Feng Song,_ Shu-Qi Chen, Chang-Guang Zou, Xiao-Chen Yu, Jian-Guo Tian, Jun Xu, Xiao-dong Xu, and Guang-jun Zhao , “Intense upconversion and infrared emissions in Er^{3+}–Yb^{3+} codoped Lu_2SiO_5 and $(Lu_{0.5}Gd_{0.5})_2SiO_5$ crystals”, *Appl. Phys. Lett.* 93, 011110 (2008).

14. Peng Zhang, Cibo Lou, Sheng Liu, Fajun Xiao, Jianlin Zhao, Jingjun Xu and Zhigang Chen. “Band-Gap Engineering and Light Manipulation with Egg-Crate Photonic Lattices”, *OPN* 25 December (2008). *
15. Rubin Liu,Yongchun Shu,Guanjie Zhang,Jiamin Sun,Xiaodong Xing,Biao Pi, Jianghong Yao,ZhanguoWang,,Jingjun Xu,"Study of nonlinear absorption in GaAs/AlGaAs multiple quantum wells using the reflection Z-scan",*Opt Quant Electron* 39:1207–1214(2008).
16. Shuqi Chen, Weiping Zang, Axel Schülzgen, Jinjie Liu, Lin Han, Yong Zeng, Jianguo Tian, Feng Song, Jerome V. Moloney, and Nasser Peyghambarian, "Implicit high-order unconditionally stable complex envelope algorithm for solving the time-dependent Maxwell’s equations", *Opt. Lett.* 33, 2755 (2008).
17. Detlef Kip, Christian E. Rüter, Rong Dong, Zhe Wang, and Jingjun Xu, “Higher-band gap soliton formation in defocusing photonic lattices”, *Opt. Lett.* 33(18), 2056-2058 (2008).
18. Peng Zhang, Sheng Liu, Jianlin Zhao, Cibo Lou, Jingjun Xu and Zhigang Chen,” Optically induced transition between discrete and gap solitons in a nonconventionally biased photorefractive crystal”, *Opt. Lett.* 33, 878(2008).
19. Kenji Hirano, Tomoe Fukamachi, Masami Yoshizawa, Riichirou Negishi, Keiichi Hirano, Zhang-Cheng Xu and Takaaki, Kawamura, “X-ray Interference Fringe of Bragg-(Bragg)m-Laue case”, *J. Phys. Soc. Jpn.* 77, 103707 (2008).
20. Wen-Bo Yan, Li-Hong Shi, Hong-Jian Chen, Yang-Xian Li and Yong-Fa Kong, “The UV-light-induced absorption in pure $LiNbO_3$ investigated by varying compositions”, *J. Phys. D-Appl. Phys.* 41(8), 085410 (2008).
21. Hua Yu, Nan Hu, Ya-Nan Wang, Zi-Lan Wang, Zong-Song Gan, and Li-Juan Zhao, “The fabrication of nano-particles in aqueous solution from oxyfluoride glass ceramics by thermal induction and corrosion treatment”, *Nanoscale Res. Lett.* 3(12), 516-520 (2008).
22. Li Zu-Bin, Yang Yi-Hong, Kong Xiang-Tian, Zhou Wen-Yuan, Tian Jian-Guo, “Enhanced transmission through a subwavelength slit surrounded by periodic dielectric bars above the metal surface”, *J. Opt.* A. 2008, 10, 095202.
23. Zhibo Liu, Xiaoqing Yan, Wenyuan Zhou, and Jianguo Tian, Evolutions of polarization and nonlinearities in an isotropic nonlinear medium, *Opt. Express* 16(11), 8144-8149(2008). *
24. D. Song, C. Lou, L.Tang, X. Wang, W. Li, X. Chen, K. Law, H. Susanto, P. G. Kevrekidis, J. Xu, and Z. Chen, “Self-trapping of optical vortices in waveguide lattices with self-defocusing nonlinearity”, *Opt. Express* 16, 10110 (2008). *
25. Shuanggen Zhang, Jianghong Yao, Weiwei Liu, Zhangchao Huang, Jue Wang, Yongnan Li, Chenghou Tu, Fuyun Lu, “Second harmonic generation of periodically poled potassium titanyl phosphate waveguide using femtosecond laser pulses”, *Opt. Express* 16(18):14180-14185(2008).
26. Peng Zhang, Jianlin Zhao, Fajun Xiao, Cibo Lou, Jingjun Xu and Zhigang Chen, “Elliptical

discrete solitons supported by enhanced photorefractive anisotropy", *Opt. Express* 16, 3865(2008).

27. Zu-Bin Li, Jian-Guo Tian, Wen-Yuan Zhou, Wei-Ping Zang, Chun-Ping Zhang, "Enhanced and confined light transmission through a funnel-type aperture with a sub-wavelength outlet", *Opt. Commun.* 281, 2321-2325(2008).
28. Yong-Liang Liu, Zhi-Bo Liu, Jian-Guo Tian, Yan Zhu, Jian-Yu Zheng, "Effects of Metallization and Bromination on Nonlinear Optical Properties of Diphenylporphyrins", *Opt. Commun.* 281: 776-781(2008).
29. Shengwen Qi, Yongliang Liu, Xiuqin Yang, Tang Xu, Guiying Chen, Chunping Zhang, Jianguo Tian, "Measurement of nonlinear refractive index of ethyl red by interference of capillary", *Opt. Commun.* 281(23):5902-5905(2008).
30. Shu-jing Liu, Feng Song, Hong Cai, Teng Li, Bin Tian, Zhao-hui Wu and Jian-guo Tian , " Effect of thermal lens on beam quality and mode matching in LD pumped Er–Yb-codoped phosphate glass microchip laser " , *J. Phys.* D: Appl. Phys. **41** 035104 (6pp) (2008).
31. Xiao-chen Yu, Feng Song , Wen-tao Wang , Lan-jun Luo , Lin Han, Zhen-zhou Cheng, Tong-qing Sun, Jian-guo Tian, and Edwin. Y. B. Pun2 , " Comparison of optical parameters and luminescence between Er^{3+}/Yb^{3+} codoped phosphate glass ceramics and precursor glasses ", *Journal of Applied Physics* 104, 113105 (2008).
32. Meixiu Sun, Chunping Zhang, Shengwen Qi, Qing Ye, Jianguo Tian, "Effect of surface roughness of incident region on determination of tissue properties", *Journal of Modern Optics* ，Vol.55,No.8，1219-1229(2008).
33. Hua Yu, Kai-Di Zhou, Kai Chen, Jie Song, Chun-Xiao Hou, and Li-Juan Zhao, "Investigation on crystallization process in oxyfluoride glass ceramics codoped with Er^{3+}/Yb^{3+}", *J. Non-Cryst. Solids* 354,3649-3652 (2008).
34. J.M.Sun, M. Helm, W. Skorupa, B. Schmidt, and A. Mücklich, "Light emission from ion-implanted silicon", *Physica Status Solidi* (c)(Proceedings of Silicon Age 3),Article No. pc80710 (2008).
35. S.Prucnal, J.M.Sun, L.Rebohle,andW.Skorupa,"Energy transfer from Gd to Er atoms in SiO2(GdEr)-MOSLEDs produced by ion implantation", *Materials Science and Engineering* B 146, 241-244(2008).
36. Ci-bo LOU, Li-qin TANG, Dao-hong SONG, Xiao-sheng WANG, Jing-jun XU, Zhi-gang CHEN, "Novel spatial solitons in light-induced photonic bandgap structures", *Front. Phys. China* 3(1): 1—11(2008).
37. H. Susanto, K. Law, P. G. Kevrekidis, L.Tang, C. Lou, X. Wang, and Z. Chen, "Dipole and quadrupole solitons in optically induced two-dimensional defocusing lattices", *Physica* D 237, 3123 (2008).
38. Yanfeng Zhang, Yudong Li, Jiwei Qi, Guoxin Cui, Hongbing Liu, Jing Chen, Lihua Zhao, Jingjun Xu, Qian Sun, "Influence of absorption on optical trapping force of spherical particles in a focused Gaussian beam", *J. Opt.* A: 10, 085001(2008).
39. Li Xiao-Chun, Kong Yong-Fa, Wang Li-Zhong and Liu Hong-De, "The two photorefractive centres in iron doped nearly stoichiometric lithium niobate crystals", *Chinese Phys.* B 17(3), 1014-1019 (2008).

40. Wei Li, Xinzheng Zhang, Yanli Shi, Jingjun Xu, Haijun Qiao, Qiang Wu, Romano A. Rupp, Cibo Lou, Zhenhua Wang, Feng Gao, Baiquan Tang, Christian Pruner, "Photopolymerization-Induced Two-Beam Coupling and Light-Induced Scattering in Polymethyl Methacrylate", *Chin. Phys. Lett.* 25(8), 2857-2859 (2008).
41. Xinzheng Zhang, Zhenhua Wang, Hui Li, Qiang Wu, Bqiquan Tang, Feng Gao, and Jingjun Xu, "Characterization of Photon Statistical Properties with Normalized Mandel Parameter", *Chin. Phys. Lett.* 25(11), 3976-3978 (2008).
42. Fei bian, Xinzheng Zhang, Zhenhua Wang, Qiang Wu, Hao Hu, Jingjun Xu, "Preparation and size characterization of silver nanoparticles produced by femtosecond laser ablation in water", *Chin. Phys. Lett.* 25(12) 4463-4465 (2008).
43. ZHANG Shuang-Gen, YAO Jiang-Hong,SHI Qing, LIU Yan-Ge, LI Yong-Nan, TU Cheng-Hou, GUO Wen-Gang, LU Fu-Yun, "Fibre-Format Photonic Source Based on Efficient Frequency Doubling of Continuous-Wave Erbium-Fibre Laser Amplifier", *Chin. Phys. Lett.* 25(8):2873-2875(2008).
44. YAO Jiang-Hong, JIA Guo-Zhi, ZHANG-Yan, LI Wei-Wu,SHU Yong-Chun,WANG Zhan-Guo,XU Jing-Jun， "Resonant Tunnelling in Barrier-in-Well and Well-in-Well Structures"，*Chin. Phys. Lett.* 25(12):4391-4393(2008).
45. Gan Zongsong, Yu Hua, Li Yanming, Wang Yanan, Chen Hui, Zhao Lijuan, "Investigation on up-conversion luminescence of Tm3+ and Yb3+ codoped oxy-fluorosilicate glass ceramics" *Acta Phys. Sin.* 57(9), 5700-4 (2008).
46. Shuanggen Zhang, Jianghong Yao, Yaxian Fan, Weiwei Liu, Yange Liu, Qing Shi, Zhangchao Huang, Fuyun Lu, Second harmonic generation in periodically poled lithium niobate waveguide using femtosecond laser pulses, Proc.SPIE 7: 1357-1359(2008).
47. Sun Xiufeng, Xu Xiaoxuan, Fan Wei, "The Optimization Of The Beam Of The Laser", Proceedings of SPIE- The International Society for Optical Engineering, v 6824, Semiconductor Lasers and Applications III, p 68241V(2008).
48. Fan Wei, Xu Xiaoxuan, Sun, Xiufeng, "Temperature dependence of PL spectrum in researching InGaAs/GaAs single quantum well", Proceedings of SPIE-The International Society for Optical Engineering, v 6838, Optoelectronic Devices and Integration II, p68380S(2008).
49. Xiaoxuan Xu, Zhe Qin, Haibo Lin, Wei Xu, "Study on the degradation of PLEDs by in-situ micro-Raman spectroscopy"，Proceedings of SPIE - TheInternational Society for Optical Engineering, v 6828, Light-Emitting Diode Materials and Devices II, p 68280R(2008).
50. 付博，张国权，刘祥明，申岩，徐庆君，孔勇发，陈绍林，许京军，"掺杂对铌酸锂晶体非挥发全息存储性能的影响"，物理学报 57（5）， 2946-2951（2008）。
51. 甘棕松，余华，李妍明，王亚楠，陈晖，赵丽娟，"Tm^{3+}/Yb^{3+}共掺氟氧硅铝酸盐玻璃陶瓷蓝色上转换发光研究"，物理学报，57（9），5699-5704（2008）。
52. 楼慈波、宋道红、唐莉勤、陈星宇、许京军、陈志刚，"光子晶格中新颖的空间带隙孤子"， 物理 37（4），239（2008）。
53. 龙绘锦，孟庆巨，元晶，曹亚安，"B 离子掺杂 TiO_2 催化剂($TiO_{2-x}B_x$)光催化活性的研究"，化学学报，66，657-661（2008）。
54. 罗大超，张兰兰，龙绘锦，陈咏梅，曹亚安，"镍离子表面处理对二氧化钛光催化活性的影响"，物理化学学报，24，1095-1099（2008）。

55. 申岩，张国权，许京军，张宇，孙秀东，赵业权，周羚君，“开路光伏孤子的动态行为”，光学学报 28（3），528-533（2008）。
56. 邓浩亮，姚江宏，“双模自组织量子点光致发光的温度依赖性”， 发光学报, 29（6），1023-1026（2008）。
57. 刘迎军，许棠，张春平，郝召锋，“掺杂浓度与溶液对偶氮聚合物薄膜全光开关特性的影响”，光子学报，37（2），252-255（2008）。
58. 范伟，徐晓轩，孙秀峰，“InGaAs/GaAs 单量子阱 PL 谱的温度变化特性”，光散射学报，20（2），182-186（2008）。
59. 邓大为，宋宁，李奇楠，徐晓轩，张存洲，“小波变换在岩屑样品红外漫反射光谱中的应用”，光谱学与光谱分析，28（1），37-40 （2008）。
60. 宋宁，徐晓轩，武中臣，张存洲，“DWT-iPLS 在漫反射光谱数据处理中的应用”，光谱学与光谱分析，28（8），1846-1850（2008）。
61. 秦哲，许伟，王斌，孙秀峰，徐晓轩，俞钢，张存洲，“新型共轭聚合物 PFO=BT15 发光二极管的电老化研究”，光谱学与光谱分析，28（8），1741-1744（2008）。
62. 王斌，徐晓轩，秦哲，宋宁，张存洲，“金属-砷化镓界面的电调制反射光谱 Franz-Keldysh 效应研究”，光谱学与光谱分析，28（8），1701-1704（2008）。
63. 王斌，徐晓轩，秦哲，宋宁，张存洲，“分子束外延 nGaAs/SI-GaAs 薄膜材料的拉曼光谱研究”，光谱学与光谱分析，28（9），2107-2110（2008）。
64. 张双根，姚江宏，李勇男，涂成厚，郭文刚，黄章超，吕福云，“基于周期极化晶体的 QPM-SHG 技术发展及其应用”，红外与激光工程， 37（2），233-236（2008）。
65. 张艳峰，李玉栋，赵立华，刘洪冰，陈靖，崔国新，许京军，孙骞，“环形光束中双层球的光俘获”， 南开大学学报，41（3）（2008）。
66. Jing Chen, Yudong Li, Yanfeng Zhang, Hongbing Liu, “Analysis on an Array of Nano-waveguide”, 南开大学学报 41（4）（2008）。

书籍出版情况/Publications of Book

1. J. Yang, X. Wang, J. Wang, and Z. Chen, “Light localization by defects in optically induced photonic structures”, Invited Book Chapter, in Nonlinearities in Periodic Structures and Metamaterials", C. Denz, S. Flach, and Y. Kivshar ed., (Springer, 2008).

专利/Patents

申请专利/ Patents Applied

[1] CN 101266209A；激光衍射测量周期极化晶体参数的方法；发明；高峰，许京军，张国权，姚江宏，张文定，刘海旭。

[2] CN 101266320A；自泵浦延迟可调光脉冲群速延迟器；发明；高峰，许京军，张国权，薄方。

[3] CN 101257180A；一种超短长度铒镱共掺高增益玻璃光纤超荧光光源；发明；宋峰，程振洲，邹昌光，韩 琳，于晓晨，张家祥，蒋雪萍，田建国。

[4] CN 101186435A；一种光纤预制棒的新型制作方法；发明；宋峰，程振洲，邹昌光，于晓晨，张家祥，蒋雪萍，田建国。

[5] 200810153618.6；一种光诱导光折变晶体表面微结构的方法；发明；王俊俏，张心正，谭信辉，许京军，吴强，王振华，唐柏权，孙骞，孔勇发。

[6] 200810052869.5；高效率纳米 Ti1-XO_2-SnX/ TiO_2-X-NX 复合薄膜可见光催化剂的制备方法；发明；曹亚安，曹永强，王恩君。

[7] 200810053738.9；高效率金属、非金属离子共掺杂纳米 TiO_2 可见光催化剂的制备方法；发明；曹亚安，曹永强，龙绘锦。

[8] 200810053737.4；一种掺杂二氧化钛纳米管的制备方法；发明；曹亚安，龙绘锦，曹永强。

[9] 200810053555.7；基于频域 OCT 的生物组织折射率测量方法；发明；叶青，周文远，田建国。

[10] 200810053556.1；多波长 OCT 系统；发明；叶青，周文远，田建国。

[11] 200810053557.6；用于双波长 OCT 系统的聚焦镜头；发明；叶青，周文远，刘宇，田建国。

[12] 200820075056.3；双波长 OCT 系统；实用新型；叶青，周文远，田建国。

[13] 200820075057.8；多波长 OCT 系统的聚焦镜头；实用新型；叶青，周文远，刘宇，田建国。

[14] 200720096496.2；牛角形光导管装置；实用新型； 张春平，田建国，郭磊，叶青，傅汝廉。

授权专利/ Patents Approved

[1] ZL02148631.X 一种近场扫描光学显微镜定位扫描成像方法；发明；张天浩，吴朝晖，张春平，张光寅，颜彩繁。

[2] ZL200720096684.5；新型光纤涂敷系统；实用新型；宋峰，程振洲，邹昌光，苏瑞渊，于小晨，张家祥，蒋雪萍，田建国

国际合作与交流/International Cooperation and Exchange

来访人员名单/Visitors List

序号	姓名	国家或地区	单位	职称或职位	来访时间	来访目的
1.	Victor Zadkov	俄罗斯	莫斯科大学物理系	教授	2008.11	学术交流
2.	S.Jiang	美国	Optical Sciences Center in University of Arizona	Associate Professor	2008.9	学术交流
3.	Germano Montemezzani	法国	University Paul Verlaine Metz	教授	2008.10.2-10	合作研究，讲学
4.	Tatiana Volk	俄罗斯	俄罗斯国家晶体研究所	教授	2008.10.14-11.13	讲学，合作研究
5.	Peter Gunter	瑞士	瑞士苏黎世联邦工业大学（ETH）	教授	2008.11.2-7	讲学
6.	Mordechai Segev	以色列	Physics Department and Solid State Institute, University of Haifa	教授	2008.6.12-14	讲学
7.	William Firth	英国	Department of Physics, Glasgow	教授	2008.6.12-14	讲学
8.	Eugenio Del Re	意大利	Electrical and Information Engineering Department, University of L'Aquila	教授	2008.6.12-14	讲学
9.	D. Kip, Clausthal-Zellerfeld	德国	Institute of Physics and Physical Technologies, Clausthal University of Technology, Clausthal-Zellerfeld	教授	2008.6.12-14	讲学
10.	R. Morandotti, Varennes	加拿大	Ultrafast Optical Processing Research Group, INRS-EMT, Université du Québec	教授	2008.6.12-14	讲学
11.	Dmitry Skryabin	英国	Centre for Photonics and Photonic Materials, Department of Physics, University of Bath	教授	2008.6.12-14	讲学

12.	Stefano Trillo	意大利	Department of Engineering, University of Ferrara	教授	2008.6.12-14	讲学
13.	Irena Drevenšek-Olenik	斯洛文尼亚	Stefan 研究所	教授	2008.2.25-3.3	合作研究
14.	Miha Devetak	斯洛文尼亚	Stefan 研究所	博士生	2008.8.26-9.5	合作研究
15.	Daniel R. Grischkowsky	美国	俄克拉何马州立大学	教授	2008.10.31	学术交流
16.	Christian Erwin Rüeter	德国	Clausthal 工业大学	博士	2008.11.17-23	工作访问
17.	Junru Wu	美国	University of Vermont	教授 系主任	2008.7.10-11	讲学
18.	Christian Rueter	德国	Technical University of Clausthal	Post Doc.	2008.11	学术交流

出访人员名单/Personnel exchange Researchers List

序号	姓名	国家或地区	单位	职称或职位	出访时间	出访目的
1.	宋　峰	香港	香港城市大学	教授	2008.3	学术访问
2.	赵丽娟	德国	洪堡大学	教授	2008.10-2009.1	合作研究
3.	张国权	斯洛文尼亚	卢布尔雅那大学	教授	2008.9.20-26	合作研究，讲学
4.	孙　骞	克罗地亚	克罗地亚物理学会	教授	2008.5	IYPT 竞赛
5.	张心正	斯洛文尼亚	Stefan 研究所	副教授	2008.9.20-26	学术访问
6.	Romano A. Rupp	韩国	釜山国立大学	教授、院长	2008.10.27-31	国际研讨会
7.	吴　强	美国	Tufts&MIT	讲师	2007.1-2008.4	博士后

研究生交流情况/Personnel exchange Students List

序号	姓名	国家或地区	单位	博士生/硕士生	出访时间	出访目的
1.	韩　琳	美国	亚利桑那大学光学中心	博士生	2007.9-2009.3	学习访问

2.	齐新元	澳大利亚	澳大利亚国立大学	博士生	2008.9	联合培养
3.	蔡　卫	西班牙	CSIC光学研究所	博士生	2008.4.7-2008.7.4	合作研究
4.	蔡　卫	西班牙	CSIC光学研究所	博士生	2008.9.29-2008.12.28	合作研究
5.	吴　限	韩国	釜山国立大学	博士生	2008.10.27-2008.10.31	国际研讨会
6.	王文杰	澳大利亚	国立大学	博士生	2008.9	联合培养

引进人才名单/New Staff

序号	姓名	性别	出生年月	职称	研究方向
1	叶　青	男	1981.5	讲师	生物医学光子学
2	王振华	男	1979.5	讲师	光子学与技术
3	齐继伟	男	1978.10	讲师	非线性光学

国内、国际会议报告/Talks at Conferences

1. Z. Chen, “Discrete solitons and singularity formation in reconfigurable photonic lattices", the International Conference on Nonlinear Waves--Theory and Applications, Beijing, June 2008. (invited)
2. 孙甲明，Light emission from ion-implanted silicon. 2008 2008 Sino-German Symposium on silicon optoelectronics， 杭州 9-14th June 2008. (邀请报告)
3. Daohong Song, Liqin Tang, Cibo Lou, Xiaosheng Wang, Jingjun Xu and Zhigang Chen H. Susanto, K. Law and P.G.. Kevrekidis "Self-trapping of optical vortices in photonic lattices optically induced with self-defocusing nonlinearity ", CLEO/QELS 2008, San Jose ,USA
4. Fei bian, Xinzheng Zhang, Zhenhua Wang, Qiang Wu, Hao Hu, Jingjun Xu, “*Preparation and size characterization of silver nanoparticles produced by femtosecond laser ablation in water*”, The OSA Topical Conference on Nanophotonics, Nanjing, May 26-29, 2008
5. Yi Hu, Cibo Lou, Sheng Liu, Peng Zhang, Jianlin Zhao, Jingju Xu, Zhigang Chen， "Observation of discrete and gap soliton trains in light-induced 2D photonic lattices under an identical bias condition", The OSA Topical Conference on Nanophotonics, Nanjing, China, May 26-29(2008)
6. Zhi-Bo Liu, Jian-Guo Tian, Zhen Guo, Dong-Mei Ren, Jian-Yu Zheng, “Nonlinear Absorption and Optical Limiting Effects in Porphyrin Covalently Functionalized Single-Wall Carbon Nanotubes”, The OSA Topical Conference on Nanophotonics’08, Nanjing, Jiangsu, China, May 26-29(2008).
7. Kaidi Zhou, Jie Song, Kai Chen, Lijuan Zhao, Hua Yu, “Study on Synthesis and Optical Characters of ZnS Quantum Dots”, The OSA Topical Conference on Nanophotonics’2008, Nanjing China (May 26-29, 2008).
8. 张雁，姚江宏，Resonant Tunnelling in Barrier-in-Well and Well-in-Well Structures, The OSA Topical Conference on Nanophotonics’2008, Nanjing China (May 26-29, 2008).
9. 徐晓轩，“近红外光谱仪器一些新进展”，第二届全国近红外光谱学术会议，长沙（2008.11.19-23）。（大会报告）
10. 田建国，杨一宏，李祖斌，“具有腔结构的亚波长狭缝的透射特性”，中国物理学会2008年秋季学术会议，济南（2008.9.19-21）（邀请报告）
11. 宋峰，“稀土光学材料的荧光测量”，第七届爱丁堡荧光光谱年会，杭州（2008，10）。(邀请报告)
12. 宋峰，“高增益短长度掺铒光纤激光器”、“小型自动化光纤拉丝系统的研制”，第三届全国光机电技术与系统集成学术会议、第十三届全国光电技术与系统学术会议，南京（2008.9）。(邀请报告)
13. 孙甲明，刘海旭，张俊杰，杨阳，张新霞，W. Skorupa，M. Helm, “稀土离子注入的高效率硅基纳米材料电致发光器件”，第二届全国掺杂纳米材料发光性质学术会议，珠海（2008.11.23-29）。 (邀请报告)
14. 楼慈波，唐莉勤，宋道红，陈志刚，“光诱导微结构中的局域态研究”，第十四届国际激光科学研讨会，广州-珠海 2008.12.4-2008.12.8
15. Qi Yiling, Anas F. Jarjour, Wang Xu, Robert A.Taylor and Zhang Guoquan, “Theoretical simulation of optical transmission in 2D photonic crystal slab with MEEP”, 2008 中国光学年会，泉州（2008.11.20-25）。

16. 张文定，高峰，张国权，许京军，“聚焦高斯光束的傍轴能量传输和群速调控”，2008 中国光学年会，泉州（2008.11.20-25）。
17. Daohong Song, Cibo Lou, Liqin Tang, Jingjun Xu, Zhigang Chen “Observation of gap vortex solitons in optically induced photonic lattice with a defocusing nonlinearity”，第十四届全国凝聚态光学性质学术研讨会(OPCM’2008)，青岛（2008.7.25-27）。
18. 齐新元，张国权，高峰，薄方，许宁宁，刘海旭，“光波在（2+1）维光感应光子晶格中的传输现象的研究”，第十四届全国凝聚态光学性质学术研讨会(OPCM’2008)，青岛（2008.7.25-27）。
19. 张文定，高峰，张国权，许京军，“基于类简并二波耦合机制的聚焦高斯光束的旁轴能量传输”，第十四届全国凝聚态光学性质学术研讨会(OPCM’2008)，青岛（2008.7.25-27）。
20. 赵立华，李玉栋, 张艳峰, 许京军, 孙骞, “基于平行纳米光波导的定向耦合器的性质研究”，第十四届全国凝聚态光学性质学术研讨会(OPCM’2008)，青岛（2008.7.25-27）。
21. 齐继伟，李玉栋，吴晶，高峰，孔凡磊，孙立萍，赵立华，许京军，孙骞， “磁场作用下的光折边光栅擦除过程研究”，第十四届全国凝聚态光学性质学术研讨会(OPCM’2008)，青岛（2008.7.25-27）。
22. 陈靖，李玉栋，陆文强，齐继伟，崔国新，刘洪冰，许京军，孙骞，“铌酸锂-金属薄膜复合结构激发表面等离子激元的研究”，第十四届全国凝聚态光学性质学术研讨会(OPCM’2008)，青岛（2008.7.25-27）。
23. 谢楠，李玉栋，许京军，孙骞， “亚波长尺度布拉格光栅的光谱特性”，第十四届全国凝聚态光学性质学术研讨会(OPCM’2008)，青岛（2008.7.25-27）。
24. 楼慈波、胡毅、陈志刚、许京军、刘圣、张鹏、赵建林“光诱导复式非线性光子晶格中的空间孤子”，第十四届全国凝聚态光学性质学术研讨会(OPCM’2008)，青岛（2008.7.25-27）。
25. 陈凯，赵丽娟，卢璟，马冬林，宋令枝，张新星，“单轴晶体中有效非线性系数的色散特性研究”，第十四届全国凝聚态光学性质学术研讨会(OPCM’2008)，青岛（2008.7.25-27）。
26. 李威，唐柏权，张心正，刘龙昌，郭尚雨，许京军，“紫外光敏有机玻璃研究”，第十四届全国凝聚态光学性质学术研讨会(OPCM’2008)，青岛（2008.7.25-27）。
27. 王俊俏，张心正，吴强，许京军，“Forming of particles rating on the surface of the photorefractive crystals using dielectrophoresis and electrophoresis effect”，第十四届全国凝聚态光学性质学术研讨会(OPCM’2008)，青岛（2008.7.25-27）。
28. 吴强，许京军，Christopher Werley, Kung-Hsuan Lin, Eric Statz, and Keith Nelson，“声子极化激元的时间分辨定量二维成像”，第十四届全国凝聚态光学性质学术研讨会(OPCM’2008)，青岛（2008.7.25-27）。
29. 陆文强，陈桂英，张春平，田建国，“提高掺杂 PMMA 的偶氮材料-乙基红薄膜全光开关调制度的研究”，第十三届全国基础光学与光物理学术讨论会，海拉尔（2008.7.26-27）。
30. 孙甲明，“离子注入高效率硅材料电注入发光器件的进展”， 2008第二届硅基光电子材料及器件会议，杭州（ 2008.6.12-15）。
31. 张新霞，孙甲明，张俊杰，杨阳，刘海旭, “半绝缘Si/SiO_2 超晶格结构在交流电场下的电致发光特性”，2008第二届硅基光电子材料及器件会议，杭州杭州（ 2008.6.12-15）。
32. 张俊杰，孙甲明，杨阳，张新霞，刘海旭，W. Skorupa，M. Helm，“纳米硅微晶对于Er离子掺杂的SiO_2薄膜的光致发光和电致发光的不同影响”， 2008第二届硅基光电子材料及器件会议，杭州（ 2008.6.12-15）。

33. 杨阳，孙甲明，张俊杰，张新霞，刘海旭，W. Skorupa，M. Helm, “离子注入缺陷局域掺杂的高效率硅pn结发光二极管”，2008第二届硅基光电子材料及器件会议，杭州（ 2008.6.12-15）。
34. 于晓晨，“Er^{3+}/Yb^{3+}共掺磷酸盐玻璃陶瓷的红外发光特性研究”，山东大学物理年会，济南（2008.9）。

主办国内、国际会议/Conferences Sponsored by the Laboratory

1. **离散光学专题讲座**（2008.6.12-13；天津）

2008 离散光学专题讲座于 6 月 13 日在南开大学泰达应用物理学院举行，超过 100 名相关领域的师生参加了此次讲座。

南开大学副校长许京军教授为本次讲座做了热情洋溢的欢迎辞。随后，来自以色列 University of Haifa、意大利 University of L'Aquila、德国 Clausthal University of Technology、加拿大 Université du Québec、英国 University of Bath、意大利 University of Ferrara 等大学的八位世界顶级专家作了精彩的报告。各位专家深入浅出地为大家展示了离散光学和光子学以及相关学科的基础概念以及相关课题的国际研究热点，讲座给在场的每个人留下了深刻的印象。在场的观众纷纷利用这个难得的机会同专家们就这个具有挑战性领域的发展趋势、创新思想以及应用前景展开了热烈的讨论。

这次专题讲座促进了中国和世界间相关领域的学术交流，也促成了南开大学和国外八所著名大学之间的良好合作关系，同时也为国内的研究者和世界顶级科学家之间搭建起了合作的桥梁。

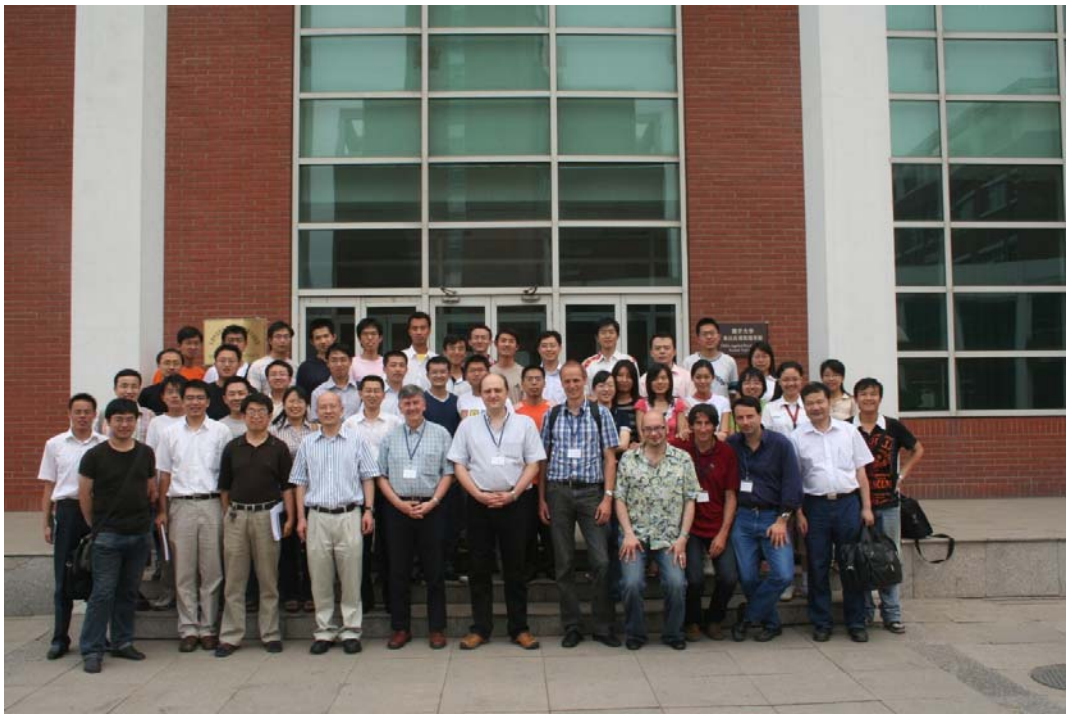

南开大学弱光非线性光子学教育部重点实验室/ The Key laboratory of Weak Light Nonlinear Photonics (Nankai University, Tianjin 300457), Ministry of Education, China

2. 第十四届全国凝聚态光学性质学术研讨会（OPCM’2008）（2008.7.25-27；青岛）

受中国物理学会委托，南开大学和青岛大学共同主办的第十四届全国凝聚态光学性质学术会议于 2008 年 7 月 25 日至 7 月 27 日在青岛大学国际学术交流中心召开，对近年来凝聚态光学性质及其应用领域中学术研究和技术进步成果进行了一次全面、集中并具有权威性的总结和交流。

大会共设置 5 个大会邀请报告，6 个分会邀请报告，共设置 6 个分会场，分别为凝聚态光子学器件分会场，半导体材料及性质分会场，凝聚态材料及性质分会场，凝聚态材料与器件光学性质分年会场，凝聚态光谱分会场及凝聚态光学新效应、新机制分会场，并设置张贴报告。会议收到学术论文 136 篇。参加会议正式代表 130 人。会议代表来自 4 个国家，包括中国、奥地利、美国及英国，代表分属 38 个高校及科研院所，包括南开大学、复旦大学、厦门大学、南京大学、中科院物理所、中科院半导体所、中科院上海技物所等。

会议对凝聚态光学材料、性质及其应用进行了广泛的交流。与会人员对长余辉磷光材料、纳米半导体材料等凝聚态光学材料的制备和性质研究进行了深入的讨论。凝聚态光学材料中的负折射率效应等新型非线性光学效应受到了与会者的关注，与会者认为这些新效应将有助于新型凝聚态光学器件的研发。会议增进了国内各单位之间的了解，会议代表探讨了凝聚态光学的最新进展与前沿研究，取得了良好的效果。

中国物理学会/ Chinese Society of Physics

南开大学弱光非线性光子学教育部重点实验室/ The Key laboratory of Weak Light Nonlinear Photonics (Nankai University, Tianjin 300457), Ministry of Education, China

3. 先进光子学材料与技术讲习班（2008.7.27-8.8；天津）

由国家自然科学基金委员会主办，南开大学承办的《先进光子学材料与技术讲习班》于 2008 年 7 月 27 日至 8 月 8 日在南开大学泰达应用物理学院举行。

光子学与技术是多学科交叉领域，不仅对信息科学、物理学、材料科学及其他相关学科的发展起到了重要的推动作用，而且直接促进技术进步、社会的发展、国民经济的增长和国防建设。此次讲习班旨在进一步加强学科之间的交流和融合，培养和造就一批掌握先进光子学与技术基本知识和先进技术，符合社会发展需求的高级后备人才，推动高新技术产业和国民经济的进一步发展。

《先进光子学材料与技术讲习班》主要内容包括《微纳光子学与技术》、《先进光子学材料》、《现代光通讯技术》、《量子相干器件与量子信息》和《固态激光技术及其应用》等 5 个专题，共邀请国内外专家学者 19 人为讲习班授课，其中包括中科院院士 3 人。我们在南开大学相关领导，尤其是科技处的支持下，扩大了招生的规模。参加讲习班的学员实际注册人员达 230 余人，学员中绝大部分为博士研究生，有 20 余位青年教师和博士后研究人员。学员分别来自北京大学、清华大学、南开大学、南京大学、复旦大学、上海交通大学、中山大学、浙江大学、山西大学、中科院物理所、西安光机所和上海技术物理研究所等 24 个高校和科研院所

讲习班在课程安排上充分考虑了学术交流的重要性，在每位专家授课之后均安排了专门的自由讨论时间，以方便学员与学员之间以及学员与主讲专家之间的交流，取得了良好的效果。为了方便大家了解讲习班的基本情况以及讲习班的筹备情况，我们专门开通了讲习班的网页（http://teda.nankai.edu.cn/aps/photonics/index.html）。讲习班网页的建设为此后的报名和组织起到了积极的作用。同时，为了方便学员回原单位后进一步学习讲习班上的授课内容，巩固讲习班已经取得的成果，扩大讲习班的受益范围，我们将授课教师的课件均传到讲习班的主页上，以方便学员和相关科研人员下载。

值得一提的是，本次讲习班还引起德国 DAAD 学术交流中心的高度关注，该中心派专人（奖学金项目主任郑怡女士）来讲习班为学员介绍德国留学和学术交流方面的情况。

国家自然科学基金委员会/NSFC
南开大学/Nankai University
南开大学弱光非线性光子学教育部重点实验室/ The Key laboratory of Weak Light Nonlinear Photonics (Nankai University, Tianjin 300457), Ministry of Education, China

学术组织与期刊任职/Academic Service

国内学术组织任职/Service to the Domestic Professional Societies

序号	姓名	任职机构	职位	任期
1	许京军	中国高校知识产权研究会	副理事长	2008-
2	许京军	天津市物理学会	理事长	
3	宋　峰	中国仪器仪表学会光机电技术与系统集成分会	第一届常务理事	2006-2010
4	孔勇发	中国材料研究学会青年工作委员会	理事	2008－2011
5	孔勇发	天津市硅酸盐学会	晶体生长与材料专业委员会副主任	2005-
6	孙　骞	天津市光电子学会	常委	2006-
7	宋　峰	教育部高等学校物理基础课程教学指导分委员会	委员，高等学校文科类物理课程教学研究协作组成员	2006-2010
8	宋　峰	教育部大学物理基础课程教指委暨医药类基础课程教指委 医药物理协作组	副组长	2008-2010
9	徐章程	中国教育技术协会多元智能专业委员会	主任	2008-2009
10	徐章程	中国电子学会半导体集成分会	委员	2007-
11	孙　骞	中国光学学会光电技术委员会	委员	2006-
12	宋　峰	固体激光技术国防科技重点实验室	第三届学术委员会委员	2007-2010
13	宋　峰	南京师范大学物理系	兼职教授	2006-2010
14	宋　峰	德州学院物理系	兼职教授	2007-2011
15	宋　峰	南通大学	兼职教授	2008-2012

国内期刊任职/Service to the Domestic Journals

序号	姓名	任职机构	职位	任期
1	许京军	Frontiers of Physics in China-Selected publications from Chinese Universities	编委	2005-
2	许京军	《光学学报》	副主编	
3	许京军	《红外与毫米波学报》	编委	
4	许京军	《物理》	编委	
5	孔勇发	《激光技术》	编委	2006-2010
6	张国权	《激光技术》	编委	2007-2011
7	孙骞	《激光技术》	编委	2006-2010

获奖情况/Awards & Honors

2008 全国工人先锋号

获奖者：弱光非线性光学教育部创新团队

2008 全国五一劳动奖状

获奖者：弱光非线性光学教育部创新团队

光诱导光子晶格中非线性空间频谱整形和带隙孤子串的实现

“2007 年中国光学重要成果” 奖

获奖者：楼慈波　许京军　陈志刚

Band-Gap Engineering and Light Manipulation With Egg-Crate Photonic Lattices

Optics in 2008 -《Optics & Photonics News》

winner：Group of Weak-Light Nonlinear Optics and Quantum Coherent Optics

获奖个人/Award for distinguished scientists

2008 天津市优秀留学回国人员

获得者：徐章程

南开大学第四届教学名师奖

获得者：宋　峰

南开大学第二届“良师益友”

获得者：宋　峰

获奖学生/Award for excellent students

南开大学三好学生：　李　辉

南开大学优秀学生干部：　李　威

南开大学优秀毕业生：　邹昌光　宋　杰

南开大学优秀党员：　刘龙昌

南开大学奖学金：

一等奖学金：　程振洲　徐　燕　杨程亮　张雅婷

二等奖学金：　杨一宏

三等奖学金：　李　伟　李　辉　王　喆　郭尚雨

金妮娜　齐新元　张文定　李昕睿

学位论文/Dissertations

1. 博士学位论文 Dissertation for Doctoral Degree

[1] 陈　靖 周期性微结构光学性质的研究；导师：许京军、孙骞

[2] 张艳峰 光镊理论模型若干问题研究；导师：孙骞

[3] 刘洪冰 基于马赫-曾德尔外差干涉仪的光偏振态测量技术研究；导师：孙骞

[4] 叶　青，多功能光学相干层析系统及其应用研究；导师：田建国

[5] 张　冰，有机材料非线性光频特性研究；导师：田建国

[6] 柳永亮，光限制器的理论和实验研究；导师：田建国

[7] 孙美秀，光在生物组织中的传输与生物组织光学性质的研究；导师：张春平

[8] 刘如斌，GaAs 基低维应变异质结和多周期结构的 MBE 制备及特性研究；导师：王占国

[9] 刘淑静，LD 抽运铒镱共掺磷酸盐玻璃激光器上转换及热效应的研究；导师：宋峰

2. 硕士学位论文 Dissertation for Master Degree

[1] 刘祥明，铌酸锂晶体的紫外光折变效应及光霍尔效应研究；导师：张国权

[2] 刘海旭，光波耦合过程中的色散调控研究；导师：张国权

[3] 陈　聪，∧型三能级体系中电磁感应透明效应的研究；导师：张国权

[4] 陈星宇, 光子晶格中的带隙孤子和矢量孤子的研究；导师: 陈志刚

[5] 陈　楠，飞秒激光在光子晶格中传播特性的研究；导师：许京军、吴强

[6] 安亚男，铌酸锂晶体抗光折变的微观机理研究；导师：孔勇发

[7] 林军海，铌酸锂晶体中脉理条纹的研究；导师：孔勇发

[8] 马晓明，纳米材料的非线性光学性质研究；导师：徐章程

[9] 宋　杰，ZnS 量子点生物荧光探针的制备与特性研究；导师：赵丽娟

[10] 王红旗，近化学计量比掺镁铌酸锂晶体制备及其周期极化；导师：张玲

[11] 王玲玲，纳米结构二氧化钛可见光催化剂的制备及其性能研究；导师：曹亚安

[12] 吴胜青，锆铁双掺铌酸锂晶体的生长及其光折变性能研究；导师：刘士国

[13] 张　玲，导电聚合物/量子点复合材料中的能量转移；导师：徐章程

[14] 赵延雷，铒镱双掺钨酸镧钾晶体生长及光谱性质研究；导师：孙同庆

[15] 陈天琳，光诱导铌酸锂晶体极化畴反转的研究；导师：陈云琳

[16] 方扩军，群速度匹配宽带激光频率变换技术的研究；导师：陈云琳

[17] 李福新，双波长光学相干层析成像系统的研究；导师：田建国

[18] 刘　宇， 光学相干层析系统设计与应用研究；导师：田建国

[19] 钱　坤，利用倾斜入射光路测量与分析生物组织的光学特性参数；导师：田建国

[20] 吴　超，嵌入式技术在 CCD 成像系统中的应用研究；导师：田建国

[21] 白香港，有机材料的双光子吸收研究；导师：田建国

[22] 杜海伟，反复网格重分法及其在光束传播中的应用；导师：臧维平

[23] 刘春锋，飞秒激光并行微加工技术研究；导师：李玉栋

[24] 王文娟，光伏非线性诱导的 LiNbO3 晶体的不对称扇形效应研究；导师：张天浩

[25] 王秉慧，光折变表面波稳定性研究；导师：张天浩

[26] 徐玉惠，光折变亮表面波及暗表面波的研究；导师：张天浩

[27] 李　丹，Ⅴ/Ⅲ族三元含磷化合物半导体材料生长与性能研究；导师：舒永春

[28] 张　雁，InAs/GaAs 量子点体系中载流子可控输运研究；导师：姚江宏

[29] 刘志伟，基于周期极化掺镁铌酸锂晶体准相位匹配红外光参量振荡研究；导师：姚江宏

[30] 邹昌光，短腔铒镱共掺光纤激光器的研究与制作；导师：宋峰

[31] 蔡　虹，LD 端面抽运铒镱共掺固体激光器模式的理论及实验研究；导师：宋峰

[32] 田　彬，干式激光清洗理论模型与实验研究；导师：宋峰

[33] 张　鑫，简化传播圆理论及自适应热透镜效应固体激光器的研究；导师：宋峰

[34] 宋　杰，ZnS 量子点生物荧光探针的制备与特性研究；导师：赵丽娟

[35] 范　伟，InGaAs/GaAs 量子阱光致发光谱研究；导师：徐晓轩

[36] 孙秀峰，全息体光栅外腔半导体激光器研究；导师：徐晓轩

开放课题/Open Subject

2008 年 9 月，弱光非线性光子学教育部重点实验室召开了学术委员会通讯会议。会议根据学术委员会委员函审结果审批了开放基金，从申请的 10 项课题中评定出 5 项课题予以开放基金资助（资助名单如下）。

项目编号	项目名称	负责人	工作单位	资助额度（万元）	起止时间
OS 08-1	隧穿效应在光折变双中心能级模型中的作用	申岩	哈尔滨工业大学	3	2008.11-2010.9
OS 08-2	基于半导体激光器的宽带宽、超混沌光保密通信研究	夏光琼	西南大学物理科学与技术学院	3	2008.11-2010.9
OS 08-3	基于自相似脉冲放大技术的高能量飞秒脉冲光纤光源研究	张书敏	河北师范大学	2	2008.11-2010.9
OS 08-4	两种光子作用下非晶硫系半导体波导的非线性光学效应研究	邹林儿	南昌大学	2	2008.11-2010.9
OS 08-5	表面等离子激元在表面结构的调制下的相互作用机制和在亚波长光学中的应用	雷军	天津工程师范学院	2	2008.11-2010.9

Spatial Frequency Combs and Supercontinuum Generation in One-Dimensional Photonic Lattices

Rong Dong, Christian E. Rüter, and Detlef Kip
Institute of Physics and Physical Technologies, Clausthal University of Technology, 38678 Clausthal-Zellerfeld, Germany

Ofer Manela and Mordechai Segev
Department of Physics, Solid State Institute, Technion, Haifa 32000, Israel

Chengliang Yang and Jingjun Xu
Key Laboratory of Weak-Light Nonlinear Photonics, Nankai University, Tianjin 300457, People's Republic of China
(Received 4 June 2008; revised manuscript received 25 August 2008; published 30 October 2008)

We experimentally demonstrate the formation of spatial supercontinuum and of spatial frequency combs in nonlinear photonic lattices. This process results from multiple four-wave mixing initiated by launching two Floquet-Bloch modes into a one-dimensional lattice. The dynamics of the waves is sensitively dependent on the transverse momentum difference between the two initial modes: when this momentum difference is commensurable with the lattice momentum the waves evolve into a frequency comb, whereas when it is incommensurable the waves evolve into a supercontinuum of spatial frequencies.

DOI: 10.1103/PhysRevLett.101.183903 PACS numbers: 42.25.Fx, 42.65.Tg, 42.65.Wi, 42.82.Et

The past few decades have witnessed growing interest in wave propagation in nonlinear media having a periodically modulated potential [1], starting with the pioneering work of Fermi, Pasta, and Ulam on wave motion in periodic particle-chains with nonlinear coupling [2]. The interplay between nonlinearity and transport properties in a periodic structure enables nonlinear lattices to exhibit intriguing properties such as lattice modulation instability [3–5], lattice solitons [5–7], and interactions among such solitons [8,9] and among Bloch waves [10], all having no analogue in homogeneous media. Specifically in the optical domain, arrays of evanescently coupled channel waveguides are a prominent example of such nonlinear lattices. These arrays consist of equally spaced identical waveguide elements, displaying all inherent properties of a photonic crystal structure, such as Brillouin zones (BZ), forbidden and allowed bands, and so on. Nonlinear waveguide arrays were realized in different materials including semiconductors [11–13], quadratic media [14], photorefractive crystals [15,16], liquid crystals [17], etc. They provide an excellent platform where nonlinear wave propagation can be directly observed and investigated experimentally [3–17].

In another domain of nonlinear waves in periodic structures-photonic crystal fibers (PCFs)-another effect was demonstrated experimentally in 1999: supercontinuum (SC) generation [18], which describes the evolution of a relatively narrow-band ultrashort optical pulse into a broad continuous spectrum [18], typically spanning an optical octave or more. This phenomenon results from the collective action of the whole set of nonlinear optical effects, such as four-wave mixing (FWM), self- and cross-phase modulation, and stimulated Raman scattering, often accompanied by soliton formation as well as modulation instability [19,20]. The SC generation phenomenon was actually first observed in 1970 [21] in bulk glass. The unusual chromatic dispersion characteristics of PCFs [22] facilitate a strong nonlinear interaction over a significant length of the fiber.

Unlike the extensive studies on temporal SC in PCFs, the dynamics of spatial SC remained unexplored until recently, when the idea of generating spatial SC and frequency combs (FC) in nonlinear photonic lattices were proposed [23]. The process starts with two Floquet-Bloch (FB) modes [with quasimomenta (QM) $k_{x1,2}$] which interact with one another via FWM. The interaction couples power to new FB modes, spreading to more and more modes which are evenly spaced in momentum space. After sufficiently long propagation distances, the power distribution among the FB modes becomes a comb or a SC structure, depending sensitively on whether or not the momentum difference between the two initial modes is commensurable (or not) to the lattice momentum. This dynamics applies to both focusing and defocusing nonlinearities. Here we demonstrate these effects experimentally: the generation of spatial SC and of spatial FC in nonlinear photonic lattices.

Consider a one-dimensional (1D) nonlinear waveguide array, which is periodically modulated in the transverse direction x, but is invariant along the propagation direction z. When the nonlinear action is not too large, the linear FB modes still form a base for describing wave propagation in the lattice; however they couple power to one another (coupled-mode regime). Following Bloch's theorem, the superposition of FB modes (for simplicity, we restrict the sum to the first band) can be written as $\sum_k A_k(z)U_k(x) \times \exp(i\beta_k z)$, where k is the QM and β_k is the propagation

constant of the mode. Here $U_k(x) = u_k(x)\exp(ikx)$, and $u_k(x+\Lambda) = u_k(x)$ are periodic functions with (lattice) period Λ. By solving the nonlinear Schrödinger equation, the coupled-mode equations for the amplitudes $A_k(z)$ are obtained [23]:

$$i\frac{dA_{k_4}}{dz} \pm \sum_{k_1k_2k_3} C_{k_1k_2k_3k_4} A_{k_1}(z) A_{k_2}(z) A^*_{k_3}(z) \exp(i\Delta\beta z) = 0. \tag{1}$$

Here $\Delta\beta = \beta_1 + \beta_2 - \beta_3 - \beta_4$ is the longitudinal phase mismatch, and the plus/minus sign corresponds to the sign of the nonlinearity. Because of the symmetry properties of FB modes, the tensor $C_{k_1k_2k_3k_4}$ can be described as

$$C_{k_1k_2k_3k_4} = N\int_0^\Lambda u_{k_1}(x) u_{k_2}(x) u^*_{k_3}(x) u^*_{k_4}(x) \exp(i\Delta k x) dx. \tag{2}$$

Here N is the number of lattice sites, $G = 2\pi/\Lambda$ is the lattice momentum (width of the BZ), and $\Delta k = k_{x1} + k_{x2} - k_{x3} - k_{x4} = nG$ (with $n = 0, 1, 2, \ldots, C_{k_1k_2k_3k_4} = 0$ when Δk does not satisfy this relation). When the two FB modes are initially excited at $z = 0$, and assuming a sufficient long distance of propagation, a cascaded excitation of modes is triggered. Modes with QM $k_{x1} - n\Delta k_{12}$ and $k_{x2} + n\Delta k_{12}$ ($n = 1, 2, \ldots, \Delta k_{12} = k_{x2} - k_{x1}$) are excited by FWM interactions of the newly generated FB modes with the modes that have excited them. This scenario goes on and on, and new FB modes are sequentially generated, until these modes reach the edge of the first BZ. The evolution from that point and on depends on the commensurability of Δk_{12} and the lattice momentum G.

If the momentum difference between the two initial FB modes, Δk_{12}, is commensurable with the width of the BZ (i.e., $\Delta k_{12} = \alpha G$ with a rational $\alpha = m/l$, m and l being coprime integers), then the nonlinear interaction leads to the appearance of a comb of FB modes, consisting of only l modes in each band. For example, see Fig. 1, for which $m = 1$, $l = 5$, $\alpha = 1/5$. On the other hand, if Δk_{12} is incommensurable with G, the nonlinear interaction excites an infinitely dense set of modes (Fig. 2, for which $\alpha \approx 1/8.6$ is irrational, to within a reasonable experimental accuracy). The explanation of both phenomena has to do with the fact that the lattice can contribute an integer quantum of lattice momentum G to the nonlinear interaction. When a newly generated FB mode is close to the edge of the BZ and it interacts with another mode, subtracting (or adding) lattice momentum folds the interaction outcome back into the first BZ. In the commensurable case, this folding always falls onto an already excited FB mode, thus keeping the number of populated modes a finite discrete set (a comb). On the other hand, in the incommensurable case [Fig. 2], folding maps onto new modes, until eventually all FB modes of a particular band are populated [24]. This is the case of SC generation or equipartition: redistribution of energy between the linear modes of a periodic system as a result of nonlinearity.

Experimentally, we investigate the formation of spatial supercontinuum and frequency combs in a 1D nonlinear lattice fabricated in lithium niobate ($LiNbO_3$). Our 1D waveguide array is fabricated by in-diffusion of Ti on a Fe-doped $LiNbO_3$ wafer, exhibiting a photovoltaic self-defocusing nonlinearity. The array consists of approximately 250 stripes with a width of 6 μm and a grating period $\Lambda = 10$ μm, and the ferroelectric axis points along the x direction. The band spectrum consists of three guided bands, which are separated by gaps. The experimental setup for the generation of spatial supercontinuum and frequency combs is sketched in Fig. 3. We use a continuous wave $\lambda = 532$ nm laser beam (Verdi V2), polarized extraordinarily to utilize the largest electro-optic coefficient r_{33} of the $LiNbO_3$ crystal. The beam is first expanded to a diameter of 30 mm (''plane wave''). Using an aperture of 2 mm diameter, we select the central part (having a constant intensity) to excite ~200 channels of the array. To excite the proper FB modes, the wave is split into two beams of equal power, which are subsequently recombined at a controllable angle. We then use a prism pair (made of high-index Rutile) to couple the two beams simultaneously into, and out of, the waveguide array. Making use of the prism coupling method [25], we selectively excite any desired FB mode (or combinations of several modes) in the array by proper adjustment of the incidence angle. The intensity of the light leaving the in-coupling prism is measured by a photodiode (PD), which allows for exact adjustment of the transverse phase matching condition for excitation of a particular FB mode [26]. The light coupled out by the second prism is recorded by a CCD camera,

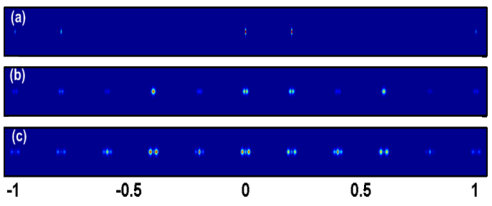

FIG. 1 (color online). Calculated evolution of the field Fourier power spectrum when two modes are launched into the array with QM difference $\Delta k_{12} = G/5$ (commensurate case). Input beam (a), and after 3 mm (b) and 6 mm (c) of propagation. Here the distance of 6 mm is related to the experimental situation.

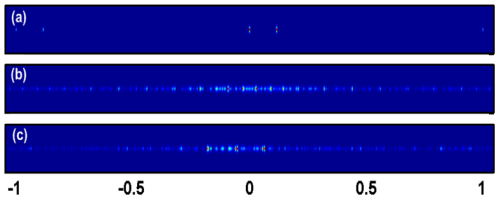

FIG. 2 (color online). Calculated evolution of the field Fourier power spectrum when two modes are launched into the array with QM difference $\Delta k_{12} \approx G/8.6$ (incommensurate case). Input beam (a), and after 3 mm (b), and 6 mm (c) of propagation.

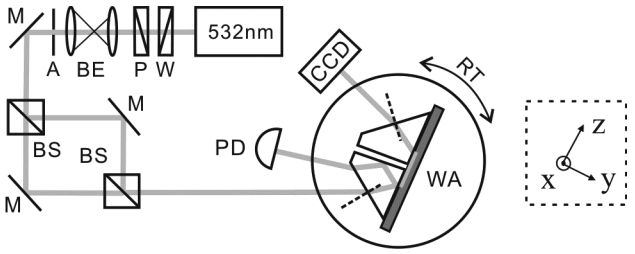

FIG. 3. Schematic experimental setup. W, $\lambda/2$ plate; P, polarizer; BE, beam expander; A, aperture; M's, mirrors; BS's, beam splitters; PD, photodiode; CCD, CCD camera; WA, waveguide array; RT, rotary stage.

which directly yields the Fourier power spectrum inside the array.

In our experiment, we adjust the two input beams to excite simultaneously two different FB modes of the first band, having different wave vectors k_1 and k_2, with $k_2 - k_1 \approx k_{x2} - k_{x1} = \Delta k_{12}$ [see Fig. 4(a)]. The angles between the directions of the input beams and the propagation direction (z direction) in the array determine the transverse wave vectors, thereby determining the Bloch momenta of the excited modes. As such, we can readily adjust the Bloch momentum difference of the excited modes by superimposing the two input beams at the prism base with a small angle difference in the xz plane. In all measurements, one beam (marked as B2) is launched to excite a mode with Bloch momentum $k_{x2} = 0$. The other beam (marked as B1) is adjusted to excite a mode with a QM difference Δk_{12} relative to k_{x2}. Here Δk_{12} can be chosen to

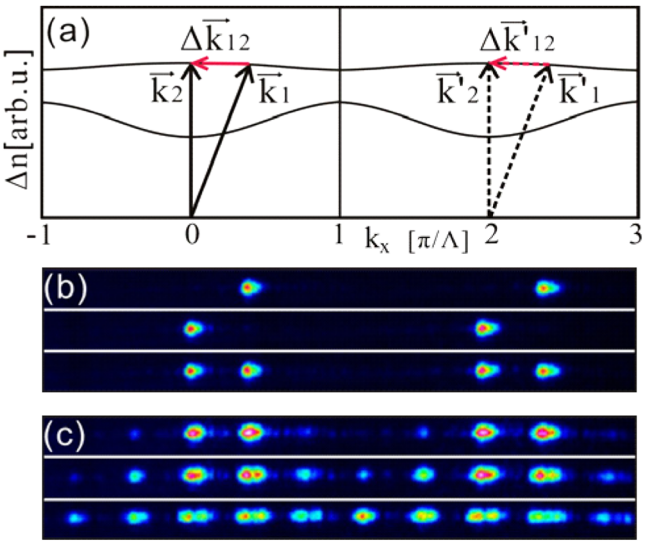

FIG. 4 (color online). Formation of spatial FC in the commensurate case with $\Delta k_{12} = G/5$. (a) Schematic band structure and excited modes. Here $\Delta n = n_{\text{eff}} - n_{\text{sub}}$ represents the effective refractive index of the FB modes; (b) output linear Fourier spectra when B1 (top), B2 (middle), and both B1 and B2 (bottom) are excited; (c) nonlinear evolution of Fourier output spectra after $t = 0.5$, 1.5, and 5 min (from top to bottom).

be either incommensurable or commensurable with the width G of the BZ.

In the first experiment, we investigate the formation of a comb of spatial frequencies. For this commensurate case, the momentum difference is adjusted to $\Delta k_{12} = G/5$. In Fig. 4, we image the output Fourier spectra in two full BZ's, to provide a better perspective of the fashion in which evenly-spaced FB modes are sequentially excited, and overlap at the border between two neighboring BZ's. Figure 4(b) depicts the output Fourier spectra, under linear conditions, when B1 and B2 are excited, either simultaneously or individually. Here the propagation distance is 6 mm and the input optical power is rather low (25 nW per channel), thus avoiding any build-up of nonlinear index changes in the array. As clearly shown in Fig. 4(c), when the optical input power is increased to 0.9 μW per channel, the increasing nonlinearity triggers the formation of a comb of spatial frequencies. Beginning with the two initially excited modes, the spectrum eventually develops into a comb containing 5 FB modes in the first BZ, in agreement with the theory about the anticipated number of modes in each band [23].

Next, we change the setup to observe spatial SC formation. For this the angle between the two input waves is now chosen to be incommensurable with the lattice momentum; here the relation between those is approximately $\Delta k_{12} = G/8.24$ [see Fig. 5(a)]. All other parameters (propagation length, input powers) are the same as before. In Fig. 5(b) the linear Fourier spectra of excited modes are given. Again, we do not observe any energy exchange between the two FB modes under such linear conditions. However, for increased input power, the system becomes highly nonlinear, giving rise to coupling between FB modes and to energy spreading. This result is obvious in Fig. 5(c), which depicts the output power spectrum as the nonlinear interaction builds up in time, becoming stronger and stronger. After switching on the input light at time $t = 0$, a cascaded excitation of FB modes starts, which, at the beginning, is dominated by appearance of additional side bands separated by QM $\pm\Delta k_{12}$ relative to k_{x1} and k_{x2}. With increasing time, also (initially weak) scattered waves start to increase in power and interact via FWM with other FB modes. Finally, after $t = 20$ minutes (this rather large time constant is related to the low mobility of our samples: low charge mobility yields large photovoltaic fields, hence all efficient photovoltaic materials have low mobility), a broad spectrum of FB modes covering almost the full BZ has developed.

The results presented in Figs. 4 and 5 nicely agree with the main predictions outlined in [23]. However, our experiments also reveal new interesting additional effects. Observing Fig. 4 carefully reveals that most of the Fourier components in the comb exhibit a double-peak structure: almost every intensity peak in Fourier space is split in two. Studying this phenomenon numerically (for example by varying the number of excited channels, i.e., changing the width of the super-Gaussian beam we use as

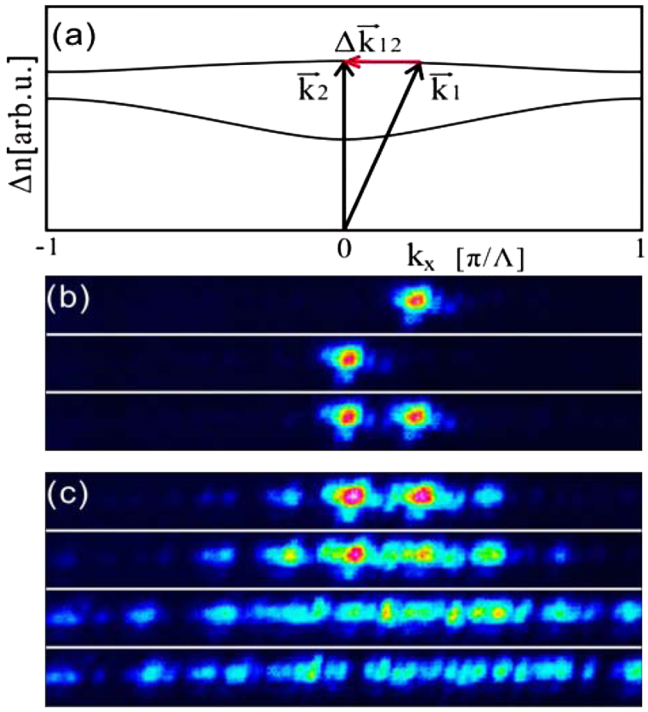

FIG. 5 (color online). Generation of SC in the incommensurate case with $\Delta k_{12} \approx G/8.24$. (a) Schematic band structure and the two FB modes; (b) output linear Fourier spectra when B1 (top), B2 (middle), and both B1 and B2 (bottom) are excited; (c) nonlinear evolution of Fourier output spectra. Photographs (from top to bottom) are taken after $t = 0.5$, 1.5, 5, and 20 min, respectively.

the launch beam) shows that the double-peak effect results from the fact that any finite beam has finite width in Fourier space, and the plane waves comprising each Fourier-peak interact with another through FWM. This phenomenon occurs also in a homogenous system (and is related to holographic scattering [27]). However, in a periodic structure the dispersion inside the band is weaker, and hence the phase matching is better; thus, the resulting peak-splitting is more apparent. In addition, we find that, if, in the simulation, a weak additional wave (of the same wavelength as B1 and B2, but with optical power of only $\sim 1\%$ of them) is launched together with the two input waves into the lattice, this weak wave considerably accelerates the frequency comb or SC generation processes, although naturally it has no apparent effect on the (very dense, almost continuous) spectrum. In the experiment [see, e.g., Fig. 5(b)], although we illuminate our sample only by two plane waves, we always observe such very weak scattered waves adjacent to the two fundamental FB modes. The origin of these waves is attributed to multiple reflections in the Mach-Zehnder interferometer and the coupling prism, or, in the nonlinear case, additional waves formed by holographic scattering inside the array [27].

In summary, we have demonstrated experimentally the generation of spatial FC and of spatial SC resulting from cascaded FWM interactions in 1D photonic lattices. These phenomena display a sensitive dependence on the difference of the FB momentum between the two initially-excited modes and the lattice momentum. We find that an additional weak wave accelerates both processes. We emphasize that both phenomena are universal, and apply to all nonlinear periodic structures in which waves propagate. In this vein, both SC and FC generation should be observable in Bose-Einstein condensates (BEC) in optical lattices, with both attractive and repulsive interactions.

We acknowledge financial support by the Deutsche Forschungsgemeinschaft (KI482/10-1), the German Federal Ministry of Education and Research (CHN 07/040), the Ministry of Science and Technology of P. R. China (2005DFA10170), GIF (grant 949-8.14/2007), and DIP (grant E6.1).

[1] D. N. Christodoulides, F. Lederer, and Y. Silberberg, Nature (London) **424**, 817 (2003).
[2] E. Fermi, J. Pasta, and S. Ulam, Los Alamos Report No. LA-1940 (1955).
[3] J. Meier *et al.*, Phys. Rev. Lett. **92**, 163902 (2004).
[4] D. Kip *et al.*, Science **290**, 495 (2000).
[5] D. N. Christodoulides and R. I. Joseph, Opt. Lett. **13**, 794 (1988).
[6] H. S. Eisenberg *et al.*, Phys. Rev. Lett. **81**, 3383 (1998).
[7] J. W. Fleischer *et al.*, Nature (London) **422**, 147 (2003).
[8] J. Meier *et al.*, Phys. Rev. Lett. **93**, 093903 (2004).
[9] M. Stepić *et al.*, Phys. Rev. E **74**, 046614 (2006).
[10] G. Bartal, O. Manela, and M. Segev, Phys. Rev. Lett. **97**, 073906 (2006).
[11] R. Morandotti *et al.*, Phys. Rev. Lett. **86**, 3296 (2001).
[12] H. S. Eisenberg *et al.*, Phys. Rev. Lett. **85**, 1863 (2000).
[13] P. Millar *et al.*, J. Opt. Soc. Am. B **14**, 3224 (1997).
[14] R. Iwanow *et al.*, Opto-Electron. Rev. **13**, 113 (2005).
[15] J. W. Fleischer *et al.*, Phys. Rev. Lett. **90**, 023902 (2003).
[16] F. Chen *et al.*, Opt. Express **13**, 4314 (2005).
[17] A. Fratalocchi *et al.*, Opt. Express **13**, 1808 (2005).
[18] J. K. Ranka, R. S. Windeler, and A. J. Stentz, Opt. Lett. **25**, 25 (2000).
[19] J. Herrmann *et al.*, Phys. Rev. Lett. **88**, 173901 (2002).
[20] A. V. Grobach and D. V. Skryabin, Nat. Photon. **1**, 653 (2007).
[21] R. R. Alfano and S. L. Shapiro, Phys. Rev. Lett. **24**, 584 (1970).
[22] J. M. Dudley, G. Genty, and S. Coen, Rev. Mod. Phys. **78**, 1135 (2006).
[23] O. Manela *et al.*, Opt. Lett. **31**, 2320 (2006).
[24] Adding lattice momentum can also lead to population of new bands, however the overlap integral—determining the coupling efficiency—between FB modes of different bands is not very large.
[25] P. K. Tien and R. Ulrich, J. Opt. Soc. Am. **60**, 1325 (1970).
[26] C. E. Rüter, J. Wisniewski, and D. Kip, Opt. Lett. **31**, 2768 (2006).
[27] R. A. Rupp and F. W. Drees, Appl. Phys. B **39**, 223 (1986).

Review

International Journal of Modern Physics B
Vol. 22, No. 5 (2008) 447–468

World Scientific
www.worldscientific.com

SLOW AND FAST LIGHTS WITH MOVING AND STATIONARY REFRACTIVE INDEX GRATINGS IN SOLIDS AT ROOM TEMPERATURE

GUOQUAN ZHANG*, FANG BO, FENG GAO, RONG DONG,
YANFEI TU and JINGJUN XU

Photonics Center, College of Physics Science,
Nankai University, Tianjin 300071, China
The Key Laboratory of Weak Light Nonlinear Photonics,
(Nankai University, Tianjin 300457), Ministry of Education, China
**zhanggq@nankai.edu.cn*

Received 5 July 2007

We reviewed the recent progress on slow and fast lights in solids at room temperature based on moving and stationary refractive index gratings. A dispersive photorefractive phase coupling associated with moving gratings results in slow and fast lights. In principle, such phase-coupling-induced slow and fast lights can be observed in any nonlinear wave mixing process with a dispersive phase coupling effect. The slow and fast lights in the stationary gratings are also discussed. One advantage of the stationary gratings is the possibility to engineer the dispersion slope of the grating through designing the grating structure and parameters. As an example, we show that the dispersion slope of the gratings is enhanced significantly by stratifying a series of identical volume index gratings with homogeneous optical buffer layers sandwiched between every two neighboring grating layers. The slow and fast lights, therefore, can be controlled more effectively in such specifically designed grating structures than in the homogeneous gratings. Another advantage is the high transparency of the slow and fast lights with appropriate grating structure and parameters. Issues such as the pulse broadening effect and the pulse distortion are addressed. The slow and fast light techniques have many important potential applications such as optical delay lines and optical buffers.

Keywords: Slow and fast lights; phase coupling; gratings.

1. Introduction

There are at least two different velocities related to the light propagation: one is the phase velocity v_p and the other is the group velocity v_g.[1] Generally speaking, the phase velocity is the velocity at which points of constant phase move through a medium, while the group velocity is defined as the velocity with which a light pulse propagates through a medium. Recent researches[1–16] on light propagation in a dispersive material system show the possibility to slow down or remarkably accelerate the group velocity of light, which has many promising applications such as optical buffers, controllable optical delay/accelerant lines, optical memories, and

devices for quantum information processing. It is also of fundamental interest targeted towards the understanding of physical laws for light pulse propagation, as well as nonlinear optics at the level of a single photon.

Early works on slow and fast lights were generally demonstrated in dispersive amplifying/absorbing material systems.[17–20] Nevertheless, the results were blurred by the pulse deformation due to the amplification or the attenuation of light pulses during propagation. Recently, extremely slow light with a group velocity $\sim$17 ms^{-1} was achieved in an ultracold gas of sodium atoms based on the electromagnetically induced transparency (EIT)[21] effect by Hau's group at Harvard University,[2] while fast light with negligible distortion was observed by Wang *et al.*[8] by use of a pair of Raman gain feature to induce transparency and a large negative refractive index dispersion. It is worthy to note that no signal propagates at a velocity faster than the speed of light in vacuum. For many important potential applications, slow and fast lights in solids are preferred. Various effects such as the EIT,[6,7] coherent population oscillations,[10,22] photorefractive effect,[11,12] stimulated Brillouin scattering and stimulated Ramam scattering in the optical fibers,[13,14] and the resonant effect in photonic crystal waveguides[15] were proposed to generate slow and fast lights in solids.

The photorefractive effect was discovered in lithium niobate ($LiNbO_3$) and lithium tantalate ($LiTaO_3$) by Ashkin *et al.* in 1966.[23] When a spatially inhomogeneous light pattern illuminates an electro–optic material, charge carriers (electrons or holes) are photo-excited from the donors (defects or impurities) to the conduction band or the valence band. These photo-excited electrons or holes migrate in the conduction or the valence band to other places due to diffusion, drift under an electric field or the photovoltaic effect, where they are re-trapped on the acceptors in the photorefractive materials. The photo–excitation, transportation and recombination of charge carriers repeat until a dynamic equilibrium is reached. In this way, the charges are redistributed in the materials, and a spatially inhomogeneous charge distribution is generated, which results in a light-induced space charge field. A spatially inhomogeneous refractive index distribution will be induced through the electro–optic effect of the materials, and this will reversibly influence the propagation behaviors of lights that induce the refractive index change of the photorefractive materials.

The photorefractive effect is a versatile nonlinear optical effect,[24–26] and is effective in photorefractive materials even at very low light intensities. It is inherently a highly dispersive process because it takes time to redistribute the photo–excited charge carriers among different donors and acceptors. In this paper, we will mainly discuss the dispersive properties of the photorefractive wave–mixing process, and special attention is paid to the dispersive photorefractive phase coupling effect and its application to the generation of slow and fast lights. In addition, slow and fast lights in stationary gratings will also be discussed.

The structure of this paper is as follows. We first discussed theoretically the dispersive phase coupling in a nondegenerate photorefractive beam coupling process

in Sec. 2. Slow and fast lights based on the dispersive phase coupling through a moving grating technique are presented in Sec. 3. In Sec. 4, we address slow and fast lights in specially designed stationary grating structures. And finally in Sec. 5, we discussed the pulse broadening effect in slow and fast lights, which is very important in view of practical applications.

2. Dispersive Photorefractive Phase Coupling

In a nondegenerate two-beam coupling process,[27–33] a weak signal beam of an angular frequency ω_s interferes with a strong pump beam of an angular frequency ω_p in a photorefractive material. The induced refractive index grating moves along the grating vector but with a delayed phase-shift with respect to the interference pattern of two coupling beams. Under the small modulation depth approximation, the associated light-induced space charge field E_{sc} is written as[34,35]

$$E_{sc} = -\frac{E_0 - iE_D}{\left(1 + \frac{E_D}{E_q} + i\frac{E_0}{E_q}\right) - \Omega\tau\left(\frac{E_0}{E_q} - i\frac{\tau_{di}}{\tau} - i\frac{E_D}{E_q}\right)}, \tag{1}$$

where $\Omega = \omega_s - \omega_p$ is the angular frequency difference between two coupling beams. E_0, $E_D = ek_BT/q$ and $E_q = eN_A(N_D - N_A)/(qN_D\epsilon\epsilon_0)$ are the externally applied electric field along the grating vector, the diffusion field and the limiting space charge field, respectively. $q = 2\pi/\Lambda$ is the grating vector and Λ is the grating spacing. N_D and N_A are the densities of the total dopants and the non–movable compensation charge that maintains the charge neutrality of the photorefractive materials in the dark, respectively. τ equals to $(\beta + sI_0 + \gamma n_0)^{-1}$, and $\tau_{di} = \epsilon\epsilon_0/e\mu n_0$ is the dielectric relaxation time. I_0, n_0, β, s, γ, e, k_B, T and μ are the total incident intensity, the electron concentration in the conduction band, the thermal excitation rate, the absorption cross section, the recombination coefficient, the magnitude of elementary charge on electrons, the Boltzmann constant, the absolute temperature of the photorefractive materials and the mobility of conduction band electrons in the photorefractive materials, respectively. Note that the photovoltaic effect is not considered here, and electrons are supposed to be the dominant charge carriers.

The intensities and phases of the two beams are coupled with each other through the light–induced refractive index grating. Therefore, one may modify/control the intensity and the phase of the signal beam through the beam coupling process. The variances of the intensity $I_s(r)$ and the phase $\Phi_s(r)$ of the signal beam satisfy the following set of differential equations[24,25]

$$\frac{\partial I_s(r)}{\partial r} = \Gamma_{\text{in}}\frac{I_s(r)I_p(r)}{I_s(r) + I_p(r)} - \alpha I_s(r), \tag{2}$$

$$\frac{\partial \Phi_s(r)}{\partial r} = \Gamma_{\text{ph}}\frac{I_p(r)}{I_s(r) + I_p(r)}, \tag{3}$$

where Γ_{in} and Γ_{ph} are the intensity coupling coefficient

$$\Gamma_{\text{in}} = \frac{2\pi n_b^3 r_{\text{eff}}}{\lambda}\text{Im}(E_{sc}) \tag{4}$$

and the phase coupling coefficient

$$\Gamma_{\rm ph} = \frac{\pi n_b^3 r_{\rm eff}}{\lambda} {\rm Re}(E_{sc})\,, \tag{5}$$

respectively, n_b is the background refractive index of the photorefractive material, $r_{\rm eff}$ is the effective electro–optic coefficient, λ is the operating wavelength, I_p is the pump beam intensity, α is the absorption coefficient of the photorefractive material, and ${\rm Im}(E_{sc})$ and ${\rm Re}(E_{sc})$ represent the imaginary and the real components of the complex space charge field.

It can be demonstrated that the wave coupling processes in photorefractive materials are highly dispersive. Figure 1(a) shows the typical dispersion curves for the phase coupling coefficient $\Gamma_{\rm ph}$ (solid curve) and the slope of the phase coupling coefficient $\partial\Gamma_{\rm ph}/\partial\Omega$ with respect to Ω (dashed curve) for a bismuth silicon oxide ($Bi_{12}SiO_{20}$) crystal under experimental conditions $\lambda = 514.5$ nm, $T = 300$ K, $I_0 = 10^4$ Wm^{-2}, $E_0 = 10^6$ Vm^{-1} and $\Lambda = 30$ μm. The typical material parameters for a $Bi_{12}SiO_{20}$ crystal are shown in Table 1. It is seen that the phase coupling

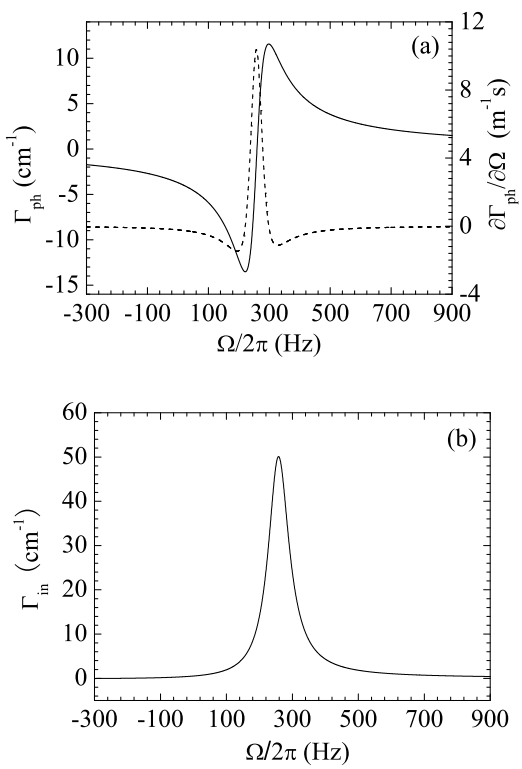

Fig. 1. (a) Typical dispersion curves of $\Gamma_{\rm ph}$ (solid curve) and $\partial\Gamma_{\rm ph}/\partial\Omega$ (dashed curve) and (b): typical dispersion curve of the intensity coupling coefficient $\Gamma_{\rm in}$, for a $Bi_{12}SiO_{20}$ crystal, respectively. The material parameters used to calculate the curves are listed in Table 1, other parameters are $\lambda = 514.5$ nm, $T = 300$ K, $I_0 = 10^4$ Wm^{-2}, $E_0 = 10^6$ Vm^{-1} and $\Lambda = 30$ μm, respectively.

Table 1. Material parameters for a typical photorefractive $Bi_{12}SiO_{20}$ crystal at 514.5 nm. From Ref. 35.

N_A (m^{-3})	N_D (m^{-3})	ϵ –	n_b –	r_{eff} (pm V^{-1})	μ (m^2 V^{-1} s^{-1})	s (m^2 J^{-1})	γ (m^3 s^{-1})	β (s^{-1})
10^{22}	10^{25}	56	2.62	3.4	10^{-5}	1.06×10^{-5}	1.65×10^{-17}	0

coefficient Γ_{ph} varies rapidly as a function of Ω. A steep positive slope ($\sim$10 m^{-1} s) with respect to Ω appears within a narrow frequency window at the middle part of the curves in Fig. 1(a), while the slope $\partial\Gamma_{\text{ph}}/\partial\Omega$ is found to be negative at the two wings of the curve. A typical dispersion curve for the intensity coupling coefficient Γ_{in} is also shown in Fig. 1(b). These results clearly illustrate the highly dispersive property of the photorefractive beam coupling process. Physically, such dispersive property originates from the slow response rate inherent in the photorefractive process, because the formation of the space charge field in photorefractive materials involves the transport and redistribution of charge carriers among different donors and acceptors, which may take quite a long time. Therefore, the strength and the relative phase (with respect to the interference intensity pattern) of the light-induced refractive index grating strongly depend on the angular frequency difference Ω.

In the following section, we will show that such a dispersive beam–coupling process can be used to generate slow and fast lights in the photorefractive materials.

3. Control on Group Velocity of Light through Dispersive Phase Coupling

Equations (2) and (3) can be solved under the pump-undepleted approximation, and one obtains

$$I_s(r) = I_s(0)\exp((\Gamma_{\text{in}} - \alpha)r)\,, \tag{6}$$

$$\Phi_s(r) - \Phi_s(0) = \Gamma_{\text{ph}} r\,. \tag{7}$$

Where $I_s(0)$ and $\Phi_s(0)$ are the initial intensity and phase of the signal beam at the entrance surface of the photorefractive material. It is seen that the signal beam intensity grows exponentially during the propagation, while the phase-coupling-induced phase shift of the signal beam $\Phi_s(r) - \Phi_s(0)$ increases linearly with the propagation distance r. The total phase shift for the signal beam is $\Gamma_{\text{ph}} r + k_s r$ with $k_s = 2\pi n_b/\lambda$ being the wave vector of the signal beam in the photorefractive material.

By differentiating the phase shift per unit distance with respect to the angular frequency ω_s of the signal beam, one obtains the effective group velocity of the signal beam v_g propagating in the photorefractive materials[35]

$$v_g = \frac{c}{n_b + c\frac{\partial(\Gamma_{\text{ph}} + k_s)}{\partial\omega_s}} \approx \frac{c}{n_b + c\frac{\partial\Gamma_{\text{ph}}}{\partial\omega_s}}\,. \tag{8}$$

Where c is the light speed in the vacuum, and the slope $\partial\Gamma_{\rm ph}/\partial\omega_s$ is

$$\frac{\partial\Gamma_{\rm ph}}{\partial\omega_s}=\frac{\partial\Gamma_{\rm ph}}{\partial\Omega}=\frac{n_b^3 r_{\rm eff}}{2c}\frac{E_D B-E_0 A}{A^2+B^2}+\frac{\pi n_b^3 r_{\rm eff}\tau}{\lambda}$$
$$\times\left(\frac{E_D\left(\frac{\tau_{di}}{\tau}+\frac{E_D}{E_q}\right)+\frac{E_0^2}{E_q}}{A^2+B^2}-\frac{2(E_D B-E_0 A)\left[B\left(\frac{\tau_{di}}{\tau}+\frac{E_D}{E_q}\right)-A\frac{E_0}{E_q}\right]}{(A^2+B^2)^2}\right), \quad (9)$$

with the parameters A and B to be

$$A=1+\frac{E_D}{E_q}-\Omega\tau\frac{E_0}{E_q}, \quad (10)$$

and

$$B=\frac{E_0}{E_q}+\Omega\tau\left(\frac{\tau_{di}}{\tau}+\frac{E_D}{E_q}\right), \quad (11)$$

respectively. In general, the refractive index dispersion is negligibly small for photorefractive materials, and it is ignored in arriving at Eqs. (8) and (9). In the case when $n_b \ll c\partial\Gamma_{\rm ph}/\partial\omega_s$ is satisfied, v_g can be further simplified to be

$$v_g\approx\left(\frac{\partial\Gamma_{\rm ph}}{\partial\omega_s}\right)^{-1}. \quad (12)$$

As is shown in Fig. 1(a), the slope $\partial\Gamma_{\rm ph}/\partial\omega_s$ can be either positive or negative, depending on the experimental conditions. Therefore subluminal and superluminal light propagation are possible with a dispersive photorefractive phase coupling. Figure 2 shows the group velocity of light in a typical photorefractive $Bi_{12}SiO_{20}$ crystal in the presence of a dispersive phase coupling process. It can be demonstrated that slow lights with group velocities of the order of $\sim$ cm s^{-1} and fast lights with $v_g \sim -$ms^{-1} are achievable through a dispersive photorefractive two–wave phase coupling.

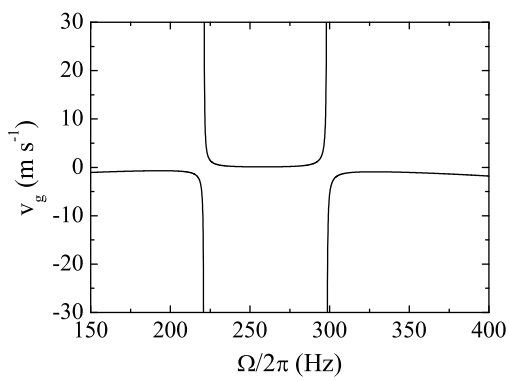

Fig. 2. Slow and fast lights in a photorefractive $Bi_{12}SiO_{20}$ crystal in the presence of a dispersive phase coupling. Simulation parameters: $\Lambda = 30$ μm, $E_0 = 10^6$ Vm^{-1} and $I_0 = 10^4$ Wm^{-2} at 514.5 nm. The material parameters for a $Bi_{12}SiO_{20}$ crystal are listed in Table 1.

The dispersion slope $\partial\Gamma_{\rm ph}/\partial\omega_s$ is related to the response rate and the strength of the photorefractive two-wave coupling, therefore the group velocity of light in photorefractive material can be controlled by adjusting the experimental parameters such as the angular frequency difference Ω, the grating spacing Λ, the incident intensity I_0 and the external field E_0, as well as the material parameters, and it can be tuned to quite a large extent, even from the subluminal to the superluminal, or vice versa, as shown in Fig. 2. Generally speaking, control on the group velocity of light is more effective with a lower intensity I_0 and a higher external field E_0 because the slope $\partial\Gamma_{\rm ph}/\partial\omega_s$ is steeper at these conditions. A more detailed discussion on this topic can be found in Ref. 35.

We note that the spectral bandwidths of the windows for the slow and fast lights are limited. The spectral bandwidth is determined by the response rate of the wave coupling process. A faster response rate corresponds to a broader spectral bandwidth, but at the sacrifice of the steepness of the dispersion slope $\partial\Gamma_{\rm ph}/\partial\Omega_s$. The spectral bandwidth for a slow or fast light is narrower at a low intensity I_0 and a higher external field E_0. The limited spectral bandwidth of the slow or fast light window illustrates the fact that the slow or fast light is observable only when the light pulse duration is comparable to or longer than the response time of the wave coupling process. We will discuss this issue in greater detail in Sec. 5.

Both slow and fast lights induced by the photorefractive phase coupling have been demonstrated experimentally by several research groups.[12,36–41] Figure 3 shows a typical experimental setup scheme to observe slow and fast lights. In the experiments, two techniques are often employed to measure the group velocity of light. One is the intensity modulation technique.[12] In this technique, the signal

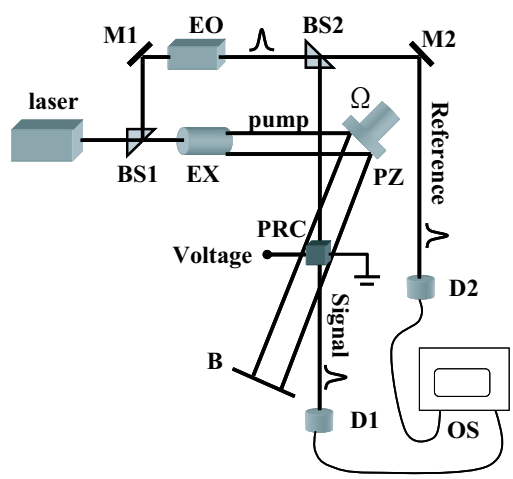

Fig. 3. Experimental setup scheme to measure the group velocity of lights. M1 and M2: mirrors, EO: electro-optic modulator, BS1 and BS2: beam splitter, EX: beam expander, PZ: piezo-mirror which is used to generate an angular frequency shift Ω, PRC: photorefractive crystal, B: Blocker, D1 and D2: photodetector, and OS: oscilloscope, respectively.

beam is modulated sinusoidally and then coupled with a strong cw pump beam in a photorefractive material. It is evident that the sinusoidally modulated signal beam is composed of two components with an angular frequency difference $\delta\omega_s = 2\pi/T$, where T is the periodical time of the sinusoidally modulated signal beam. These two components are respectively coupled with the same pump beam, but of different values of $\Gamma_{\rm ph}$ because the phase coupling coefficient $\Gamma_{\rm ph}$ is highly dispersive in the photorefractive two–beam coupling process [see Fig. 1(a)]. The dispersive phase coupling will result in a phase-delay/phase-advance $\Delta\Phi_s = \delta\Gamma_{\rm ph}L$ [see Eq. (7)] of the transmitted signal beam, where $\delta\Gamma_{\rm ph}$ is the phase coupling coefficient difference between the two components of the signal beam when they are coupled with the pump beam, and L is the propagation distance of the signal beam in the photorefractive material. Therefore the group velocity of the signal beam in the photorefractive material in the presence of a dispersive phase coupling is written as $v_g = (\delta\Gamma_{\rm ph}/\delta\omega_s)^{-1} = L/\delta t$. By measuring the time–delay or time–advance δt experienced by the signal beam, one can obtain the group velocity of the signal beam. Another technique is to use a single light pulse as the signal beam.[38–40] In this case, the time–delay or the time-advance δt experienced by the signal pulse with respect to a reference pulse propagating in air can be measured directly, and the group velocity of the light pulse is obtained through the relationship $v_g = L/\delta t$.

3.1. *Slow light*

Slow light was observed in photorefractive materials such as $BaTiO_3$,[11,37,38] $Bi_{12}SiO_{20}$,[12,39] $Sn_2P_2S_6$ and CdTe.[36] The group velocity from $\sim$ m s^{-1} to $\sim$ mm s^{-1} were reported in different photorefractive materials under various experimental conditions. A typical experimental observation of ultraslow light is shown in Fig. 4, where the steady–state temporal traces for the reference beam and the sinusoidally

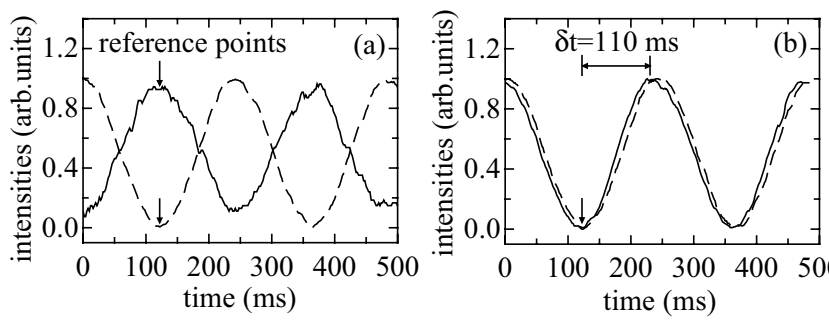

Fig. 4. Steady–state temporal traces of the reference wave (dashed curves) and the transmitted signal wave (solid curves) with the pump beam off (a) and on (b), respectively, during a two-beam coupling in a 5.7-mm $Bi_{12}SiO_{20}$ crystal. A 532-nm solid–state laser was used. The experimental conditions were a pump beam intensity $I_p = 106$ mW cm^{-2}, the pump to the signal intensity ratio $\zeta = 1500$, an external field $E_0 = 8$ kV cm^{-1}, a grating spacing $\Lambda = 21.3$ μm, a periodical time of the signal beam $T = 250$ ms and a frequency–shift of the pump beam $\Omega/2\pi = 50$ Hz, respectively. From Ref. 12.

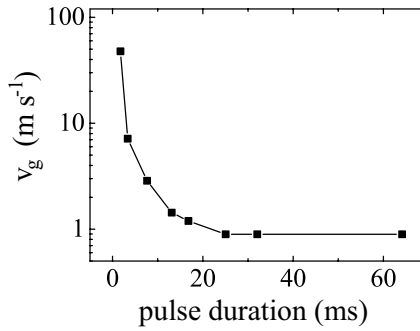

Fig. 5. Group velocity of a single Gaussian pulse v_g as a function of the pulse duration measured in a 5.7-mm $Bi_{12}SiO_{20}$ crystal. The values for I_p, ζ, E_0, Λ and $\Omega/2\pi$ were set at 152 mW cm^{-2}, 1400, 8 kV cm^{-1}, 21.3 μm and 60 Hz, respectively.

modulated signal beam after a $Bi_{12}SiO_{20}$ crystal was recorded. A time–delay of 110 ms was detected for the transmitted signal beam in a 5.7-mm $Bi_{12}SiO_{20}$ crystal, which corresponds to an ultraslow group velocity of $\sim$0.05 m s^{-1}. In addition, the phase-coupling-induced slow light was found to be amplified because of the energy transfer from the pump beam through the intensity coupling effect, which is quite different from the slow lights based on EIT[2] and quantum population oscillation effects.[10,22] We will discuss this issue in greater detail in Sec. 3.4.

It is found that the group velocity of a Gaussian light pulse depends on the pulse duration.[39] The group velocity v_g of a Gaussian pulse was found to be decelerated with the increment of the pulse duration, but finally reaches a minimum value, as shown in Fig. 5. This is because the photorefractive phase coupling is more effective with a longer pulse duration, especially when the pulse duration is much less than the response time of the coupling process, but it finally saturates when the pulse duration is comparable to or much longer than the response time. We also note that the time-delay δt of a single pulse is less than that in the quasi-continuous wave (quasi-cw) case (for example, that measured by the intensity modulation technique), even under similar experimental conditions. This may be due to the fact that the interaction duration between the signal and the pump in the single pulse case is determined entirely by the pulse duration, while the photorefractive phase coupling effect accumulates one pulse after another because of the memory effect of the photorefractive gratings,[26] and is therefore enhanced in the quasi-cw case. In addition, the photorefractive phase coupling is more complicated in the single pulse case than in the quasi-cw case because the frequency components of a single pulse are more complicated than those of a sinusoidal wave in the quasi-cw case.

3.2. *Fast light*

With an appropriate angular frequency difference Ω between the pump and the signal beams, fast light was observed by Bo *et al.*[40,41] in photorefractive $Bi_{12}SiO_{20}$

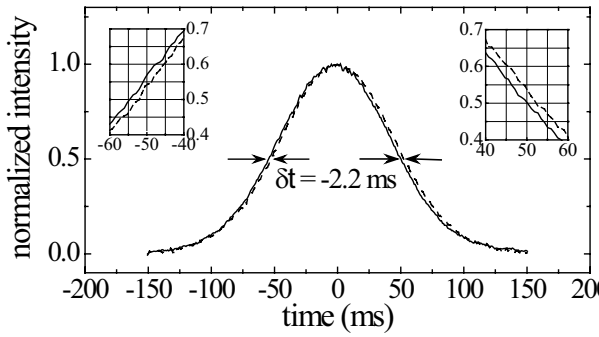

Fig. 6. Temporal traces of fast light in a 5.7-mm photorefractive $Bi_{12}SiO_{20}$ crystal. The dashed and the solid curves were for the reference and the signal pulses, respectively. A 90-ms Gaussian pulse experienced a time–advance of -2.2 ms when a pump beam was on. The pump beam was of 34 mW cm^{-2} at 532 nm and shifted in frequency by $\Omega/2\pi = 2$ Hz. The pump to the signal intensity ratio was 1400. The external field E_0 and the grating spacing Λ were 8 kV cm^{-1} and 21.3 μm, respectively. The insets show the leading and the trailing edges of the signal and the reference pulses. Both the leading and the trailing edges of the pulses were shifted in time by the same amount.

crystals. A negative group velocity of -2.6 m s^{-1} was measured for a 90-ms Gaussian pulse propagating in a 5.7-mm $Bi_{12}SiO_{20}$ crystal in the presence of a pump beam of 34 mW cm^{-2}, as shown in Fig. 6. The transmitted signal pulse was found to be amplified slightly with the pump beam on, as compared with that without the pump beam. This indicates that the fast light is not a result of the energy transfer between the two coupling beams which requires the attenuation of the signal pulse. We should emphasize that the observed fast light with a negative group velocity is not at odds with causality, it is a result of the negative slope of the phase coupling coefficient dispersion and the interference among different frequency components of the light pulse.

Very recently, fast light was also observed by Gao *et al.*[42] in ruby at room temperature. Figure 7 shows the experimental setup scheme to measure the group velocity of light in ruby. A 532-nm laser beam was modulated into Gaussian pulses by an electro–optic modulator with a pulse duration of 40 ms and a modulation depth of 0.66, and then focused into a 10–cm ruby. The peak intensity of the pulse in the front of the ruby was 490 mW. The group velocity in the ruby was obtained by measuring the time delay δt between the transmitted signal pulse and a reference pulse from detectors D1 and D2, respectively. By adjusting the distance d between the lens L1 and the front surface of the ruby, one could observe both the subluminal and the superluminal light propagation at appropriate conditions. In the case when the front surface of the ruby was beyond the focal plane of the lens (i.e., $d > 300$ mm), one observed slow lights. On the other hand, when the front surface of the ruby was within the focal plane of the lens, one could observe fast light propagation, as shown in Fig. 8 where d was set to be 233 mm and a time advance of -1.6 ms was observed.

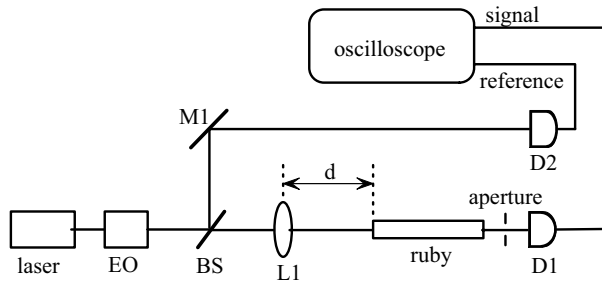

Fig. 7. Experimental setup scheme to measure the group velocity of light in ruby at room temperature. EO: an electro–optic modulator, BS: a beam splitter, L1: a lens with a 300-mm focal length, M1: a mirror, and D1 and D2: detectors. d is the distance between the lens and the front surface of the ruby.

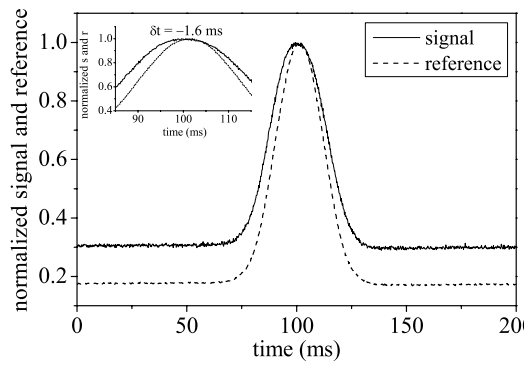

Fig. 8. The normalized temporal traces of the transmitted signal pulse (solid curve) and the reference pulse in the air (dashed curve). The inset shows the temporal traces near the peak of the pulses for a clear view of the time advance.

We believe the observed fast light in the room-temperature ruby is a result of the wave coupling process between different frequency components of the incident pulse. It is known that a Gaussian pulse consists of many frequency components. These frequency components interact with each other in the ruby via nondegenerate wave coupling processes[43] with dispersive phase coupling coefficients of negative or positive dispersion slopes under appropriate conditions.[44] Such nondegenerate wave couplings are usually accompanied by energy transfer between different frequency components. In fact, we did observe the energy transfer from the center to the edge of the beam, which was a good support for the above explanation.

3.3. *Transition between slow and fast lights*

A convenient way to realize transition between slow and fast lights is by tuning the angular frequency difference Ω between the signal and the pump beams. It is evident from Fig. 1 that the slope $\partial\Gamma_{\rm ph}/\partial\omega_s$ is negative first and then becomes positive, but finally goes to negative again when one scans the angular frequency

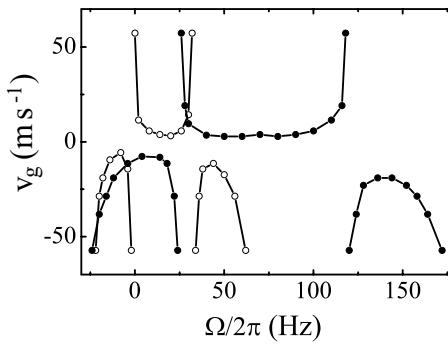

Fig. 9. Transitions between slow and fast lights achieved by scanning the angular frequency difference Ω in a 5.7-mm photorefractive $Bi_{12}SiO_{20}$ crystal. The solid and the empty circles were the results with I_p = 83.0 mW cm^{-2} and I_p = 19.5 mW cm^{-2} at 532 nm, respectively. The values of E_0, I_s, Λ and T for both cases were 8 kV cm^{-1}, 0.1 mW cm^{-2}, 21.3 μm, and 30 ms, respectively. The results were measured by using the intensity modulation technique.

shift Ω of the pump beam with respect to the signal beam. Therefore, it is easy to demonstrate slow and fast lights in the same photorefractive material and thereby the transitions between the slow and the fast lights simply by scanning the angular frequency shift Ω of the pump beam. Bo *et al.*[41] demonstrated experimentally such transitions by scanning the pump frequency shift in a photorefractive $Bi_{12}SiO_{20}$ crystal, as shown in Fig. 9.

The slope $\partial\Gamma_{\rm ph}/\partial\omega_s$ is determined by the response rate and the coupling strength of the photorefractive wave coupling, and is therefore tunable to quite a large extent by adjusting the experimental conditions, so is the group velocity of lights.[35] In addition, the subluminal and the superluminal spectral windows shift when one tunes the pump intensity I_p or the external field E_0, as one can see from Fig. 9. This is because the response rate and the coupling strength of the photorefractive two-beam coupling depend on experimental parameters such as the incident intensity and the external field. Therefore, at a specific angular frequency shift of the pump beam with respect to the signal beam, one might observe transitions between slow and fast lights by tuning the pump intensity or the external field. Figure 10 shows such slow and fast light transitions in photorefractive $Bi_{12}SiO_{20}$ crystals at room temperature by tuning the pump intensity I_p and the external field E_0, respectively.

3.4. *Amplification of slow and fast lights*

Both slow and fast lights induced by the photorefractive phase coupling were observed to be amplified due to the energy transfer from the pump beam through the intensity coupling effect [see Eq. (6) and Fig. 1(b)], while the slow light was found to be amplified more effectively than the fast light.[12,41] Figure 11 shows the measured dispersion curves of $\Gamma_{\rm in}$ in the cw regime and v_g measured using the sinusoidal intensity modulation technique under the same experimental conditions except for

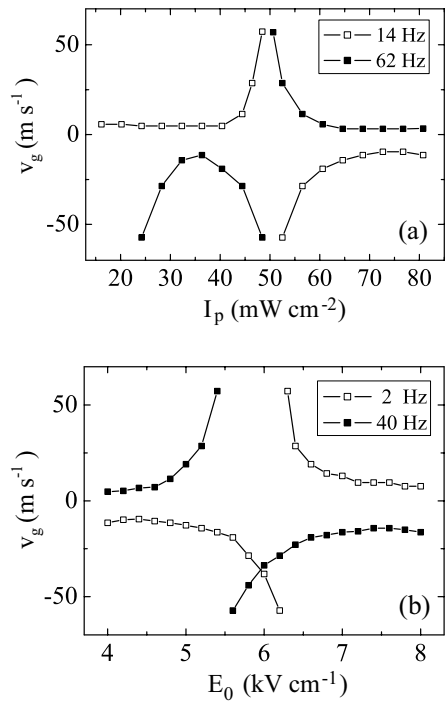

Fig. 10. Transitions between slow and fast lights by tuning the pump intensity I_p or the external field E_0 in a 5.7-mm photorefractive $Bi_{12}SiO_{20}$ crystal. (a) Slow and fast light transitions by tuning the pump intensity I_p at $\Omega/2\pi = 14$ Hz (*empty squares*) and 62 Hz (*solid squares*), respectively. An external field E_0 of 8 kV cm^{-1} was applied cross the crystal. (b) Slow and fast light transitions by tuning the external field E_0 at $\Omega/2\pi = 2$ Hz (*empty squares*) and 40 Hz (*solid squares*), respectively. The pump intensity I_p was set to be 19.5 mW cm^{-2}. Other parameters I_s, Λ and T for both cases were 0.1 mW cm^{-2}, 21.3 μm and 30 ms, respectively. The results were measured by using the intensity modulation technique.

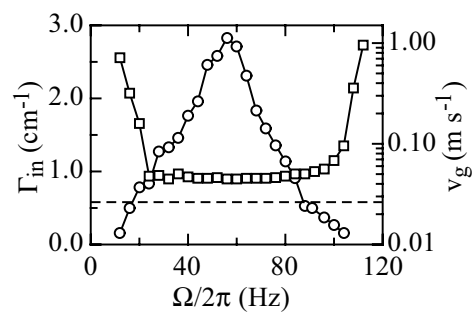

Fig. 11. Dispersion curves for $\Gamma_{\rm in}$ (connected circles) measured in the cw regime and v_g (connected squares) measured by using the sinusoidal intensity modulation technique in a 5.7-mm $Bi_{12}SiO_{20}$ crystal with $I_p = 106$ mW cm^{-2} at 532 nm, $\Lambda = 21.3$ μm and $E_0 = 8$ kV cm^{-1}. The pump to the signal intensity ratio ζ was set to be 3000 and 1500 for the cases of $\Gamma_{\rm in}$ and v_g, respectively. The dashed horizontal line indicates the value of the absorption coefficient α at 532 nm for the $Bi_{12}SiO_{20}$ crystal. From Ref. 12.

a difference in the pump to signal intensity ratio ζ by a factor of 2 because the sinusoidal signal beam has two components with equal intensities. It is clearly shown that the slow light is amplified within the slow light spectral window. The amplification of slow light was also confirmed both theoretically and experimentally by Podivilov *et al.* in a $BaTiO_3$ crystal.[11] One might explain the slow light in photorefractive material as a result of the dynamic amplification of the signal pulse in the wave coupling. In fact, this is not the case. Odoulov *et al.*[36] proved experimentally that it is the strong dispersion of the dynamic photorefractive gratings instead of the intensity amplification that is of primary importance for the slow light. They observed a considerable deceleration of light pulses in crystals such as $Sn_2P_2S_6$ and CdTe with nearly compensated space charge fields due to the electron–hole competition, in which the unidirectional energy transfer effect is negligibly small.

Several inherent advantages are appealing for this technique: (1) the group velocity of light pulses can be controlled to a great extent at room temperature in solids by controlling the phase coupling coefficient dispersion, both slow and fast lights are possible by controlling the sign of $\partial\Gamma_{\mathrm{ph}}/\partial\omega_s$; (2) the slow and fast light pulses can be amplified by use of the energy transfer from the coupling beam; (3) this technique is effective in a wide spectral range, as long as a dispersive phase coupling occurs during a nonlinear wave mixing process. Moreover, slow and fast lights are expected in all nonlinear wave mixing processes with a dispersive phase coupling effect; (4) the experimental requirements are relatively simple, for example, it is not necessary for the light source to be a single frequency laser, and it operates at room temperature.

4. Control on Group Velocity of Light through Stationary Gratings

Slow and fast lights induced by the dispersive phase coupling process are based on the dynamic refractive index gratings in the photorefractive materials. In fact, slow and fast lights can also be generated in stationary refractive index gratings by using its dispersion property of the forbidden bandgap.[45] One advantage of the stationary grating is the possibility to modify its dispersion property through the grating structure design.[46] In the following subsections, we will address the issues on slow and fast lights in uniform stationary gratings, as well as in specifically structured gratings.

4.1. *Fast and slow lights in uniform stationary gratings*

The effective group velocity in a uniform stationary grating (SG) with a grating spacing Λ and a length L is written as[45]

$$v_g = \frac{c}{n_b}\frac{(\Delta k/2)^2 - \kappa^2 \cosh^2 \xi L}{(\Delta k/2)^2 - \kappa^2 \frac{\sinh \xi L}{\xi L}\cosh \xi L}\,, \tag{13}$$

where $\Delta k = 2n_b\omega_s/c - 2\pi/\Lambda$ is the phase mismatch, ξ is equal to $(\kappa^2 - (\Delta k/2)^2)^{1/2}$, and $\kappa = \pi n_1/\lambda$ is the coupling constant, n_1 is the index modulation of the stationary grating. At the center of the forbidden gap where $\Delta k = 0$, the effective group velocity reduces to

$$v_g = \frac{c}{n_b} \frac{\kappa L}{\tanh \kappa L}\,, \tag{14}$$

and one observes fast light. The group velocity is approximated to $\kappa L v_g$ as κL becomes very large. Nevertheless, the light transmission is very small because of the Bragg-reflection effect of the volume index grating. At the immediate vicinity of the band edges where $\xi L = i\pi$ and the transmission is unity, slow light is expected with an effective group velocity

$$v_g = \frac{c}{n_b} \frac{\pi^2}{\kappa^2 L^2 + \pi^2}\,. \tag{15}$$

Lin *et al.*[45] experimentally demonstrated slow and fast lights in a uniform stationary grating. A group index $n_g = c/v_g = 7.5$ was observed in a stationary volume index grating with an index modulation depth $n_1 = 2.1 \times 10^{-5}$ recorded in a 3.5–cm photorefractive $LiNbO_3$:Fe crystal. Gao *et al.*[47] quantitatively studied the relationship between the group velocity of light and the parameters such as the phase mismatch Δk and the diffraction efficiency η of the gratings in $LiNbO_3$ crystals with different dopants (see Fig. 12). The effective group velocity of light was found to be roughly proportional to the diffraction efficiency η of the grating when the grating modulation depth is small and the phase mismatch is fixed. One notes that the group index is quite small in the uniform SGs, although it is expected to increase with a longer grating length L and a larger modulation depth n_1.

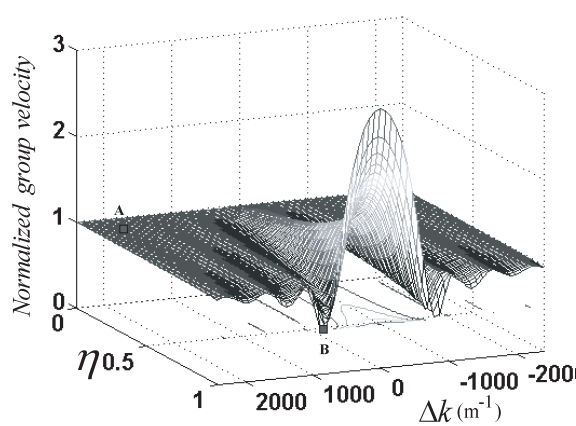

Fig. 12. The dependence of the normalized group velocity of light $v_g/(c/n_b)$ on the diffraction efficiency η and the phase mismatch Δk.

4.2. *Control on group velocity of light through stratified and phase-shifted volume index gratings*

The dispersion property of the gratings can be modified by introducing defect structures into the gratings.[46] We have designed a kind of stratified and phase-shifted volume index grating (SPVIG) in which N discrete thick volume index grating layers of thickness D are interleaved with $N-1$ optically homogeneous buffer layers of thickness d, as shown in Fig. 13. The buffer layers provide the phase-shifts between the neighboring grating layers. For the sake of simplicity, the averaged refractive indices for both the grating layers and the buffer layers are set to be n_0. The refractive index modulation depth for the grating layers is n_1, and the grating wave vector along the x–axis is $q = 2\pi/\Lambda$ with Λ being the grating spacing.

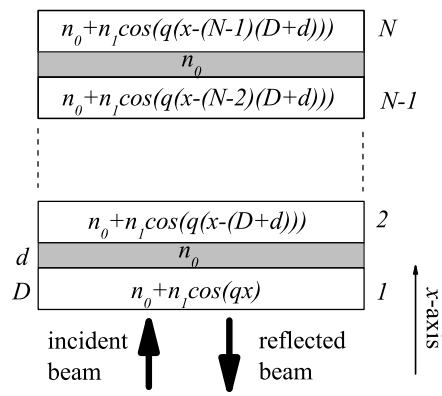

Fig. 13. The structure of the stratified and phase-shifted volume index gratings.

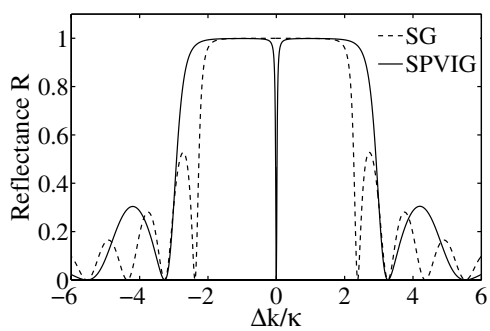

Fig. 14. Reflectance spectra of an uniform SG (dashed curve) and a 2-layer SPVIG (solid curve). The grating parameters for both cases are $\Lambda = 0.5$ μm and $n_1 = 4 \times 10^{-4}$. Other parameters are set to be $D = 3$ mm, $d = 2.25$ μm and $n_0 = 1.55$, respectively. The thickness of the uniform SG is 6 mm for comparison.

4.2.1. *Enhanced dispersion of stratified and phase-shifted volume index gratings*

The reflectance spectra of the SPVIGs have been studied, and strong spectral dispersion has been found in such structures. As compared to the reflectance spectra of the uniform SGs, transparency peaks appear within the stop band of the reflectance spectra of the SPVIGs due to the intervention of the homogeneous buffer layers. As an example, Fig. 14 shows the reflectance spectra for a 2-layer SPVIG ($N = 2$) with $\Lambda = 0.5$ μm, $n_1 = 4 \times 10^{-4}$, $D = 3$ mm, $d = 2.25$ μm and $n_0 = 1.55$, respectively. The reflectance spectra for a 6-mm uniform SG with the same set of grating parameters as those of the 2-layer SPVIG is also shown in Fig. 14 for comparison. A narrow bandwidth transparency peak with nearly 100% transmittance appears at the Bragg-matched wavelength $\lambda_0 = 1.55$ μm in the reflectance spectrum of the 2-layer SPVIG whenever the condition $2k_0 d = (2m + 1)\pi$ is satisfied, where m is an integer and $k_0 = 2\pi n_0/\lambda_0$ is the wave vector at the Bragg-matched wavelength. It can be demonstrated that $N - 1$ transparency peaks will appear within the stop band of the reflectance spectrum of the N-layer SPVIG, and that the positions of the transparency peaks can be controlled by adjusting the phase-shift induced by the buffer layer.[46]

4.2.2. *Enhanced control on group velocity of light in stratified and phase-shifted volume index gratings*

The dispersion of the SPVIG is remarkably enhanced as compared to that of the uniform SG. Therefore, an enhanced control on the group velocity of lights is feasible through the design of the SPVIGs. Figure 15(a) depicts the simulation results of the group velocity v_g and the transmittance T of lights through a 2-layer SPVIG with $n_0 = 1.55$, $D = 1.46$ mm, $d = 0.25$ μm, $\Lambda = 0.5$ μm and $n_1 = 4 \times 10^{-4}$, respectively. For comparison, the group velocity and the transmittance of a uniform SG with $n_0 = 1.55$, a thickness of $2D + d$, $\Lambda = 0.5$ μm and $n_1 = 4 \times 10^{-4}$ are also shown in Fig. 15(b). It is seen that fast light is demonstrated at/near the Bragg-matched wavelength in both cases, while the group velocity in the 2-layer SPVIG case is faster by a factor of ~ 10 as compared to that in the uniform SG case. Moreover, the transmittance of the fast lights in the 2-layer SPVIG case is larger than 80%, whereas that in the uniform SG case is less than 5% due to the Bragg-reflection effect. It is evident that, as compared to the uniform SGs, an enhanced effect on the control of light group velocity with a high transmittance by use of the SPVIGs is demonstrated.

Figure 16 shows the group delay τ_g (defined as $\tau_g = L/v_g$, where L is the total thickness of the SPVIG or the uniform SG) as a function of the thickness D for the 2-layer SPVIGs and the uniform SGs at the Bragg-matched wavelength $\lambda_0 = 1.55$ μm. The parameters for n_0, d, Λ and n_1 are set to be 1.55, 0.25 μm, 0.5 μm and 4×10^{-4}, respectively. The thickness of the uniform SG is $L = 2D + d$. It is seen that the group delay in the uniform SG case increases first but then tends

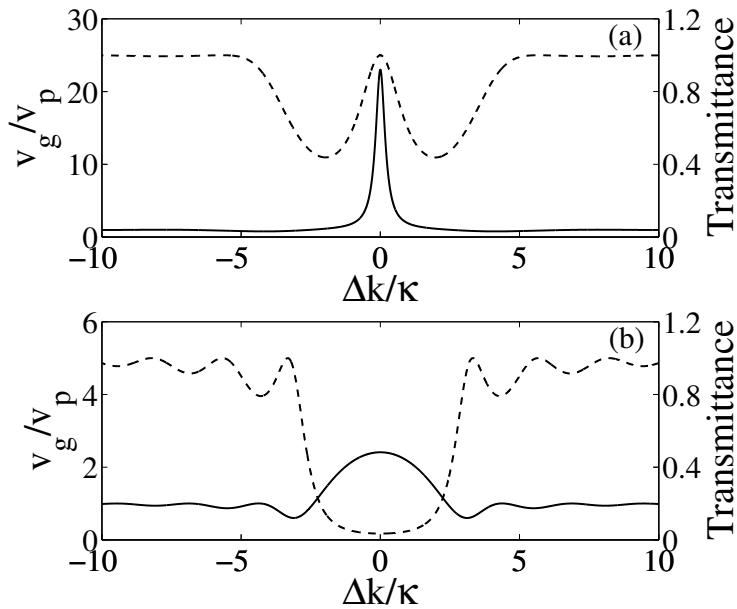

Fig. 15. The normalized group velocity v_g/v_p (solid curves) and the transmittance (dashed curves) of the light incident normally onto a 2-layer SPVIG (a) and an uniform SG (b), respectively. Here $v_p = c/n_0$ is the phase velocity and c is the velocity of light in vacuum.

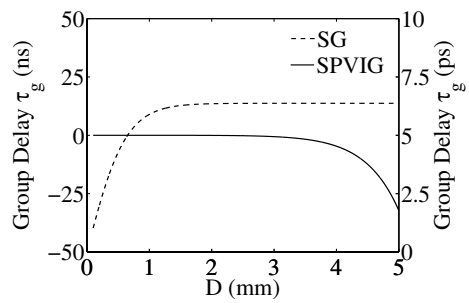

Fig. 16. The group delays τ_g of a 2-layer SPVIG (solid curve) and an uniform SG (dashed curve) versus the variation of the grating thickness D.

to be saturated with the increase of D. The group delay in the 2-layer SPVIG case varies slowly at first, but then becomes negative and decreases rapidly with the increase of D. A negative group delay of ~ -30 ns is possible with $D = 5$ mm. This is because the transparency peak becomes sharper and sharper, therefore, the dispersion slope becomes steeper and steeper with the increment of D in the 2-layer SPVIG case. Note that the time scale for the SPVIG is nano-second while that for the uniform SG is pico-second in Fig. 16. These results clearly illustrate the versatility and the effectiveness of the SPVIG on the control of the group velocity of light through the design of its structure and grating parameters.

5. Pulse Broadening Effect

For practical applications, it is necessary to deccelerate/accelerate pulses while keeping their temporal profile of high fidelity.[16] This is achieved experimentally when the bandwidth of the pulse is within the subluminal or the superluminal spectral windows. For short duration pulses with a broad spectral bandwidth, however, serious temporal profile distortion is observed[6,37,39] because the spectral bandwidth of the light pulse is much broader than that of the subluminal or the superluminal spectral windows (see Fig. 1). In this case, the frequency components of the pulse are not uniformly delayed and amplified or attenuated. Furthermore, the high order dispersion effect will also contribute to the pulse broadening and distortion.[48,49] Such pulse broadening effects will not only degrade the measurement accuracy, but also impede slow and fast lights from practical applications such as an optical buffer.

Several techniques were proposed to alleviate the pulse broadening effect. Odoulov *et al.*[36] delayed Gaussian pulses without severe broadening effect by using pump pulses of identical temporal profile as those of the signal pulses. The pulses were delayed through a degenerate photorefractive two-wave mixing with a negligible intensity coupling effect using electron–hole competition in $Sn_2P_2S_6$ and CdTe crystals. Recently, Deng *et al.*[38] proposed a novel technique to solve the pulse broadening effect and to enlarge the delay-time-bandwidth product of slow lights. The key in the technique is to simultaneously slow down all frequency components of the input pulse by the same amount using inhomogeneous broadening. The input pulse is first split into different spectral channels by use of a dispersive element such as a prism or grating. Each spectral channel is composed of a relatively long subpulse with its temporal duration and its central frequency determined by the inverse spectral resolution and the channel number of the dispersive element, respectively. These spatially separated subpulses are then delayed independently by the same amount of time using bandwidth–matched slow–light array elements, and are finally recombined using another dispersive element to produce the output pulse. In this way, a short pulse can be delayed by an amount of time much larger than the pulse duration without temporal profile distortion and broadening effect. As a proof–of–principle experiment, they tried to slow down a rectangular pulse in a photorefractive $BaTiO_3$:Ce crystal by using multiple pump beams, in which each pump beam was tuned at different incident angle and frequency shift with respect to the central frequency of the rectangular pulse. Here, the photorefractive crystal simultaneously worked as both a dispersive and a slow–light element. The pulse distortion was demonstrated to be alleviated to some extent, depending on the number of pump beams (spectral channels) used.

Since the bandwidth of the frequency window for the slow and fast lights is determined by the response rate of the phase coupling process, a larger response rate corresponds to a broader spectral window of slow and fast lights. One may alleviate the pulse distortion and broadening effect by improving the response rate of the phase coupling process. This could be achieved by increasing the incident

intensity but the slope $\partial\Gamma_{\rm ph}/\partial\omega_s$ becomes less steep, therefore tradeoff between the pulse duration and the group velocity of light pulse should be made. One way to solve this dilemma is to use a photorefractive material with a larger coupling strength and a fast response rate. The photorefractive quantum well is a good candidate for short pulse applications, and it is known to possess a strong coupling strength of $\sim 10^3$ cm^{-1} and a short response time of the order of microseconds, even at the mW cm^{-2} intensity level in the near infrared.[50,51] In such material systems, pulses of microseconds with a group velocity of the order of centimeters per second are expected. However, for practical applications of slow and fast lights, large ratios of the time delay δt to the pulse duration may be necessary.

6. Summary

In summary, we have reviewed the recent progresses on slow and fast lights based on the dispersive properties of both moving and stationary gratings. Slow lights with group velocities as low as $\sim$ mm s^{-1} and fast lights with negative group velocities in the order of $\sim$ m s^{-1} have been observed in photorefractive materials with a dispersive phase coupling based on moving gratings. Several methods have been developed to tune the group velocity of light to a large extent, and even transitions between slow and fast lights can be easily realized. The phase-coupling-induced slow and fast lights can be observed in principle in various nonlinear wave mixing processes as long as there are dispersive phase coupling effects. It has been demonstrated that the dispersion properties of stationary gratings can be engineered by designing the grating structure and parameters, therefore, enhanced control on the group velocity of light can be realized in grating structures such as the stratified and phase-shifted volume index gratings. More importantly, one is able to observe slow and fast lights while still maintaining high transparency through grating design. In addition, in view of practical applications, important issues on slow and fast lights such as the pulse broadening effect are discussed, and methods and techniques to alleviate the pulse broadening effect are reviewed. The slow and fast light techniques have important potential applications such as optical delay line, optical buffer and quantum information processing.

Acknowledgments

This work is financially supported by the National Natural Science Foundation of China (grants 60308005, 60678021 and 10334010), the Program for New Century Excellent Talents in University under grant NCET-04-0234, the Program for Changjiang Scholars and Innovative Research Team in University, the Municipal International Cooperation Program of Tianjin under grant 06YFGHHZ00500, the National Basic Research Program of China under grant 2007CB307002, CNKBRSF under grant 2006CB921703, and the Programme of Introducing Talents of Discipline to Universities.

References

1. P. W. Milonni, *Fast Light, Slow Light and Left-Handed Light* (Institute of Physics Publishing, Bristol and Philadelphia, 2005), pp. 1–179.
2. L. V. Hau, S. E. Harris, Z. Dutton and C. H. Behroozi, *Nature* **397**, 594 (1999).
3. M. M. Kash, V. A. Sautenkov, A. S. Zibrov, L. Hollberg, G. R. Welch, M. D. Lukin, Y. Rostovtsev, E. S. Fry and M. O. Scully, *Phys. Rev. Lett.* **82**, 5229 (1999).
4. C. Liu, Z. Dutton, C. H. Behroozl and L. V. Hau, *Nature* **409**, 490 (2001).
5. D. F. Phillips, A. Fleischhauer, A. Mair, R. L. Walsworth and M. D. Lukin, *Phys. Rev. Lett.* **86**, 783 (2001).
6. A. V. Turukhin, V. S. Sudarshanam, M. S. Shahriar, J. A. Musser, B. S. Ham and P. R. Hemmer, *Phys. Rev. Lett.* **88**, 023602 (2002).
7. J. J. Longdell, E. Fraval, M. J. Sellars and N. B. Manson, *Phys. Rev. Lett.* **95**, 063601 (2005).
8. L. J. Wang, A. Kuzmich and A. Dogariu, *Nature* **406**, 277 (2000).
9. M. D. Stenner, D. J. Gauthier and M. A. Neifeld, *Nature* **425**, 695 (2003).
10. M. S. Bigelow, N. N. Lepeshkin and R. W. Boyd, *Science* **301**, 200 (2003).
11. E. Podivilov, B. Sturman, A. Shumelyuk and S. Odoulov, *Phys. Rev. Lett.* **91**, 083902 (2003).
12. G. Zhang, F. Bo, R. Dong and J. Xu, *Phys. Rev. Lett.* **93**, 133903 (2004).
13. Y. Okawachi, M. S. Bigelow, J. E. Sharping, Z. Zhu, A. Schweinsberg, D. J. Gauthier, R. W. Boyd and A. L. Gaeta, *Phys. Rev. Lett.* **94**, 153902 (2005).
14. D. Dahan and G. Eisenstein, *Opt. Express* **13**, 6234 (2005).
15. Y. A. Vlasov, M. O'Boyle, H. F. Hamann and S. J. McNab, *Nature* **438**, 65 (2005).
16. R. W. Boyd, D. J. Gauthier and A. L. Gaeta, *Opt. Photon. News* **17**(4), 19 (2006).
17. C. G. B. Garrett and D. E. McCumber, *Phys. Rev. A* **1**, 305 (1970).
18. M. D. Crisp, *Phys. Rev. A* **4**, 2104 (1971).
19. S. Chu and S. Wong, *Phys. Rev. Lett.* **48**, 738 (1982).
20. E. L. Bolda, R. Y. Chiao and J. C. Garrison, *Phys. Rev. A* **48**, 3890 (1993).
21. S. E. Harris, *Phys. Today* **50**, 36 (1997).
22. M. S. Bigelow, N. N. Lepeshkin and R. W. Boyd, *Phys. Rev. Lett.* **90**, 113903 (2003).
23. A. Ashkin, G. D. Boyd, J. M. Dziedzic, R. G. Smith, A. A. Ballman, J. J. Levinstein and K. Nassau, *Appl. Phys. Lett.* **9**, 72 (1966).
24. P. Günter and J.-P. Huignard (eds.), *Photorefractive Materials and Their Applications I*, Vol. 61 (Springer-Verlag, Berlin, Heidelberg, New York, 1988).
25. P. Günter and J.-P. Huignard (eds.), *Photorefractive Materials and Their Applications II*, Vol. 62 (Springer-Verlag, Berlin, Heidelberg, New York, 1989).
26. L. Solymar, D. J. Webb and A. Grunnet-Jepsen, *The Physics and Applications of Photorefractive Materials* (Clarendon Press, Oxford, 1996).
27. G. C. Valley, *J. Opt. Soc. Am B* **1**, 868 (1984).
28. P. Réfrégier, L. Solymar, H. Rajbenbach and J.-P. Huignard, *J. Appl. Phys.* **58**, 45 (1985).
29. S. L. Sochava, E. V. Mokrushina, V. V. Prokofev and S. I. Stepanov, *J. Opt. Soc. Am B* **10**, 1600 (1993).
30. S. I. Stepanov, V. V. Kulikov and M. P. Petrov, *Opt. Commun.* **44**, 19 (1982).
31. A. Marrakchi, J. P. Huignard and P. Günter, *Appl. Phys.* **24**, 131 (1981).
32. S. I. Stepanov and M. P. Petrov, Nonstationary holographic recording for efficient amplificaion and phase conjugation, in *Photorefractive Materials and Their Applications I*, Vol. 61 eds. P. Günter and J.-P. Huignard (Springer-Verlag, Berlin, Heidelberg, New York, 1988) pp. 263–289.

33. L. Solymar, D. J. Webb and A. Grunnet-Jepsen, *The Physics and Applications of Photorefractive Materials* (Clarendon Press, Oxford, 1996), pp. 157–169.
34. G. Zhang, R. Dong and J. Xu, *Chin. Phys. Lett.* **20**, 1725 (2003).
35. G. Zhang, R. Dong, F. Bo and J. Xu, *Appl. Opt.* **43**, 1167 (2004).
36. A. Shumelyuk, K. Shcherbin, S. Odoulov, B. Sturman, E. Podivilov and K. Buse, *Phys. Rev. Lett.* **93**, 243604 (2004).
37. Z. Deng and P. R. Hemmer, *SPIE* **5362**, 81 (2003).
38. Z. Deng, D. Qing, P. Hemmer, C. H. R. Ooi, M. S. Zubairy and M. O. Scully, *Phys. Rev. Lett.* **96**, 023602 (2006).
39. F. Bo, G. Zhang and J. Xu, *Opt. Commun.* **261**, 349 (2006).
40. F. Bo, G. Zhang and J. Xu, *TOPS* **99**, 386 (2005).
41. F. Bo, G. Zhang and J. Xu, *Opt. Express* **13**, 8198 (2005).
42. F. Gao, J. Xu, G. Zhang, F. Bo and H. Liu, *Appl. Phys. Lett.* **92**, 021121 (2008).
43. I. McMichael, P. Yeh and P. Beckwith, *Opt. Lett.* **13**, 500 (1988).
44. Q. Yang, J. T. Seo, B. Tabibi and H. Wang, *Phys. Rev. Lett.* **95**, 063902 (2005).
45. S. H. Lin, K. Y. Hsu and P. Yeh, *Opt. Lett.* **25**, 1582 (2001).
46. G. Zhang, W. Che, B. Han and Y. Qi, *Opt. Express* **15**, 2055 (2007).
47. F. Gao, J. Xu, H. Qiao, Q. Wu, Y. Xu and G. Zhang, *Opt. Commun.* **257**, 185 (2006).
48. G. P. Agrawal, *Nonlinear Fiber Optics* (Academic Press, San Diego, 2001).
49. F. Bo, Studies on dispersive phase coupling effect and ligh-group-velocity control, Ph.D. thesis, Nankai University, Tianjin, China, (2007).
50. S. Balasubramanian, I. Lahiri, Y. Ding, M. R. Melloch and D. D. Nolte, *Appl. Phys. B* **68**, 863 (1999).
51. M. Dinn, K. Nakagawa, M. R. Melloch, A. M. Weiner and D. D. Nolte, *J. Opt. Soc. Am B* **17**, 1313 (2000).

DOI: 10.1002/adma.200702547

Enhanced Optical Limiting Effects in Porphyrin-Covalently Functionalized Single-Walled Carbon Nanotubes**

By *Zhi-Bo Liu*, *Jian-Guo Tian*,* *Zhen Guo*, *Dong-Mei Ren*, *Feng Du*, *Jian-Yu Zheng*,* and *Yong-Sheng Chen*

Optical limiters are employed to protect sensitive optical components or eyes from laser-induced damage.[1,2] They have lower transmittance for high-intensity or fluence laser input while they keep a high linear transmittance. Many works have concentrated on creating ideal optical limiting devices by exploiting passive limiting mechanisms such as nonlinear absorption (multiphoton absorption, reverse saturable absorption (RSA)), nonlinear refraction (electronics or thermal effects), and nonlinear light scattering. Both single-walled carbon nanotube (SWNT) and multiwalled carbon nanotube (MWNT) suspensions have been reported to have strong optical limiting effects in the nanosecond regime, which arise from strong nonlinear light scatterings due to the creation of new scattering centers consisting of ionized carbon microplasmas and solvent microbubbles.[3–9] To promote their optical limiting effects, the optical nonlinear media with other optical nonlinear processes (e.g., two-photon absorption or RSA) have been blended with carbon nanotubes.[10,11] The association of SWNTs with organic chromophores having multiphoton absorption processes was recently shown to be a promising approach to achieve optical limiting systems with broad temporal and spectral responses.[10] Carroll et al.[11] also reported an enhanced nonlinear transmittance obtained by a RSA dye blended with carbon nanotubes. Recently, Blau et al.[12] presented a study on nonlinear optical characterization of stable porphyrin/SWNT composite solutions obtained by non-covalent bonding between the carbon nanotubes and conjugated tetraphenylporphyrin molecules.

However, little research has been carried out on optical limiting effects of covalently functionalized SWNTs with reverse saturable absorbents. Vivien et al.[5] predicted that further optimizations of the optical limiting performances of carbon nanotubes may be achieved by the cumulative influences of different nonlinear effects arising from functionalized carbon nanotubes with reverse saturable absorbents. Porphyrins are often used as visible chromophores to decorate the surfaces of semiconductor and metal nanoparticles, and they are also promising candidates for applications in optical limiters owing to their large RSA in the visible even near-infrared wavelength range.[13–15] Furthermore, an effective energy or electron transfer may exist in the functionalized SWNTs with porphyrins.[16] The photoinduced electron transfer can result in a large optical limiting effect, which has been observed in the PVK-modified SWNTs system.[17,18] We also reported that a covalently 5-*p*-aminophenyl-10,15,20-triphenylporphyrin-functionalized SWNTs exhibits a strong optical limiting.[19] In this Communication, we present the large enhancement of optical limiting effects in three covalently functionalized SWNTs with porphyrins at 532 nm, and the contribution of photoinduced electron or energy transfer to enhanced optical limiting is discussed.

The structures of porphyrin-functionalized SWNTs, SWNT-TPP (**I**), SWNT-NH-TPP (**II**), and SWNT-SnDPP (**III**) are shown in Figure 1. The SWNT sample was produced by using the arc-discharge method with NiO/Y_2O_3 as catalyst.[20] According to the established relationship between radial breathing mode (RBM) frequency and tube diameter,[21] individual tubes have a diameter range of 1.4–1.7 nm. 5,10,15,20-tetraphenylporphyrin (TPP), 5-*p*-aminophenyl-10,15,20-triphenylporphyrin (NH_2TPP) and trans-dihydroxo [5,15-bis-(3,5-diocty-loxyphyenyl)porphyrin]Tin(IV) ($Sn(OH)_2DPP$) were also prepared for a comparison of their optical properties with functionalized SWNTs'. Further details of the SWNTs' functionalization can be found in the Experimental section.

Shown in Figure 2 are the absorption and fluorescence spectra of TPP, NH_2TPP, $Sn(OH)_2DPP$, **I**, **II**, and **III** in *N*,*N*-dimethylformamide (DMF) solutions. It is seen from the absorption spectrum of **I** shown in Figure 2a that its Soret band and Q-band have 5 nm and 4–7 nm red-shift relative to TPP in DMF respectively, and its Soret band has a notable broadening relative to the porphyrin moiety. A similar notable

[*] Prof. J.-G. Tian, Dr. Z.-B. Liu
The Key Laboratory of Weak Light Nonlinear Photonics, Ministry of Education, and Teda Applied Physics School
Nankai University
Tianjin 300457 (P.R. China)
E-mail: jjtian@nankai.edu.cn
Prof. J.-Y. Zheng, Dr. Z. Guo, D.-M. Ren
State Key Laboratory of Elemento-Organic Chemistry
Nankai University
Tianjin 300071 (P.R. China)
Dr. F. Du, Prof. Y.-S. Chen
Center for Nanoscale Science and Technology and
Key Laboratory for Functional Polymer Materials
College of Chemistry, Nankai University
Tianjin 300071 (P.R. China)

[**] This work was supported by the Natural Science Foundation of China (10574075, 60708020, and 20421202), the Chinese National Key Basic Research Special Fund (2006CB921703), the 973 Program (2006CB932900) and the Program for Changjiang Scholars and Innovative Research Team in University.

ADVANCED MATERIALS

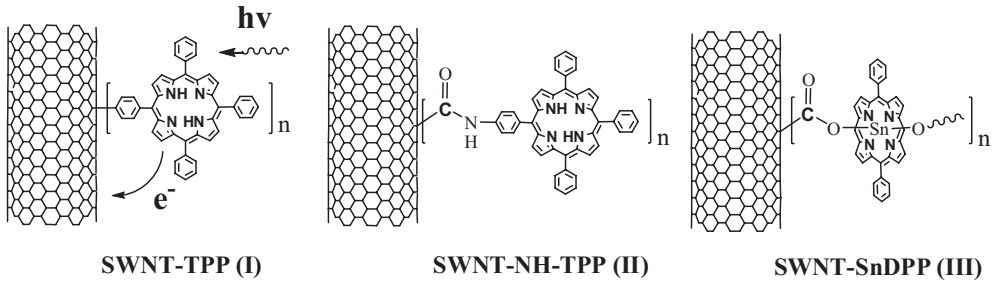

Figure 1. Structures of porphyrin-covalently functionalized SWNTs **I**, **II**, and **III**.

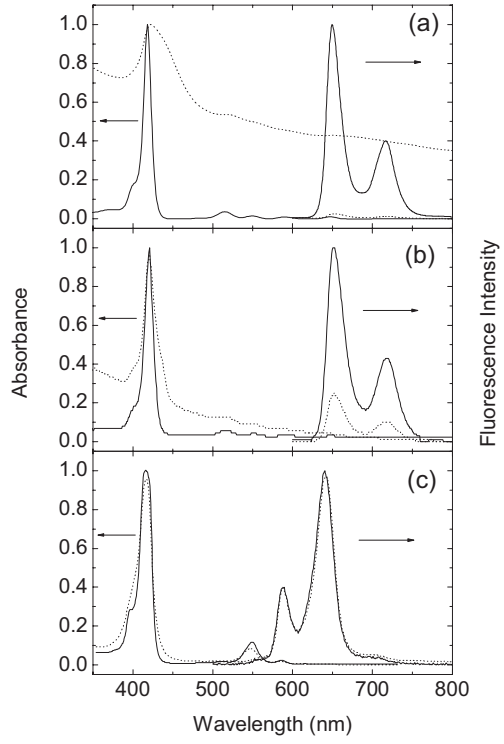

Figure 2. Absorption and fluorescence spectra of a) **I** (dotted line) and TPP (solid line), b) **II** (dotted line) and NH_2TPP (solid line), c) **III** (dotted line) and $Sn(OH)_2DPP$ (solid line).

broadening of the Soret band in **II** relative to the porphyrin moiety can be observed as shown in Figure 2b, however, there is no red-shift of the Soret band. The UV-vis absorption spectrum of **III** (Fig. 2c) is similar to that of $Sn(OH)_2DPP$ because the effect of carbon nanotube absorption on the porphyrin peak positions is relatively small.[16] In order to probe excited state interactions of porphyrins and SWNTs, the fluorescence spectra of **I**, **II**, **III**, TPP, NH_2TPP and $Sn(OH)_2DPP$ were measured, as shown in Figure 2a. Upon excitation of the porphyrin moiety in Soret band, the solution of **I** exhibits 97 % quenching of fluorescence emission at 651 nm and 717 nm. The fluorescence spectrum of **II** has the same profile as that of TPP, but its fluorescence quantum yield is only about 25 % of that of NH_2TPP (Fig. 2b). Therefore, the magnitude of fluorescence quenching of **I** is larger than that of **II**. The previously reported porphyrin–nanotube hybrids linked by flexible chains[16] exhibits the excited-state energy transfer quenching of porphyrin fluorescence caused by SWNTs, which is dependent on the length of the tether linking the porphyrin moiety to the nanotube. However, as the linkage chains become shorter no fluorescence quenching occurs.[16] **III** has a shorter tether linking the porphyrin ring to SWNTs than **II**, thus both its fluorescence spectral profile and intensity hardly changed from $Sn(OH)_2DPP$ to **III**, indicating that almost no fluorescence quenching occurred (Fig. 2c). For the composite **I**, the effective quenching can be explained by the extended conjugated π-system of SWNTs with a porphyrin-mediated through-bond mechanism owing to the unique direct linkage mode of the two moieties.[22,23] A possible pathway to the deactivation of excited porphyrin can be attributed to two competitive processes, energy transfer (ET) and photoinduced electron transfer (PET).

Since it was predicted that the further optimizations of optical limiting performances of nanotubes may be achieved by the accumulation of different nonlinear effects by functionalizing carbon nanotubes with reverse saturable absorbents,[5] we performed the nonlinear transmittance measurements to compare optical limiting effects of porphyrin-functionalized SWNTs. The characteristics of output fluence vs. input fluence for these samples are shown in Figure 3a, and the curves of nonlinear transmittance vs. input fluence are shown in Figure 3b. C_{60} solution in toluene was employed as a reference. For comparison, all of the samples were set to have same linear transmittance of 75 % at 532 nm by adjusting their concentration. From Figure 3, it can be seen that the optical limiting effects of three porphyrins functionalized SWNTs (**I**, **II**, and **III**) are much better than not only C_{60} and SWNTs, but also these individual porphyrins (TPP and $Sn(OH)_2DPP$). The optical limiting thresholds of **I**, **II**, and **III** are approximately 70, 100, and 150 $mJ \cdot cm^{-2}$, respectively, all of which are much smaller than those of C_{60} (300 $mJ \cdot cm^{-2}$) and SWNTs (250 $mJ \cdot cm^{-2}$). At the highest fluence (95 $mJ \cdot cm^{-2}$) used in our experiments, the transmittance has decreased to 4.3 %, 5.1 %, and 6.6 % for **I**, **II**, and **III**, respectively, while the transmittance is 11.3 %, 9.9 %, 21 %, and 33.5 % for C_{60}, SWNTs, TPP, and $Sn(OH)_2DPP$, respectively. This illustrates that enhanced optical limiting effects can be

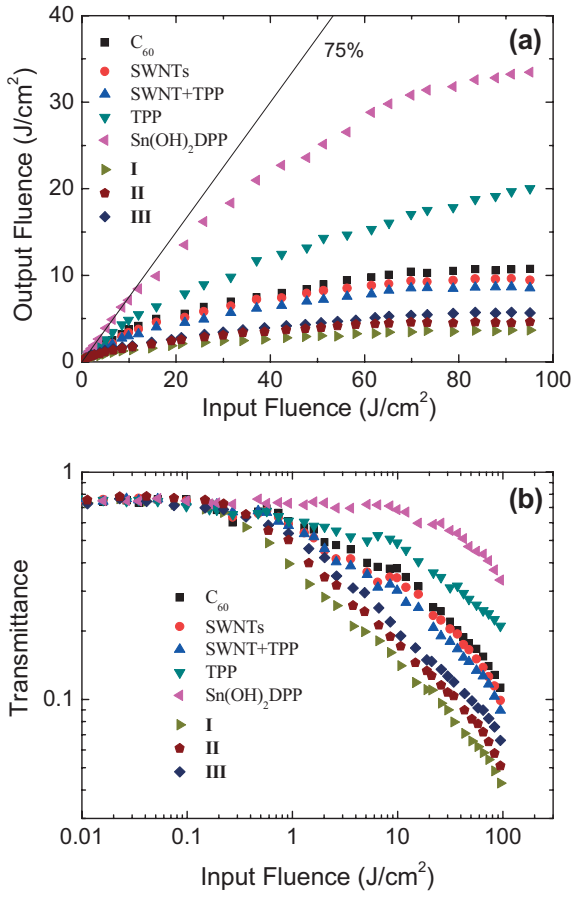

Figure 3. The optical limiting of C_{60}, SWNTs, SWNT+TPP, TPP, $Sn(OH)_2DPP$, **I**, **II**, and **III** for 5-ns pulsed laser at 532 nm. a) Output fluence vs. input fluence. b) Nonlinear transmittance spectra vs. input fluence. The linear transmittance for all of the samples was adjusted to 75 %.

obtained by functionalizing SWNTs with RSA chromophore porphyrins.

As we know, nonlinear transmittance can be enhanced by blending a RSA dye with carbon nanotubes.[11] To compare functionalized SWNTs with blended system, we also performed the optical limiting measurements of SWNTs blended with TPP, as shown in Figure 3. Because the content of porphyrin in **I** was about 30 %, which was determined by thermogravimetric analysis[24] and the fittings of the absorption spectra of SWNTs and **I**, the sample of 7:3 weight ratio of SWNTs to TPP was used as the blended system, and its linear transmittance was also adjusted to 75 % at 532 nm. The optical limiting effect of SWNT+TPP blended system is better than those of C_{60}, SWNTs, and TPP, since the shortcomings of these individual materials' optical limiting are compensated by combining these materials into a single system.[11] However, the functionalized SWNTs with porphyrin may be more suitable for the application in optical limiting than SWNT+TPP blended system as shown in Figure 3. In SWNT+TPP blended system, although nonlinear transmittance can be availably enhanced by complementary nonlinear mechanisms, linear absorption has been also increased simultaneously. Under same concentrations of 20 $mg \cdot L^{-1}$, the linear transmittances of **I** and SWNT+TPP are 70 % and 55 %, respectively. The increase of linear absorption can partially restrict the enhancement of optical limiting effect.

To get a better insight into the optimizations of the optical limiting performances of porphyrin functionalized SWNTs, we carried out open-aperture *Z*-scan experiments of SWNTs, SWNT+TPP, **I**, **II**, and **III** with the same concentration of 20 $mg \cdot L^{-1}$, and results are shown in Figure 4a. The linear transmittances of SWNTs, SWNT+TPP, **I**, **II**, and **III** are 64 %, 55 %, 70 %, 68 %, and 75 %, respectively. The composite **I** has a largest dip among the transmittance curves of these materials, indicating that it should has the best optical limiting effect. Although the combination of nonlinear scattering with RSA can improve the optical limiting effect effectively, we believe that the enhanced limiting performance arises from not only the combination of nonlinear mechanism, but also the photoinduced electron or energy transfer from electron donor TPP moiety to acceptor SWNTs.[17,18] From Figures 2 and 3, it can be seen that **I** with stronger fluorescence quenching (about 97 %) has a better optical limiting effect than **II** (about 75 %). This photoinduced electron transfer could produce a charge-separated excited state and result in a

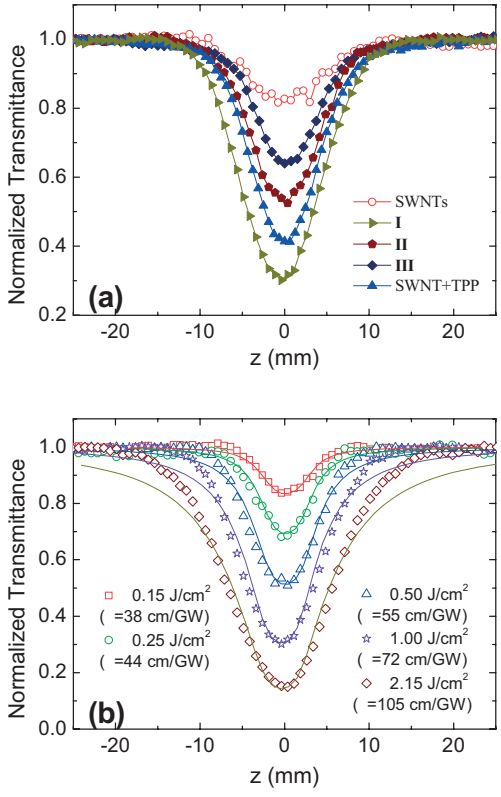

Figure 4. Open-aperture *Z*-scan curves for 5ns pulsed laser at 532 nm. a) *Z*-scan curves of SWNTs, SWNT+TPP, **I**, **II**, and **III** with same concentration of 20 $mg \cdot L^{-1}$, b) *Z*-scan curves of **I** for different input fluence. The solid lines are the numerical fittings.

ADVANCED MATERIALS

large optical limiting effect, just as the semiconducting polymer/methano-fullerence system reported previously.[25] Comparatively there is almost no fluorescence quenching occurring in the composite **III**, and the enhancement of optical limiting effect for **III** is the smallest among three functionalized SWNTs.

Figure 4b gives the open-aperture *Z*-scan curves of **I** for different input fluence. Using the Crank–Nicolson finite-difference scheme, we fitted the *Z*-scan curves numerically (the solid lines) and obtained the values of nonlinear absorption coefficient, β, as shown in Figure 4b. In general, the value of β will decrease as input fluence increases for RSA process because of the saturation of RSA,[26] and however it will keep unchanged for two-photon absorption process. The increase of β with input fluence implies that besides nonlinear absorption the observed optical limiting performance is also influenced by nonlinear scattering in the high-fluence regime. The similar phenomena were also observed in the composites II and III. In SWNTs and porphyrin non-covalent blended system, the nonlinear absorption coefficient β will decrease as intensity increases.[12] This may be due to the saturation of the accessible energy levels under high-intensity pumping.

In summary, functionalizing SWNTs with RSA chromophores porphyrins can enhance optical limiting performance. The porphyrins covalently functionalized SWNTs offer superior performance to C_{60}, the individual SWNTs and porphyrins by combination of nonlinear mechanism and the photoinduced electron or energy transfer between porphyrin moiety and SWNTs. Further studies to understand better the mechanism and the structure–property correlations are currently in progress.

Experimental

SWNT-TPP: The SWNTs sample was produced by arc-discharge method. It was purified via oxidative acid treatment according to an established procedure. 6.3 mg of purified SWNTs was sonicated for 4 h in 7.5 mL *o*-dichlorobenzene (ODCB). To this suspension was added 20 mg (0.032 mmol) 5-*p*-aminophenyl-10,15,20-triphenylporphyrin (NH_2TPP) in 2.0 mL of acetonitrile. After transfer to a septum-capped flask and bubbling with nitrogen for 10 min, 10 μL (0.074 mmol) of isoamyl nitrite was quickly added and the suspension was stirred in dark at 70 °C under the protection of nitrogen for 48 h. Another 100 mg (0.16 mmol) 5-*p*-aminophenyl-10,15,20-triphenylporphyrin and 50 μL (0.37 mmol) isoamyl nitrite were added in 5 times (total 5 × 20 mg TPP-NH_2 and 5 × 10 μL isoamyl nitrite) during this period to ensure high degree of functionalization. After cooling to room temperature, the suspension was diluted with 10 mL *N*,*N*′-dimethylformamide (DMF), filtered over a nylon membrane (0.1 μm), and washed extensively with DMF. Sonication and redispersion were repeated in DMF and then in ether to remove the adsorbed porphyrin and solvent. The final product was collected by filtration over a nylon membrane (0.1 μm) and dried in vacuum at 80 °C for 10 h to give modified SWNTs as black powder (5.8 mg).

SWNT-NH-TPP: The SWNTs were treated as the same above. After the oxidation process, about 10 %(Weight) of carboxylic acid groups were introduced to the surface and end of SWNTs. Then purified SWNTs sample was treated with thionyl chloride at 70 °C for 24 h. After the complete removel of excess thionyl chloride, porphyrin [5-(4-aminophenyl)-10,15,20-triphenylporphyrin] was added, the DMF solution was stirred in the presence of triethylamine at 100 °C under nitrogen protection for 2 days. The funcitonalized SWNTs were isolated by washing off the unreacted porphyrin with a large amount of chloroform on 0.2 um pore size nylon membrane, with the help of sonication to disperse the solid, the removal of free porphyrin was accomplished via washing with diluted acetic and triethylamine, finally with chloroform. The product was then dried at 60 °C for 9 h under vacuum.

SWNT-SnDPP: The SWNTs were treated as the same above. In a typical $Sn(OH)_2$DPP porphyrin covalent solubilization experiment, a purified SWNT sample (49 mg) was added to a solution of $Sn(OH)_2$DPP in THF (10 mg mL^{-1}, 10 mL), and the mixture was sonicated for 48 h. After the removal of THF on a rotary evaporator, the solid mixture was extracted repeatedly with hexanes, coupled with vigorous centrifuging, to remove free $Sn(OH)_2$DPP. Then, THF was added to the solid sample to dissolve the SnDPP-attached SWNTs. Upon vigorous centrifuging, the solid residue was collected and then used to go through the same covalent solubilization procedure again. The soluble SWNT–SnDPP samples from the two repeated experiments were combined, followed by a complete evaporation of the solvent THF, the residue was dried at 60 °C for 9 h under vacuum.

Measurements: The optical limiting and *Z*-scan experiments were preformed with linearly polarized 5 ns pulses at 532 nm generated from a frequency doubled Q-switched Nd:YAG laser. The spatial profiles of the pulses were of nearly Gaussian distribution after the spatial filter. The pulses were split into two parts. The reflected pulse was used as reference, and we focused the transmitted pulse onto the sample by using a 150 mm focal length lens. The sample was placed at the focus where the spot radius of the pulses was (25 ± 2) μm. The reflected and transmitted pulse energies were measured simultaneously with two energy detectors (Molectron J3S-10). C_{60} was employed as a standard. For optical limiting experiments, all of the sample concentrations were adjusted to have same linear transmittance of 75 % at 532 nm in 5 mm quartz cells. For *Z*-scan experiments, the samples have same concentration of 20 $mg \cdot L^{-1}$.

Received: October 10, 2007
Revised: November 8, 2007
Published online: January 17, 2008

[1] L. W. Tutt, A. Kost, *Nature* **1992**, *356*, 225.
[2] L. W. Tutt, T. F. Boggess, *Prog. Quantum Electron.* **1993**, *17*, 299.
[3] X. Sun, R. Q. Yu, G. Q. Xu, T. S. A. Hor, W. Ji, *Appl. Phys. Lett.* **1998**, *73*, 3632.
[4] P. Chen, X. Wu, X. Sun, J. Lin, W. Ji, K. L. Tan, *Phys. Rev. Lett.* **1999**, *82*, 2548.
[5] L. Vivien, P. Lancon, D. Riehl, F. Hache, E. Anglaret, *Carbon* **2002**, *40*, 1789.
[6] L. Vivien, D. Riehl, F. Hache, E. Anglaret, *Phys. B* **2002**, *323*, 233.
[7] X. Sun, Y. Xiong, P. Chen, J. Lin, W. Ji, J. H. Lim, S. S. Yang, D. J. Hagan, E. W. Van Stryland, *Appl. Opt.* **2000**, *39*, 1998.
[8] L. Vivien, D. Riehl, P. Lancon, F. Hache, E. Anglaret, *Opt. Lett.* **2001**, *26*, 223.
[9] L. Vivien, D. Riehl, J. F. Delouis, J. A. Delaire, F. Hache, E. Anglaret, *J. Opt. Soc. Am. B* **2002**, *19*, 208.
[10] N. Izard, C. Ménard, D. Riehl, E. Doris, C. Mioskowski, E. Anglaret, *Chem. Phys. Lett.* **2004**, *391*, 124.
[11] S. Webster, M. Reyes-Reyes, X. Pedron, R. López-Sandoval, M. Terrones, D. L. Carroll, *Adv. Mater.* **2005**, *17*, 1239.
[12] E. M. N. Mhuircheartaigh, S. Giordani, W. J. Blau, *J. Phys. Chem. B* **2006**, *110*, 23136.
[13] W. J. Blau, H. Byrne, W. M. Dennis, J. M. Kelly, *Opt. Commun.* **1985**, *56*, 25.
[14] K. McEwan, P. Fleitz, J. Rogers, J. Slagle, D. McLean, H. Akdas, M. Katterle, I. Blake, H. Anderson, *Adv. Mater.* **2004**, *16*, 1933.

[15] M. O. Senge, M. Fazekas, E. G. A. Notaras, W. J. Blau, M. Zawadzka, O. B. Locos, E. M. Ni Mhuircheartaigh, *Adv. Mater.* **2007**, *19*, 2737.
[16] H. Li, R. B. Martin, B. A. Harruff, R. A. Carino, L. Allard, Y. P. Sun, *Adv. Mater.* **2004**, *16*, 896.
[17] W. Wu, S. Zhang, Y. Li, J. Li, L. Liu, Y. Qin, Z. X. Guo, L. Dai, C. Ye, D. Zhu, *Macromolecules* **2003**, *36*, 6286.
[18] C. Li, C. Liu, F. Li, Q. Gong, *Chem. Phys. Lett.* **2003**, *380*, 201.
[19] Z. Guo, F. Du, D. M. Ren, Y. S. Chen, J. Y. Zheng, Z. B. Liu, J. G. Tian, *J. Mater. Chem.* **2006**, *16*, 3021.
[20] X. Lv, F. Du, Y.-F. Ma, Q. Wu, Y.-S. Chen, *Carbon* **2005**, *43*, 2020.
[21] M. S. Dresselhaus, G. Dresselhaus, A. Jorio, A. G. Souza Filho, R. Saito, *Carbon* **2002**, *40*, 2043.
[22] C. Luo, D. M. Guldi, H. Imahori, K. Tamaki, Y. Sakata *J. Am. Chem. Soc.* **2000**, *122*, 6535.
[23] J.-S. Hsiao, B. P. Krueger, R. W. Wagner, T. E. Johnson, J. K. Delaney, D. C. Mauzerall, G. R. Fleming, J. S. Lindsey, D. F. Bocian, R. J. Donohoe, *J. Am. Chem. Soc.* **1996**, *118*, 11181.
[24] L. Zeng, L. Zhang, A. R. Barron, *Nano Lett.* **2005**, *5*, 2001.
[25] N. S. Sariciftci, L. Smilowitz, A. J. Heeger, F. Wudl, *Science* **1992**, *258*, 1474
[26] R. L. Sutherland, *Handbook of Nonlinear Optics*, 2nd ed., Marcel Dekker, New York **2003**.

Paraxial energy transport of a focused Gaussian beam in ruby with nondegenerate two-wave couplinglike mechanism

Feng Gao,[a] Jingjun Xu,[b] Guoquan Zhang, Fang Bo, and Haixu Liu
Photonics Center, College of Physics Science, Nankai University, Tianjin 300457, China and Key Laboratory of Weak Light Nonlinear Photonics (Nankai University, Tianjin 300457), Ministry of Education, China

(Received 1 September 2007; accepted 2 December 2007; published online 17 January 2008)

Paraxial energy transport of an intensity-modulated and focused Gaussian beam is studied in ruby. Deformations of the temporal profiles are observed under different conditions and explained by the interplay among a nondegenerate two-wave couplinglike mechanism, the population oscillations, and the Fraunhofer diffraction. Experimental evidence is provided for the existence of a nondegenerate two-wave couplinglike mechanism. The self-superluminal can be observed under proper conditions. A group velocity of −83 m/s is achieved with a Gaussian-like-modulated pulse of 30 ms with background illumination. Based on these results, a method to control the group velocity of a single beam in such media is proposed. © *2008 American Institute of Physics*. [DOI: 10.1063/1.2827568]

The essence of controlling the group velocity of light is to control the dispersion of the material. Among the various applications are real-time optical delay lines and optical buffers. Several methods have been proposed to manipulate the material dispersion in order to control the group velocity,[1–12] but most of them require a separated pump beam to get a large change of the group velocity. In 2003, Bigelow *et al.* found subluminal propagation in ruby and explained it by the creation of a spectral hole via coherent population oscillations.[6] Besides a large time delay, their method has the advantage to be a self-delay of the signal beam, i.e., a subluminal behavior without pump beam, which makes ruby a promising material to control the group velocity of light. There is also a theoretical analysis of the propagation of a pulse with different temporal frequencies.[7] They only predict subluminal light propagation in the ruby, yet the ruby needs a strong focusing beam to exploit the refractive index change, and, furthermore, the laser beam is usually a TEM_{00} Gaussian beam and thus exhibits different spatial frequencies. If the intensity of the beam is modulated in time, we may expect a contribution similar to the effect of nondegenerate two-wave coupling[8–12,15] (NDTWC) that arises from mixing of different spatial frequency components with a dispersive coupling coefficient Γ_{ph} because of the limited response rate of the saturable resonant interaction of the ruby. Such a dispersive wave coupling effect would lead to superluminal/subluminal light propagation. Since there is actually only one beam, we call this a NDTWC-like mechanism. In this letter, we study the deformation of the paraxial part of a focused TEM_{00} Gaussian pulse after the ruby and provide evidence for the NDTWC-like mechanism and its contributions to the group velocity control in ruby. At the same time, we observed superluminal propagation at low spatial frequencies in ruby with little deformation. A convenient method is demonstrated to control the group velocity of light without separated pump beams in the medium with a NDTWC effect.

The configuration of our experiment is shown in Fig. 1. A 532 nm TEM_{00} laser beam was temporally modulated by an electro-optic (EO) modulator to generate pulses. A small part of the modulated beam was sent via the beam splitter (BS) and mirror M1 into a detector D1. This served as a reference and also acted as the trigger of the oscilloscope. After being focused by a lens of 300 mm focal length, the transmitted beam was directed into a 100 mm long ruby rod set on a translation stage. The position Z of the ruby with respect to the lens could be changed conveniently along the direction of the beam. An aperture of 1.5 mm diameter was placed just in front of another detector D2 and was 840 mm away from the lens. Therefore only the paraxial part of the transmitted beam was detected as a signal by D2. The temporal traces of the reference and the signal beams were monitored by an oscilloscope and the time delay of the signal beam with respect to the reference beam could be measured.

In the experiment, a 30 ms Gaussian pulse with a peak power of 490 mW and a background power of 100 mW was used. The temporal profiles of the transmitted signal pulses at different Z's near the focal spot of the lens are presented in Fig. 2. The dashed curve shows the pulse profile of the reference and the vertical line indicates its peak position. The solid curves are the paraxial signal pulse profiles at different Z's. We notice that there are large asymmetrical deformations of the pulses at certain positions, for example, when the crystal was placed at $Z=313$, 308, 273, and 258 mm. However, we also observed clear superluminal propagation at certain places that largely maintained their symmetric Gaussian-like pulse profiles. For example, a time advance of 1.2 ms was observed for $Z=233$ mm, which corresponds to a negative group velocity of −83 m/s. In the case of a sinusoidally modulated beam, similar superluminal propagation could also be observed.

The serious deformations at certain Z's are mainly caused by the self-phase modulation of the beam and by the Fraunhofer diffraction from the back surface of the sample. When the input beam was kept at its peak intensity of 490 mW, a structure with one ring could be observed in the far field with the ruby placed at these Z's of large deforma-

[a]Electronic mail: fenggao@nankai.edu.cn.
[b]Electronic mail: jjxu@nankai.edu.cn.

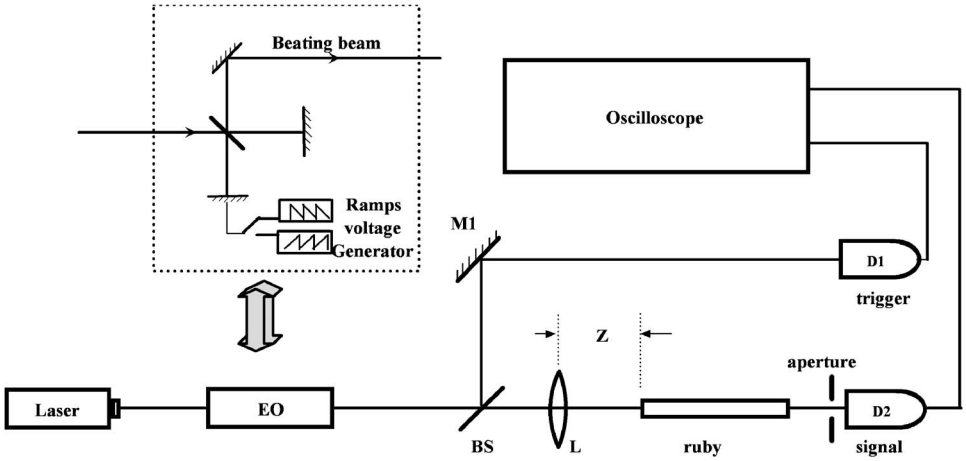

FIG. 1. Experimental configuration: laser (Verdi-10) is at 532 nm, EO is the electro-optic modulator, BS is the beam splitter, M1 is a mirror, D1 and D2 are photodetectors, and L is a 300-mm-focal-length lens. Z is the distance from the front surface of the ruby to the lens. The inset in the dotted rectangle is a replacement of EO to generate the beating beams.

tions. The ring structure is originated from the self-phase-modulation effect of a high intensity Gaussian beam.[14] Whether the center of the rings is dark or bright is rather complicated, but roughly speaking, it is mainly decided by the wave-front curvature of the beam and the nonlinearity of the sample.[15] For a light wave with an intensity much less than the saturation intensity in ruby, the nonlinearity is weak (the real part n_2 of the nonlinear index of ruby $\sim 10^{-8}$ cm^2/W) (Ref. 13) and the large absorption (0.69 cm^{-1} in the sample) leads to a rapid decrease in the intensity of the beam inside the sample. As a consequence, the total self-induced phase change is very small and only one diffraction ring is observed in the experiment.

When the intensity of the beam is modulated, the self-phase modulation of the beam inside the sample changes accordingly, and consequently the diffraction pattern in the far field. The self-phase modulation is only intensity dependent, which means that the pulse should be symmetric even if there was deformation in its temporal profile. Considering the relaxation of the medium, the self-phase modulation is related to the history of the intensity of the incident beam, so it is with the Fraunhofer diffraction pattern in the far field. This is the main reason for the large asymmetrical deformations of the temporal profile of the paraxial energy.

Besides the case with large deformations of the pulse, one can also see pulses of only little deformation that exhibits a superluminal behavior (for example, Z=233 mm in Fig. 2). The result indicates abnormal dispersion under the given conditions. The group index of the modulated beam based on the population oscillation effect is given by[6]

$$n_g = n_1 + \frac{\alpha_0 c T_1}{2} \frac{I_0}{1+I_0}\left[\frac{1}{(T_1\delta)^2 + (1+I_0)^2}\right], \quad (1)$$

where n_g is the group index of the ruby, n_1 is the refractive index, I_0 is the normalized pump intensity, δ is the temporal frequency deviation from the frequency of the pump beam, α_0 is the unsaturated absorption coefficient, c is the invariant speed, and T_1 is the ground state recovery time of the ruby. It is shown that the group index is always larger than the refractive index of the ruby, which provides a good explanation for the subluminal light propagation, but not for the superluminal results observed in the experiment.

We believe that the superluminal light propagation is mainly the result of a NDTWC-like process. To find evidence for the process, we have to distinguish it from the other effects mentioned above, i.e., the coherent population oscillations and the Fraunhofer diffraction. Fortunately, both effects are intensity dependent. However, we will show in the following that the group velocity of light propagating in ruby also depends on frequency shift and it could cause superluminal result.

We know that the NDTWC process can occur in ruby between two beams of different frequencies under appropriate conditions.[13] Since a modulated TEM$_{00}$ beam consists, not only of different temporal, but also of different spatial

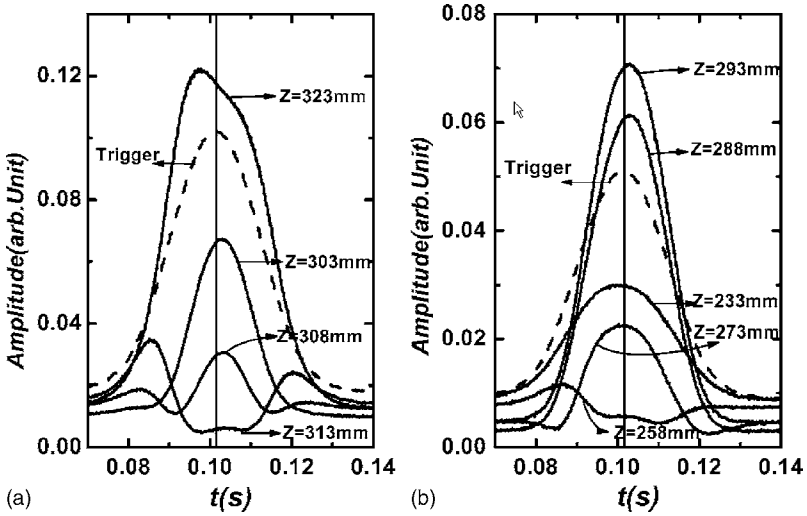

FIG. 2. Temporal profiles of the transmitted paraxial pulses with different Z's.

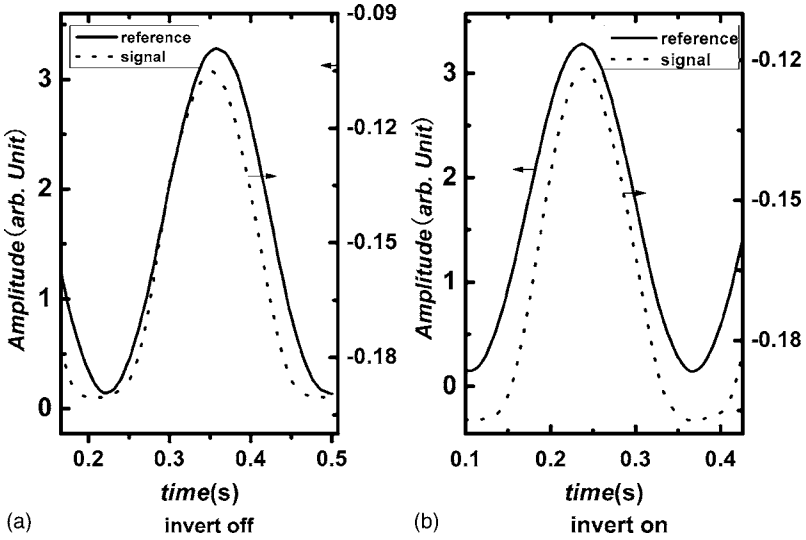

FIG. 3. Proof for the existence of a NDTWC-like mechanism: (a) with a downward ramp voltage applied to the PZD mirror, (b) with the upward ramp voltage applied to the PZD mirror. The solid and the dashed curves are the temporal traces for the reference and the signal pulses, respectively. The result shows the signal beam is changing from superluminal to subluminal behavior thus testifying the existence of a NDTWC-like mechanism. Note that the intensity modulation and the setup are all the same whereas the frequency shift is opposite.

frequency components, these frequency components may interact with each other in ruby via a NDTWC-like process. The dispersive coupling coefficient Γ_{ph} could have a sharp negative or positive dispersion slope and thus leads to superluminal as well as subluminal propagations.[8–12] The coupling coefficient Γ_{ph} for the NDTWC process depends not only on the intensity but also on the frequencies shift between two coupling beams.[13] Therefore, exchanging the frequency of the signal and the reference beam will result in the change of the dispersion slope of Γ_{ph}, i.e., the change in the group velocity of the pulse. This is confirmed by the following experiment.

A beating beam with only two temporal frequencies is introduced. In the experiment, the EO was replaced by a Michelson interferometer with one of the mirrors being a piezoelectric-driven (PZD) mirror, as shown in the inset of Fig. 1. Thus a beating beam was obtained when a voltage ramp was applied to the PZD mirror. By shifting the driving voltage from upward ramps to downward ramps, we could control the frequency shift δ to be positive or negative between the two frequency components to be positive or negative while keeping the intensity modulation and the experiment setup the same. Therefore, the population oscillations and the Fraunhofer diffraction are all the same. Yet, when we inverted the ramp of the driving voltage, a transition from the superluminal to the subluminal was observed for the beating beam, as shown in Fig. 3. This clearly indicates a NDTWC-like process between the two frequency components in ruby. Actually the situation inside the sample is very complicated, including the NDTWC-like process which leads to the superluminal or the subluminal result, the population oscillations which leads to the subluminal result, the large absorption along the sample, and the Fraunhofer diffraction. They compete with each other and only for certain conditions one of them will be dominant. Exact solution and simulation of the process are important but complicated because of the complicated competition and interaction between different effects, and it deserves a more detailed investigation.

In conclusion, we studied the paraxial energy transport of a focused Gaussian beam in presence of a NDTWC-like mechanism in ruby. By adjusting the position of the sample, we observed self-induced superluminal as well as subluminal propagation of the pulse with lower spatial frequency. A negative group velocity of -83 m/s was observed for a 30 ms Gaussian pulse. This kind of self-induced changes in the group velocity reported here should also exist in other media with a NDTWC process.

This work is supported by the Program for Changjiang Scholars and Innovative-Research Team in University, the Key International S&T Cooperation Project (2005DFA10170), the NSFC (10334010 and 60678021), the 111 Project (B07013), the Key Project of Chinese Ministry of Education (No. 105043), the Program for New Century Excellent Talents in University (NCET-04-0234), the Municipal International Cooperation Program of Tianjin (No. 06YFGHHZ00500 and 06YFGHHZ00800), the National Basic Research Program of China (No. 2007CB307002), and CNKBRSF (No. 2006CB921703). The authors thank Romano A. Rupp for proofreading the manuscript.

[1] L. V. Hau, S. E. Harris, Z. Dutton, and C. H. Behroozi, Nature (London) **397**, 594 (1999).
[2] A. V. Turukhin, V. S. Sudarshanam, M. S. Shahriar, J. A. Musser, B. S. Ham, and P. R. Hemmer, Phys. Rev. Lett. **88**, 023602 (2002).
[3] C. P. Kuo, U. Osterberg, C. T. Seaton, G. I. Stegeman, and K. O. Hill, Opt. Lett. **13**, 1032 (1988).
[4] S. H. Lin, K. Y. Hsu, and P. Yeh, Opt. Lett. **25**, 1582 (2000).
[5] H. Su and S. L. Chuanga, Appl. Phys. Lett. **88**, 061102 (2006).
[6] M. S. Bigelow, N. N. Lepeshkin, and R. W. Boyd, Phys. Rev. Lett. **90**, 113903 (2003).
[7] Q. Yang, J. Seo, B. Tabibi, and H. Wang, Phys. Rev. Lett. **95**, 063902 (2005).
[8] G. Zhang, R. Dong, and J. Xu, Chin. Phys. Lett. **20**, 1725 (2003).
[9] G. Zhang, R. Dong, F. Bo, and J. Xu, Appl. Opt. **43**, 1167 (2004).
[10] G. Zhang, F. Bo, R. Dong, and J. Xu, Phys. Rev. Lett. **93**, 133903 (2004).
[11] F. Bo, G. Zhang, and J. Xu, Proceedings of the TOPS 99, Photorefractive Effects, Materials, and Devices, 2005 (unpublished), p. 386.
[12] F. Bo, G. Zhang, and J. Xu, Opt. Express **13**, 8198 (2005).
[13] E. Santamato and Y. R. Shen, Opt. Lett. **9**, 564 (1984).
[14] K. He and L. Deng, Laser Part. Beams **15**, 940 (2003).
[15] I. McMichael, P. Yeh, and P. Beckwith, Opt. Lett. **13**, 500 (1988).

Long luminescence lifetime in self-assembled InGaAs/GaAs quantum dots at room temperature

Zhangcheng Xu,[1,a)] Yating Zhang,[1] and Jørn M. Hvam[2]
[1]*Nano-photonics Group, Key Laboratory of Weak-Light Nonlinear Photonics Materials (MOE), TEDA College, Nankai University, Tianjin 300457, People's Republic of China and State Key Laboratory of Infrared Physics, Shanghai Institute of Technical Physics, Chinese Academy of Sciences, Yutian Road No. 500, Shanghai 200083, People's Republic of China*
[2]*Department of Photonics Engineering, Technical University of Denmark, Ørsteds Plads 343, DK-2800 Lyngby, Denmark*

(Received 15 September 2008; accepted 18 October 2008; published online 6 November 2008)

Time-resolved photoluminescence (PL) measurements of high-quality self-assembled small $In_{0.5}Ga_{0.5}As/GaAs$ quantum dots (QDs) show that the PL decay time of the QD ground state transition is nearly constant when the temperature is below 80 K and increases monotonously from 1.0 to 5.5 ns when the temperature increases from 80 to 300 K. The increased radiative lifetime of the QD ground state at higher temperatures is attributed to the thermal population of the subwetting-layer continuum states and could be one of the fundamental reasons for the low modal gain of the QD ground state transition in single-layer self-assembled QD lasers. © *2008 American Institute of Physics*. [DOI: 10.1063/1.3021018]

Research on self-assembled semiconductor quantum dots (QDs) has received much attention due to their potential application in optoelectronics devices, such as QD lasers.[1] The radiative lifetime of the excitons in QDs at room temperature is one of the most important device parameters, being inversely proportional to the modal gain of QD lasers.[2–5] The radiative lifetime of strongly confined excitons in QDs, where the energy separation between the ground state and the first excited exciton state is larger than the thermal energy k_BT (k_B is the Boltzmann constant and T is the temperature), should be almost independent of T. However, in real QDs, the radiative lifetime of the ground state excitons is expected to increase with increasing temperature due to the thermal population of optically inactive or poorly active exciton states.[6–8] This phenomenon was first observed in InGaAs/GaAs QDs by Wang *et al.*[9] in 1994, in InAs/GaAs QDs by Yu *et al.*[10] in 1996, and by other groups later.[11] They found that the photoluminescence (PL) radiative lifetime increases first with increasing temperature and then decreases at high temperatures. In fact, Marcinkevičius and Leon[12] reported that the PL decay time of InAs QDs decreases monotonously with increasing temperature. These contradicting experimental results could be related to the different sample qualities. To investigate the intrinsic radiative lifetime of excitons in QDs at high temperatures, two important issues should be taken into account. First, the influence of the nonradiative recombination on the surface and in the substrate should be suppressed, which can be realized by growing AlAs confining layers around the QDs and their barriers. Second, the amount of defects in and around the QDs themselves should be minimized, which strongly depends on the growth temperature, the deposition amount, and the quality of the barrier layers. In this letter, we investigate the temperature dependence of the PL decay time in high-quality small Stranski–Krastanow-grown InGaAs/GaAs QDs. We find that the PL decay time increases monotonously with increasing temperature when the temperature is above 80 K and reaches a value of 5.5 ns at 300 K.

The sample was grown with a molecular beam epitaxy instrument on a (001)-oriented undoped GaAs substrate. The layout of the structure is as follows: GaAs substrate/500 nm GaAs/8 nm AlAs/80 nm GaAs/InGaAs QDs/20 nm GaAs/8 nm AlAs/20 nm GaAs Cap layer. The QDs were formed by depositing 5 monolayers (MLs) of $In_{0.5}Ga_{0.5}As$ at 500 °C. The details of the growth conditions and basic characterization of this sample can be found in Refs. 13 and 14. Transmission electron microscopy observation shows that the QDs are half-lens shaped with the lateral base of 5–8 nm and the height of around 2 nm. The area density of QDs is about 3×10^{11} cm^{-2}.

The power-dependent continuous-wave PL was excited via a Ti-sapphire laser with tunable wavelength. Shown in Fig. 1 is the PL spectrum measured at 10 K with the excitation wavelength of 790 nm. The focus spot is about 50 μm in diameter. At the excitation power of 0.02 mW, the PL spectrum is characterized by a peak located at 1.326 eV, with a full width at half maximum of 38 meV. As the excitation power increases from 0.02 to 36 mW, the low-energy transi-

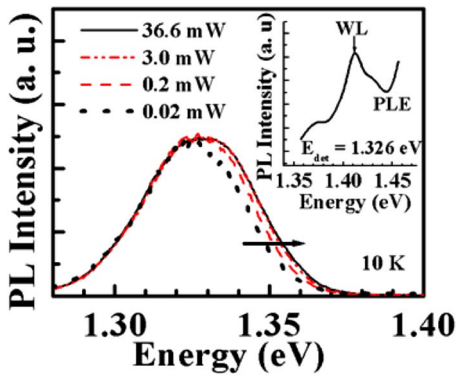

FIG. 1. (Color online) Continuous-wave PL spectra at different excitation powers. The maximum PL intensity is normalized for comparison. The inset shows the PLE spectrum.

a)Electronic mail: zcxu@nankai.edu.cn.

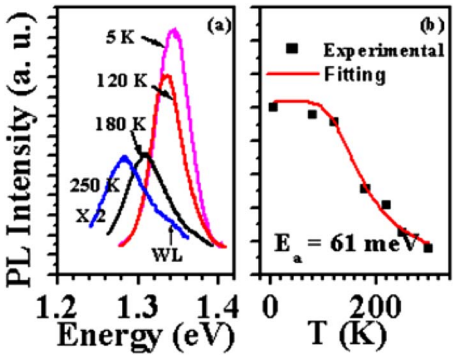

FIG. 2. (Color online) (a) PL spectra at different temperatures; (b) PL peak intensity vs temperature.

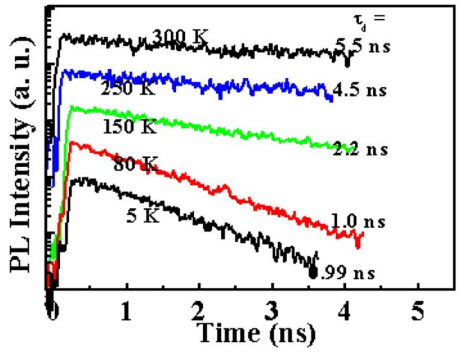

FIG. 3. (Color online) Time decay of PL detected at the peak energies at different temperatures.

tions saturate, while transitions at higher energy are activated, leading to a blueshift of the peak position. This is similar to what is previously observed in high-quality small InAs/GaAs QDs.[15] The high-energy tail at high excitation power results from an excited state transition involving ground state confined electrons and the two-dimensional hole continuum associated with the wetting layer (WL). The inset of Fig. 1 shows the PL excitation (PLE) spectrum with the detection energy of 1.326 eV. The peak at 1.41 eV is attributed to the electron to heavy-hole transitions of the WL. Note that the continuum background below the WL bandgap can be clearly seen. These sub-WL transitions could be related to the WL morphology and/or the coupling of the QDs with their surroundings and are believed to be responsible for the efficient carrier relaxation in self-assembled QDs.[16–20] The upconversion PL from the GaAs barrier layer can even be observed at room temperature when pumping in the continuum background region (not shown here), indicating the high crystal quality of the QD heterostructure.

The time-resolved PL was excited by a femtosecond Ti-sapphire laser with a pulse width of 120 fs and a repetition rate of 76 MHz at the wavelength of 800 nm. The PL signal was dispersed with a monochromator and detected with a streak camera. The overall time resolution of the system is 2.5 ps. The sample temperature can be tuned from 5 to 300 K in a helium cryostat. The excitation power is kept to be 4 mW. The time-integrated PL spectra at different temperatures are shown in Fig. 2(a). The peak intensity of the QD emission is plotted as a function of temperature in Fig. 2(b). The thermal activation energy E_a is determined to be 61 meV by fitting the experimental data with the formula $I(T)=I_0/[1+C\exp(-E_a/k_BT)]$, where $I(T)$ and I_0 are the intensities at temperatures T and 0 K, respectively. Clearly, the observed activation energy is much smaller than the energy difference between the QD peak energy and the WL bandgap, indicating that the drop of QD PL intensity at high temperatures cannot simply be ascribed to the thermal emission of carriers from QDs to the WL. Actually, not only the thermal emission of carriers from the QDs but also the carrier capture by the defects in the barrier matrix before capturing to the QDs, and the thermal population of the optically inactive states can lead to the drop of the PL intensity.

The time decays of the quantum-dot PL detected at the peak energies for different temperatures from 5 to 300 K are shown in Fig. 2. The change in the PL decay time as a function of the temperature is depicted in Fig. 3. It can be seen that the PL decay time is about 1 ns and constant from 5 to 80 K. As the temperature increases from 80 to 300 K, the PL decay time increases monotonously from 1 to 5.5 ns. Note that a decrease in the PL decay time at 300 K has been widely reported in the literature.[9–12,21–23] The observation of long PL decay times, even at 300 K, indicates a high quality of our QD sample. The two AlAs layers can suppress the influence of nonradiative centers on the surface and in the substrate. In addition, the high growth temperature and the small deposition amount facilitate the formation of defect-free QDs.

The thermal population of the higher exciton states, which are optically inactive or have lower oscillator strength, accounts for the prolonged net radiative recombination lifetime in the higher temperature region.[6–8] The radiative recombination rate $\Gamma_R(T)$ at temperature T is given by $\Gamma_R(T)=\Gamma_R(0)/[1+g\exp(-\Delta E/k_BT)]$, where ΔE is the energy difference between the ground state of the QD and some optically inactive excited states and g is the ratio between the degeneracy of the optically inactive states to that of the ground state. The total recombination rate of the QD ground state is given by[11]

$$\Gamma_{\mathrm{rec}}(T)=\frac{1}{\tau_{\mathrm{decay}}}=\Gamma_R(T)+\Gamma_{\mathrm{NR}}(T). \quad (1)$$

Here, τ_{decay} is the measured PL decay time. Γ_{NR} is the nonradiative recombination rate associated with carriers escaping out of the QDs and is given by $\Gamma_{\mathrm{NR}}=\Gamma_0\exp(-\delta/k_BT)$, where δ is the activation energy for thermal carrier escape and Γ_0 is an escape attempt frequency. The parameters in Eq. (1) can be determined to be $\Gamma_R(0)=1.0\times10^{-3}$ ps^{-1}, $g=27$, $\Delta E=36$ meV, and $\Gamma_0=7.0\times10^{-5}$ ps^{-1}, according to the nonlinear least-squares fitting of the experimental data in Fig. 3. The fitting result does not strongly depend on the value of δ. The radiative recombination rate is two orders of magnitude larger than the nonradiative recombination rate. Therefore, the measured PL decay time is dominated by the radiative recombination even at room temperature. The large value of 27 for the g factor (much larger than that determined in Ref. 11) rules out the possibility that the optically inactive states are related to the first excited hole states. The energy difference $\Delta E=36$ meV suggests that the optically inactive states are located in the continuum background determined in the PL spectrum. The values of ΔE and E_a are not the same because E_a contains more information on the complex mechanisms of the carrier loss in the QD heterostructure. For comparison, the typical data for small InAs or InGaAs QDs from Refs. 9, 10, and 23 are also fitted by using formula (1),

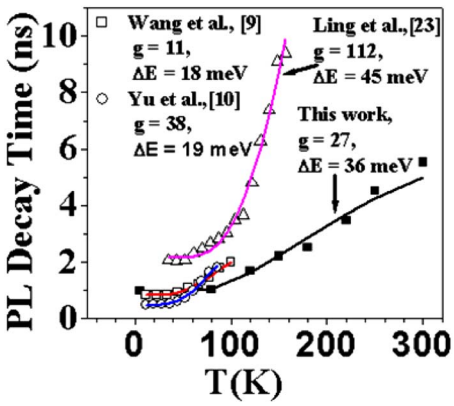

FIG. 4. (Color online) The PL decay times of InGaAs/GaAs QDs vs temperature (closed squares). Open symbols represent data from the literature. The solid lines show the fitting results. The fitting parameters are given in the figure.

as shown in Fig. 4. Note that the values of g ranges from 11 to 112. Therefore, the value of $g=27$ in our QD sample is reasonable.

It is widely believed that the sub-WL continuum background plays an important role in the carrier relaxation in self-assembled QDs.[16–20] The photoexcited carriers in the barrier are captured into the QD ground state through a continuum background relaxation.[19,20] The increase in the PL decay time of the QD ground state transition due to the feeding of carriers into the sub-WL states at high excitation levels and low temperatures has recently been reported.[19] As proposed by Vasanelli *et al.*,[17] the sub-WL continuum transition results from the intrinsic crossed transitions between the bound QD states and the delocalized states. Therefore, the sub-WL continuum transitions should have lower oscillation strength but higher degeneracy, compared with the QD ground state transitions. At high temperatures, the continuum states are thermally populated and behave like carrier reservoirs. Consequently, the PL decay time will be longer if the effect of the nonradiative recombination on the surface and in the substrate is suppressed enough.

In summary, the temperature dependent PL decay time in high-quality small InGaAs/GaAs QDs was investigated by using time-resolved PL experiments. We have observed that the PL decay time of the QD ground states increases with the increase in temperature from 80 to 300 K, and the increase is ascribed to the thermal population of the sub-WL continuum states. As the intrinsic radiative lifetime is at least as long as the observed PL decay time, our observation gives one of the fundamental reasons for the low modal gain of the QD ground states in single-layer self-assembled QD lasers.

This work has been supported by the National Natural Science Foundation of China (Grant Nos. and 60506013 and 10774078) and the Program for New Century Excellent Talents in Universities of China (Grant No. NCET-06-0213). Professor Jingjun Xu, Zhanguo Wang, Professor Wei Lu, and Professor Xiaoshuang Chen are acknowledged for their sincere help.

[1] D. Bimberg, M. Grundmann, and N. N. Ledentsov, *Quantum Dot Heterostructures* (Wiley, New York, 1998).
[2] L. V. Asryan, M. Grundmann, N. N. Ledentsov, O. Stier, R. A. Suris, and D. Bimberg, J. Appl. Phys. **90**, 1666 (2001).
[3] M. V. Maximov, Yu. M. Shernyakov, A. F. Tsatsul'nikov, A. V. Lunev, A. V. Sakharov, V. M. Ustinov, A. Yu. Egorov, A. E. Zhukov, A. R. Kovsh, P. S. Kop'ev, L. V. Asryan, Zh. I. Alferov, N. N. Ledentsov, D. Bimberg, A. O. Kosogov, and P. Werner, J. Appl. Phys. **83**, 5561 (1998).
[4] Z. C. Xu, D. Birkedal, M. Juhl, and J. M. Hvam, Appl. Phys. Lett. **85**, 3259 (2004).
[5] Z. C. Xu, Y. T. Zhang, A. Tackeuchi, Y. Horikoshi, and J. M. Hvam, Appl. Phys. Lett. **92**, 063103 (2008).
[6] D. Citrin, Superlattices Microstruct. **13**, 303 (1993).
[7] H. Gotoh, H. Ando, and T. Kakagahara, J. Appl. Phys. **81**, 1785 (1997).
[8] G. Pistone, S. Savasta, O. Di Stefano, R. Girlanda, and S. Portolan, Phys. Status Solidi B **245**, 1067 (2008).
[9] G. Wang, S. Fafard, D. Leonard, J. E. Bowers, J. L. Merz, and P. M. Petroff, Appl. Phys. Lett. **64**, 2815 (1994).
[10] H. P. Yu, S. Lycett, C. Roberts, and R. Murray, Appl. Phys. Lett. **69**, 4087 (1996).
[11] M. Gurioli, A. Vinattieri, M. Zamfirescu, and M. Colocci, Phys. Rev. B **73**, 085302 (2006), and the references therein.
[12] S. Marcinkevičius and R. Leon, Phys. Rev. B **59**, 4630 (1999).
[13] Z. C. Xu, Y. T. Zhang, and J. M. Hvam, Nanotechnology **18**, 325401 (2007).
[14] Z. C. Xu, K. Leosson, D. Birkedal, J. M. Hvam, J. Sadowski, Z. Y. Zhao, X. S. Chen, Y. M. Liu, and K. T. Yang, J. Cryst. Growth **251**, 177 (2003).
[15] H. Lee, W. D. Yang, and P. C. Sercel, Phys. Rev. B **55**, 9757 (1997).
[16] Y. Toda, O. Moriwaki, M. Nishioka, and Y. Arakawa, Phys. Rev. Lett. **82**, 4114 (1999).
[17] A. Vasanelli, R. Ferreira, and G. Bastard, Phys. Rev. Lett. **89**, 216804 (2002).
[18] E. W. Bogaart, J. E. M. Haverkort, T. Mano, T. van Lippen, R. Nötzel, and J. H. Wolter, Phys. Rev. B **72**, 195301 (2005).
[19] Yu. I. Mazur, B. L. Liang, Zh. M. Wang, D. Guzun, G. J. Salamo, G. G. Tarasov, and Z. Ya. Zhuchenko, J. Appl. Phys. **100**, 054316 (2006).
[20] G. Rainò, G. Visimberga, A. Salhi, M. De Vittorio, A. Passaseo, R. Cingolani, and M. De Giorgi, Appl. Phys. Lett. **90**, 111907 (2007).
[21] A. Fiore, P. Borri, W. Langbein, J. M. Hvam, U. Oesterle, R. Houdré, R. P. Stanley, and M. Ilegems, Appl. Phys. Lett. **76**, 3430 (2000).
[22] M. Paillard, X. Marie, E. Vanelle, T. Amand, V. K. Kalevich, A. R. Kovsh, A. E. Zhukov, and V. M. Ustinov, Appl. Phys. Lett. **76**, 76 (2000).
[23] L. M. Kong, Z. C. Feng, Z. Y. Wu, and W. J. Lu, Semicond. Sci. Technol. **23**, 075044 (2008).

Fast photorefractive response and high sensitivity of Zr and Fe codoped $LiNbO_3$ crystals

Yongfa Kong,[a] Shengqing Wu, Shiguo Liu, Shaolin Chen, and Jingjun Xu
The MOE Key Laboratory of Weak-Light Nonlinear Photonics, Nankai University, Tianjin 300457, People's Republic of China

(Received 25 March 2008; accepted 5 June 2008; published online 24 June 2008)

A series of Zr and Fe codoped $LiNbO_3$ crystals was grown and their photorefractive properties have been investigated. Compared with $LiNbO_3$:Fe,Hf, the concentration of Fe^{2+} ions is strongly increased in $LiNbO_3$:Fe,Zr. As a result, the photorefractive response speed of these as-grown $LiNbO_3$:Fe,Zr crystals is only 2 s and the sensitivity is larger than 12 cm/J while the saturation diffraction efficiency still remains at a high level. These findings prove that $LiNbO_3$:Fe,Zr is an excellent choice for volume holographic storage. © *2008 American Institute of Physics*. [DOI: 10.1063/1.2952275]

Because of its good electro-optic, acousto-optic, elasto-optic, piezoelectric, pyroelectric, and nonlinear properties, lithium niobate ($LiNbO_3$, LN) is one of the most important synthetic crystals. Laser-induced optical damage (also named photorefraction) was discovered in LN and $LiTaO_3$ crystals.[1] This effect can be utilized as holographic storage, laser physics, information processing, and calculation. It was reported that photorefraction can be enhanced by transition-metal ions, such as Fe, Cu, Mn, Ni, etc.,[2,3] and among them, iron doped LN (LN:Fe) crystals have been widely used in holographic volume storage nowadays because of high diffractive efficiencies, high data storage density, and long dark storage time. However, still several shortcomings, such as low response speed and strong light-induced scattering, impede the real application of LN:Fe crystal in holographic volume storage. On the other hand, laser-induced optical damage of congruent LN can greatly be improved by optical damage resistant additives, such as Mg, Zn, In, Sc, and Hf,[4–8] as soon as the doping concentration exceeds a certain threshold. LN crystals doped with optical damage resistant elements have high resistance against light-induced scattering and fast response speed for concentrations above threshold, as has, e.g., been demonstrated by Zhang *et al.* for LN:Fe,Mg.[9]

The main mechanism of this phenomenon is that above the doping threshold, a part of the Fe^{2+} and all of the Fe^{3+} ions are repelled from Li sites to Nb sites, which causes an abrupt decrease of the capture cross section of electrons by Fe^{3+}, and as a consequence, a sharp increase of photoconductivity and therefore a fast response speed. Nevertheless the decrease of $Fe^{2+/3+}$ ions in Li sites will cause an apparent decrease of the diffraction efficiency.[10] Recently, Li *et al.* have reported that Fe ions still remain at Li sites in LN:Fe,Hf crystals when the Hf-doping concentration goes above its threshold value. As a result, response speed and sensitivity are greatly improved while the saturation diffraction efficiency remains at a high value.[11] Therefore the authors considered hafnium ions to be the most efficient one among the optical damage-resistant ions to improve the photorefractive properties of LN:Fe crystals. Last year, we proved that Zr doped LN has much higher resistance against optical damage in comparison to LN:Mg and LN:Hf.[12] Because Zr^{4+}, just like Hf^{4+} ion are both tetravalent ion with higher valence than that of $Fe^{2+/3+}$, we expect that Zr codoped LN:Fe crystal will have excellent photorefractive properties.

The objective of this letter is to investigate the holographic properties of LN:Fe codoped with Zr (LN:Fe,Zr). We will show that LN:Fe,Zr crystals not only maintain relatively high diffraction efficiencies, but also have much shorter response times and better photorefractive sensitivities than LN:Fe,Hf crystals. These results make LN:Fe,Zr crystals the better choice for holographic volume storage.

In our experiments, a series of LN:Fe,Zr crystals were grown along the *c* axis with the conventional Czochralski method. The [Li]/[Nb] composition was selected as 48.38/51.62, 0.03 wt % Fe_2O_3 and 1, 2, 3, 4, and 5 mol % ZrO_2 were codoped in to the melt, and were labeled as LN:Fe,Zr_1, LN:Fe,Zr_2, LN:Fe,Zr_3, LN:Fe,Zr_4, and LN:Fe,Zr_5, respectively. After annealing treatment and artificial polarization, these crystals were cut to 1 and 3 mm plates along the *y* faces and optically polished for characterization of optical absorption and photorefraction.

The holographic properties were investigated by two-wave mixing in transmission geometry at a fixed grating spacing. A diode-pumped frequency-doubled Nd:YAG (yttrium aluminum garnet) laser operating at 532 nm was used with an intensity of 250 mW/cm^2. Two mutually coherent and extraordinary polarized beams irradiated these 3 mm thick plates with a crossing angle of 23°. The grating vector was aligned along the *c* axis to utilize the largest electro-optic coefficient r_{33}. The measured diffraction efficiency η was defined as $I_d/(I_d+I_t)$, where I_d and I_t are the diffracted and transmitted intensity of the readout beam, respectively. The recording time constant τ_r and the saturation diffraction efficiency η_{sat} were described by the function of $\eta(t) = \eta_{sat}[1-\exp(-t/\tau_r)]$, while the photorefractive sensitivity S was defined as $S=(d\sqrt{\eta}/dt)_{t=0}/(IL)$, where I is the total recording light intensity and L is the crystal thickness.

Table I shows the photorefractive properties of LN:Fe,Zr crystals. The data for LN:Fe, LN:Mg,Fe, and LN:Fe,Hf crystals are also listed for comparison.[9,11] We can see from Table I that the response time of LN:Fe is as long as 160 s. However, for LN:Mg,Fe crystals, the response time shortens to 60 s when 2 mol % MgO was codoped and to just 15 s as MgO concentration exceeds its doping threshold. The re-

[a]Electronic mail: kongyf@nankai.edu.cn.

TABLE I. Photorefractive properties of LN:Fe,Zr crystals. Incident light intensity of a single beam was approximately 250 mW/cm. The data for LN:Fe, LN:Mg,Fe, and LN:Fe,Hf crystals were also listed for comparison (Refs. 9 and 11).

	Doping concentrations				Photorefractive properties			
Sample	Fe (wt %)	Mg (mol %)	Hf (mol %)	Zr (mol %)	η_{sat}(%)	τ_r (s)	S (cm/J)	σ_{ph} (Ω^{-1} cm^{-1})
LN:Fe	0.01				70	160		
LN:Fe,Mg_2	0.01	2			70	60		
LN:Fe,Mg_6	0.01	6			15	15		
LN:Fe,Hf_2	0.03		2		68.0	17.2	3.99	1.31×10^{-13}
LN:Fe,Hf_5	0.03		5		55.4	10.7	5.23	1.78×10^{-13}
LN:Fe,Zr_1	0.03			1	25.5	2.2	13.46	2.52×10^{-12}
LN:Fe,Zr_2	0.03			2	32.0	1.8	12.87	2.91×10^{-12}
LN:Fe,Zr_3	0.03			3	32.7	1.8	13.48	2.72×10^{-12}
LN:Fe,Zr_4	0.03			4	32.5	1.8	13.40	3.10×10^{-12}
LN:Fe,Zr_5	0.03			5	42.2	2.2	12.61	3.04×10^{-12}

sponse time for LN:Fe,Hf crystals is in a range from 10 to 17 s. However, for LN:Fe,Zr crystals, the response time decreases to only 2 s! Table I also indicates that as the doping concentration of MgO exceeds the threshold, the diffraction efficiency of LN:Fe,Mg decreases to only about one fifth of that of LN:Fe. However, for LN:Fe,Hf crystals, the diffraction efficiency does not show such large differences for HfO_2 concentration below and above its doping threshold. The situation of LN:Fe,Zr is just like that of LN:Fe,Hf though the value of diffraction efficiency for the former is smaller than that of the later. However, because the response time of LN:Fe,Zr is much smaller than that of LN:Fe,Hf, the photorefractive sensitivity of the former is more than two times higher than that of the later.

The above experimental results show that LN:Fe,Zr has more than five times shorter photorefractive response time, more than two times larger photorefractive sensitivity, and about 2/3 photorefractive of the diffraction efficiency of that of LN:Fe,Hf. Since we know that Zr and Hf all exist in LN crystal as tetravalent ions, there arises the basic question: what induces these differences? To find an answer, we calculate the photoconductivity σ_{ph} from the equation:[13] $\ln(\eta/\eta_{max})=2(\sigma_{ph}/\varepsilon)t+\text{constant}$, where ε is the dielectric constant of the material and σ_{ph} follows from the slope of the line $\ln(\eta/\eta_{max})\sim 2t/\varepsilon$. Experimental results on σ_{ph} for LN:Fe,Hf and LN:Fe,Zr crystals are listed in Table I. We can see from this table that the photoconductivity of LN:Fe,Zr is one order of magnitude larger than that of LN:Fe,Hf, which can give us a phenomenological explanation why the photorefractive response time of LN:Fe,Zr is much shorter than that of LN:Fe,Hf. However, what is the micromechanism underneath?

The OH^- absorption spectra and UV-visible absorption spectra of LN:Fe,Zr crystals were investigated with 1 mm thick plates, and measured by a Magna-560 Fourier transform infrared spectrophotometer and a Beckman DU-8B spectrophotometer, respectively, with the incident light transmitting along the y axis at room temperatures. Figure 1 shows the OH^- absorption spectra of LN:Fe,Zr crystals, where the curves from top to bottom are for 1, 2, 3, 4, and 5 mol % ZrO_2, respectively. It is known that when the doping concentration of MgO exceeds the threshold in LN:Fe,Mg, there exists a 3507 cm^{-1} peak corresponding to the vibration of $Fe^{3+}_{Nb}-OH^-$,[14,15] which means Fe^{3+} ions move from Li sites to Nb sites and causes an abrupt decrease of its capture cross section for electrons. Therefore, the photoconductivity has a sharp increase and thus strongly reduces the light-induced refractive index in LN:Fe,Mg. However, in Fig. 1, there is no 3507 cm^{-1} absorption peak even if we decompose these bands with a three-peaks model. This suggests that the lattice locations of Fe^{3+} ions are still at Li sites when the doping concentration of ZrO_2 goes above its threshold.

Figure 2 shows the UV-visible absorption spectra of LN:Fe,Zr and LN:Fe,Hf crystals, where A, B, C, D, and E are for 1, 2, 3, 4, and 5 mol % Zr, and X and Y are for 2 and 5 mol % Hf, respectively. We can see from this figure that LN:Fe,Zr crystals have deeper absorption in the visible range than LN:Fe,Hf crystals. The broad absorption band from the absorption edge to 700 nm corresponds to the electron transition from Fe^{2+} to Nb^{5+}.[16] It was reported that the concentrations of Fe^{2+} irons ($C_{Fe^{2+}}$) can be deduced from the absorption at 476 nm.[17] The distribution coefficient of Fe is nearly one, therefore the concentration of Fe^{3+} ions ($C_{Fe^{3+}}$) can be obtained by $C_{Fe}-C_{Fe^{2+}}$, where C_{Fe} is the total iron doping content. The calculated results for LN:Fe,Zr and

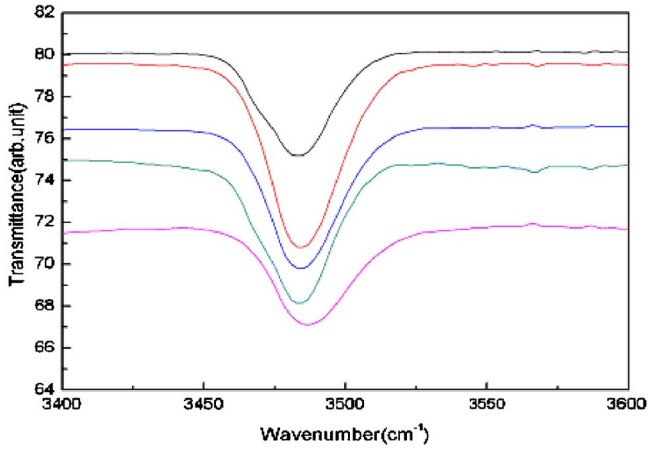

FIG. 1. (Color online) OH^- absorption spectra of LN crystals codoped with 0.03 wt % Fe and different concentrations of Zr. The curves from top to bottom are for 1, 2, 3, 4, and 5 mol % Zr, respectively.

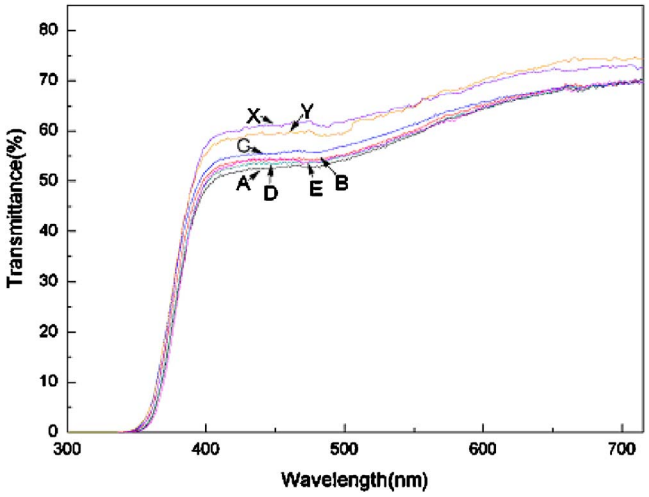

FIG. 2. (Color online) Transmittance curves for LN crystals codoped with 0.03% Fe_2O_3 and different concentrations of ZrO_2. A, B, C, D, and E are for 1, 2, 3, 4, and 5 mol % Zr, and X and Y are for 2 and 5 mol % Hf, respectively.

LN:Fe,Hf crystals were collected in Table II. From this table, we can easily see that the concentration of Fe^{2+} ions in LN:Fe,Zr crystals is apparently larger than that of LN:Fe,Hf and the Fe^{2+}/Fe^{3+} ratio of the former is several times higher than that of latter, which suggests that LN:Fe,Zr crystals have larger photoconduction, faster photorefractive response speed and higher sensitivity than LN:Fe,Hf crystals.

It surprises to some extent that the photorefractive properties of LN:Fe,Zr have not shown much difference for concentrations of ZrO_2 below and above its doping threshold. In fact, from Table I, we can also see a similar phenomenon for LN:Fe,Hf crystals though it is not so obvious. It is known that the main photorefractive centers are $Fe^{2+/3+}$ ions in LN:Fe crystals. As to LN:Fe,Mg crystals when the concentration of MgO exceeded its doping threshold, Fe^{3+} ions will be pushed to Nb sites from Li site, which causes abrupt decreases of photorefractive diffraction efficiency and response time. However, for LN:Fe,Hf and LN:Fe,Zr crystals, the site occupation of $Fe^{2+/3+}$ ions does not change as the doping concentrations exceed thresholds, so the response times decrease gradually. Below doping threshold, the response time should decrease with decreasing content of intrinsic defects as the doping concentrations increases, and since there are different types of intrinsic defects that are related with photorefraction, detailed experiments are needed to exactly describe this process. Especially for the LN:Fe,Zr crystals of this study, because the doping threshold is between 1.7 and 2.0 mol %,[12] the doping concentration of ZrO_2 in $LN:Fe,Zr_1$ is closer to the threshold than that for $LN:Fe,Hf_2$, where the doping threshold of HfO_2 is about 4 mol %, which causes the relative change of the response time between $LN:Fe,Zr_1$ and $LN:Fe,Zr_2$ being smaller than that between $LN:Fe,Hf_2$ and $LN:Fe,Zr_5$.

TABLE II. The concentration of Fe^{2+} and the ratio of Fe^{2+}/Fe^{3} in LN:Fe,Zr and LN:Fe,Hf crystals.

Sample	$C_{Fe^{2+}}$ (10^{24} cm^{-3})	$C_{Fe^{2+}}/C_{Fe^{3+}}$
$LN:Fe,Hf_2$	5.53	0.358
$LN:Fe,Hf_5$	6.72	0.457
$LN:Fe,Zr_1$	9.89	1.570
$LN:Fe,Zr_2$	8.82	1.197
$LN:Fe,Zr_3$	7.94	0.962
$LN:Fe,Zr_4$	8.76	1.179
$LN:Fe,Zr_5$	9.16	1.303

In summary, a series LN:Fe,Zr crystals with different doping concentrations of ZrO_2 have been grown, and photorefractive properties and UV-visible-infrared absorption spectra were investigated. As compared with LN:Fe,Mg, $Fe^{2+/3+}$ ions still occupy Li sites as photorefractive centers in LN:Fe,Zr when the concentration of ZrO_2 exceeds the doping threshold. It is interesting that although Zr^{4+} and Hf^{4+} are all tetravalent ions, the concentration of Fe^{2+} ions in as-grown LN:Fe,Zr is much higher than that in LN:Fe,Hf. Therefore, these LN:Fe,Zr crystals have greatly enhanced photorefractive response speed and sensitivity while keeping still a relatively high diffraction efficiency. Our experimental results indicate that zirconium ions are a preferable choice to improve the photorefractive properties of LN:Fe crystal.

This work was financially supported by Chinese National Key Basic Research Special Fund (No. 2006CB921703), National Basic Research Program of China (No. 2007CB307002), Program for Changjiang Scholars and Innovative Research Team in University, and National Natural Science Foundation of China (60578019). The authors hope to greatly thank the referee for his valuable comments. One of the authors, (Y. K.), wants to express his appreciation to Professor Romano Rupp (Vienna University) for his helpful discussion.

[1] A. Askin, G. D. Boyd, J. M. Dziedzic, R. G. Smith, A. A. Ballman, J. J. Levinstein, and K. Nassau, Appl. Phys. Lett. **9**, 72 (1966).
[2] W. Phillips, J. J. Amodei, and D. L. Staebler, RCA Rev. **33**, 94 (1972).
[3] D. K. McMillen, T. D. Hudson, J. Wagner, and J. Singleton, Opt. Express **2**, 291 (1998).
[4] G. Zhong, J. Jin, and Z. Wu, in *Proceedings of the 11th International Quantum Electronics Conference*, IEEE Cat. No. 80 CH1561–0 (IEEE, New York, 1980), p. 631.
[5] T. R. Volk, V. J. Pryalkin, and M. M. Rubinina, Opt. Lett. **15**, 996 (1990).
[6] J. K. Yamamoto, K. Kitamura, N. Iyi, S. Kimura, Y. Furukawa, and M. Sato, Appl. Phys. Lett. **61**, 2156 (1992).
[7] Y. Kong, J. Wen, and H. Wang, Appl. Phys. Lett. **66**, 280 (1995).
[8] E. P. Kokanyan, L. Razzari, I. Cristiani, V. Degiorgio, and J. B. Gruber, Appl. Phys. Lett. **84**, 1880 (2004).
[9] G. Zhang, J. Xu, S. Liu, Q. Sun, G. Zhang, Q. Fang, and C. Ma, Proc. SPIE **14**, 2529 (1995).
[10] S. Chen, H. Liu, Y. Kong, Z. Huang, and J. Xu, Cryst. Res. Technol. **41**, 790 (2006).
[11] S. Li, S. Liu, Y. Kong, J. Xu, and G. Zhang, Appl. Phys. Lett. **89**, 101126 (2006).
[12] Y. Kong, S. Liu, Y. Zhao, H. Liu, S. Chen, and J. Xu, Appl. Phys. Lett. **91**, 081908 (2007).
[13] M. Bienvenu, D. Woodbury, and T. Robson, J. Appl. Phys. **51**, 4245 (1980).
[14] L. Kovács, Z. Szaller, I. Cravero, I. Földvari, and C. Zaldo, J. Phys. Chem. Solids **51**, 417 (1990).
[15] Y. Kong, J. Xu, W. Zhang, and G. Zhang, J. Phys. Chem. Solids **61**, 1331 (2000).
[16] O. Schirmer, O. Thiemann, and M. Wöhlecke, J. Phys. Chem. Solids **52**, 185 (1991).
[17] H. Kurz and E. Kraitzig, Appl. Phys. **12**, 355 (1977).

Compact high power broadband $Er^{3+}-Yb^{3+}$-codoped superfluorescent fiber source

Feng Song,[a] Zhenzhou Cheng, Changguang Zou, Lin Han, Xiaochen Yu, Jiaxiang Zhang, Xueping Jiang, Peize Han, and Jianguo Tian
Photonics Center, College of Physics Science, Nankai University, Tianjin 300071, People's Republic of China

(Received 15 April 2008; accepted 31 July 2008; published online 3 September 2008)

Compact high power broadband superfluorescent fiber source has been demonstrated using an ultrashort $Er^{3+}-Yb^{3+}$-codoped phosphate glass fiber. The fiber is 10.4-cm-long and at 1.68 W pump power, an output power of 16.85 mW, a mean wavelength of 1540.9 nm, a bandwidth of 18.4 nm, and a slope efficiency of 18.6% have been obtained. The dependence of output power, mean wavelength, and bandwidth stability on pump power and fiber length are also studied, and there is an excellent agreement between the theoretical results and experimental data. © *2008 American Institute of Physics*. [DOI: 10.1063/1.2976664]

Superfluorescent fiber source (SFS) has attracted much research interest,[1–3] due to its distinct advantages, such as high spatial coherence, broad spectral emission, and excellent long-term stability of the mean wavelength, and has been investigated widely.[4–7] Usually, the SFS comprises of a single-mode silica fiber, which length is typically 1–50 m. Such long length is not practical for packaging with integrated optical components because spooling the long length of fiber affects the size, the complexity, and the cost. Nonlinear effects in fiber will be aggravated with the increasing active fiber length in the light source. Common SFS using silica glass fiber limits the bandwidth (BW) of the emission spectra. A shorter length of active fiber in SFS is therefore desirable and will overcome the above shortcomings. In recent years, many studies have been carried out using short length of high gain fiber, and several groups have demonstrated compact fiber amplifier and laser devices but not SFS (Refs. 8–12) because it is difficult to provide sufficient gain and curb simultaneously with laser emission in an ultrashort high gain fiber. Hence, despite its potential applications the investigation of SFS with short length high gain fiber has received less attention.

In this letter, we report both theoretical and experimental results on an ultrashort double-pass forward (DPF) pumped high-concentration $Er^{3+}-Yb^{3+}$-codoped phosphate glass fiber (EYDPF) suitable as SFS. Dependence of the output power, the SFS mean wavelength, and the BW on the launched pump power and the fiber length are analyzed in details. Superfluorescence is generated from an active fiber with only 10.4 cm in length.

High-concentration EYDPF has been demonstrated to provide sufficient gain per centimeter in achieving high power in an ultrashort length,[12] due to the distinct advantages of material.[13–15] The theories and performances of high concentration $Er^{3+}-Yb^{3+}$-codoped phosphate glass have been reported previously.[16,17] In our experiments, Er^{3+} ions and Yb^{3+} ions were incorporated uniformly in the core region of the fiber with concentrations of ~1 and ~8 wt %, respectively. The fiber has a numerical aperture of 0.214 and a 5 μm core diameter, and is single mode at 1.5 μm wavelength. The off-center core fibers, which are employed in our experiments, can enhance the pump absorption efficiency due to the chaotic propagation of the pump light.[18]

Considering the system complexity and the conversion efficiency, DPF pumping configuration is preferred as the ideal choice.[19] Each fiber end was cleaved at a small angle ($>7°$), which can diminish the light fed back by Fresnel reflection; hence the amplified spontaneous emission (ASE) propagates only once through the fiber and lasing can be suppressed effectively. Coupling lens was used to focus the pump light into the fiber through a dielectric mirror (M), and the mirror was attached to the input end of the active fiber. The M has a reflectivity R_1 of ≈100% at 1540 nm wavelength and a $R_2<6\%$ at 976 nm pump wavelength. The fiber was end pumped by a high-power 976 nm wavelength semiconductor laser diode (LD) source (Apollo Instruments S20-976-1). To reduce the instability caused by the pump wavelength variations, there was a temperature controlling setup for the LD in our experiments. A power meter and an optical spectrum analyzer (OSA) (Advantest Q8384) were used to measure the output power and the spectrum, respectively. The room temperature was controlled by an airconditioner in our experiments. No attempt was made to control the EYDPF's temperature.

The relationship between the superfluorescence output power and launched pump power is shown in Fig. 1. A maximum output power of 16.85 mW was measured experimen-

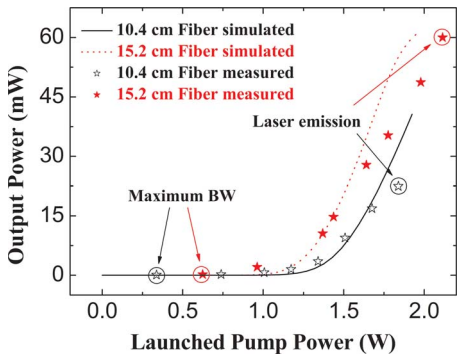

FIG. 1. (Color online) Output power vs launched pump power for $Er^{3+}-Yb^{3+}$-codoped SFS.

[a]Electronic mail: fsong@nankai.edu.cn. FAX: +86-22-2350-159.

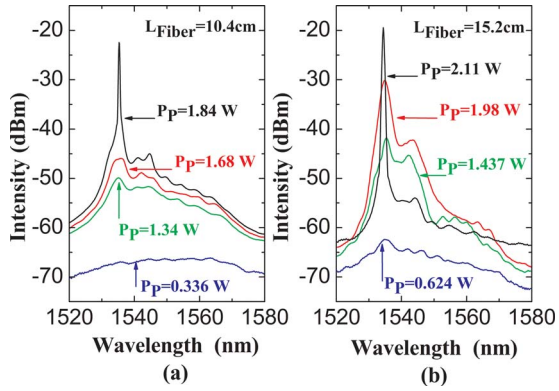

FIG. 2. (Color online) Emission spectra at different launched pump powers. (a) Emission spectra using a 10.4-cm-long fiber. (b) Emission spectra using a 15.2-cm-long fiber.

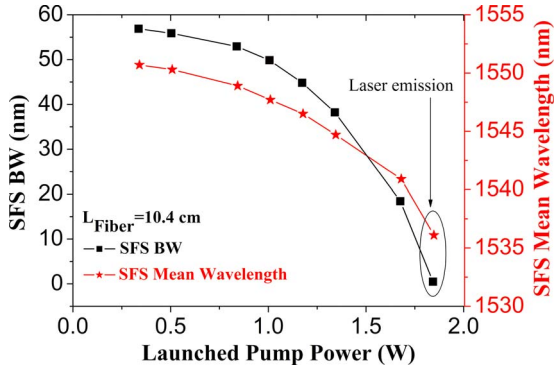

FIG. 3. (Color online) BW and mean wavelength of SFS vs launched pump power with a 10.4-cm-long fiber.

tally from a 10.4-cm-long fiber. The output power increases almost linearly with launched pump power above the threshold. The slope efficiency is 18.6% with respect to the absorbed power. We calculate the performances of the SFS based on the propagation and the rate equations model.[20] The solid line in Fig. 1 represents the calculated results with DPF configuration. The evolution of the pump power and the ASE powers with longitudinal fiber coordinate z is governed by the power propagation equations.[20] The propagation equations used a 40 nm output BW, which is represented by ten wavelength regions, so each simulating power is produced in a 4 nm BW. Using the fiber parameters and the coupling efficiency measured, the calculated results agree well with the experimental data. The results of a 15.2-cm-long fiber are also shown in Fig. 1. A maximum superfluorescence power of 45.85 mW can be obtained using a launched power of 1.98 W.

The emission spectra at different launched pump powers are shown in Fig. 2. From Fig. 2(a), we can see that the threshold launched pump power for the 10.4-cm-long fiber is 0.336 W, and the SFS reaches a maximum output power with a launched pump power of 1.68 W. As expected, the spectral profile varies when the pump power increases from 0.336 to 1.68 W. The peak wavelength of the emission band is 1535.8 nm with a BW (3 dB) of 5.7 nm (from 1532.5 to 1538.2 nm) at the launched pump power of 1.68 W. The light emitted from the fiber is the fundamental mode because a single mode fiber is used. Further increase in the launched pump power leads to lasing as confirmed by the presence of a sharp peak in the output spectrum, as shown in Fig. 2. It is the residual feedback from the fiber-end facets that results to the onset of lasing. The superfluorescent spectra of a 15.2 cm EYDPF were also recorded, as shown in Fig. 2(b).

In our experiment the spectra were divided into 501 discrete points by the OSA. The mean wavelength[21] and emission BW (Ref. 19) were calculated, respectively.

Generally, the mean wavelength of SFS depends on many parameters; however, it is difficult to stabilize all parameters.[22,23] In our research, we tried to reduce the influence of LD by controlling its temperature. We controlled the LD's temperature to ± 0.1 °C, which corresponds to the pump wavelength variations of ± 0.03 nm. According to theoretical simulation, the dependence of mean wavelength on pump wavelength in our experiments was calculated to be $\partial\bar{\lambda}/\partial\lambda_p = 0.0017$, so the mean wavelength fluctuation caused by LD was ± 0.033 ppm. Thus SFS mean wavelength variations due to LD's temperature can be neglected.[22] Moreover, we fixed launched pump power at 1.3 W, and the room temperature was changed between 20.2 and 23 °C over 5 h. According to linear fit to mean wavelengths under different room temperatures, the intrinsic thermal effect of SFS under experimental temperature was estimated to be −8.44 ppm/°C.

The dependence of mean wavelength and BW on pump power was shown in Fig. 3. For the 10.4-cm-long fiber, when the pump power increases from 0.336 to 1.68 W, the mean wavelength decreases by 9.8 nm and changes from 1550.7 to 1540.9 nm. The shift towards shorter wavelength as pump power increases is due to the strengthening of the 1535 nm emission that dominates the spectrum, as shown in Fig. 2. The increase in pump power produces a decrease in mean wavelength with a slope of −7.19 ppm/mW. Since room temperature was kept relatively constant (± 0.2 °C) during a short period of measuring, the dependence of mean wavelength on pump power (less than 5 min) and the mean wavelength variations caused by SFS experimental temperature were about ± 1.7 ppm. The maximum BW measured is 56.9 nm. When the launched pump power is increased to a value just before lasing occurs, the BW narrows monotonously to a value of 18.4 nm.

For comparison, the mean wavelength and the BW characteristics for a 15.2-cm-long fiber are also measured and calculated. Within the superfluorescence output range, the total change of the mean wavelength is 8.4 nm and the slope is -6.04 ± 1.7 ppm/mW. The maximum BW is 29.3 nm at the threshold launched pump power and decreases to 5.1 nm with a maximum output power of 45.85 mW.

In our experiments, the mean wavelength remained within 24 ppm and room temperature was in the range of 2.8 °C over the 5 h of the test. So the average drift of mean wavelength is about −8.57 ppm/°C, which agrees with the linear fit and is in the range of reported values.[22,23] However, the fluctuation of mean wavelength always exited, even under the same room temperature. We speculate that fluctuation mainly comes from temperature disruption around the active fiber and the energy transfer mechanism in this material. To improve the stability, further researches are undergoing.

In summary, we demonstrate the operation of a compact broadband high-concentration $Er^{3+}-Yb^{3+}$-codoped phosphate glass SFS by employing the conventional DPF configuration. The shortest fiber, which can generate considerable superfluorescence, is 10.4 cm in length. From this fiber

we obtain an output power of 16.85 mW, a mean wavelength of 1540.9 nm, a BW of 18.4 nm, and a slope efficiency of 18.6% using a launched pump power of 1.68 W.

This work was supported by National Science Foundation of China (NSFC) (Grant No. 60778038); we appreciate Professor Edwin Y.B. Pun in City University of Hong Kong for revising the manuscript.

[1]S.-P. Chen, Z.-J. Liu, Y.-G. Li, K.-C. Lu, and S.-H. Zhou, Opt. Express **16**, 207 (2008).
[2]P. Wang, J. K. Sahu, and W. A. Clarkson, IEEE J. Sel. Top. Quantum Electron. **13**, 580 (2007).
[3]P. Wang, J. K. Sahu, and W. A. Clarkson, Opt. Lett. **31**, 3116 (2006).
[4]Y. C. Yan, A. J. Faber, H. de Waal, P. G. Kik, and A. Polman, Appl. Phys. Lett. **71**, 2922 (1997).
[5]S. C. Tsai, T. C. Tsai, P. C. Law, and Y. K. Chen, IEEE Photon. Technol. Lett. **15**, 197 (2003).
[6]S. P. Chen, Y. G. Li, J. P. Zhu, H. Wang, Y. Zhang, T. W. Xu, R. Guo, and K. C. Lu, Opt. Express **13**, 1531 (2005).
[7]W. Huang, X. Wang, B. Zheng, H. Xu, C. Ye, and Z. Cai, Opt. Express **15**, 9778 (2007).
[8]J. Limpert, N. Deguil-Robin, I. Manek-Hönninger, F. Salin, F. Röser, A. Liem, T. Schreiber, S. Nolte, H. Zellmer, A. Tünnermann, J. Broeng, A. Petersson, and C. Jakobsen, Opt. Express **13**, 1055 (2005).
[9]M. Laroche, A. M. Chardon, J. Nilsson, D. P. Shepherd, W. A. Clarkson, S. Girard, and R. Moncorgé, Opt. Lett. **27**, 1980 (2002).
[10]Y. Hu, S. Jiang, T. Luo, K. Seneschal, M. Morrell, F. Smektala, S. Honkanen, J. Lucas, and N. Peyghambarian, IEEE Photon. Technol. Lett. **13**, 657 (2001).
[11]B. C. Hwang, S. Jiang, T. Luo, K. Seneschal, G. Sorbello, M. Morrell, F. Smektala, S. Honkanen, J. Lucas, and N. Peyghambarian, IEEE Photon. Technol. Lett. **13**, 197 (2001).
[12]L. Li, M. Morrell, T. Qiu, V. L. Temyanko, A. Schülzgen, A. Mafi, D. Kouznetsov, J. V. Moloney, T. Luo, S. Jiang, and N. Peyghambarian, Appl. Phys. Lett. **85**, 2721 (2004).
[13]R. Wu, J. D. Myers, M. J. Myers, and C. Rapp, Proc. SPIE **4968**, 1 (2003).
[14]W. H. Wong, E. Y. B. Pun, and K. S. Chan, Appl. Phys. Lett. **84**, 176 (2004).
[15]B. Hwang, S. Jiang, T. Luo, J. Watson, G. Sorbello, and N. Peyghambarian, J. Opt. Soc. Am. B **17**, 833 (2000).
[16]F. Song, M. J. Myers, S. Jiang, Y. Feng, X. B. Chen, and G. Y. Zhang, Proc. SPIE **3622**, 182 (1999).
[17]F. Song, G. Y. Zhang, M. R. Shang, H. Tan, J. Yang, and F. Meng, Appl. Phys. Lett. **79**, 1748 (2001).
[18]V. Doya, O. Legrand, and F. Mortessagne, Opt. Lett. **26**, 872 (2001).
[19]L. Shi, S. Zhao, W. Meng, Y. Li, S. Zhan, and R. Zhu, Opt. Commun. **257**, 270 (2006).
[20]D. T. Nguyen, A. Chavez-Pirson, S. Jiang, and N. Peyghambarian, IEEE J. Quantum Electron. **43**, 1018 (2007).
[21]W. Huang, X. Wang, Z. Cai, H. Xu, and C. Ye, J. Opt. **7**, 179 (2005).
[22]H. G. Park, M. Digonnet, and G. Kino, J. Lightwave Technol. **21**, 3427 (2003).
[23]P. F. Wysocki, M. J. F. Digonnet, B. Y. Kim, and H. J. Shaw, J. Lightwave Technol. **12**, 550 (1994).

Band-Gap Engineering and Light Manipulation with Egg-Crate Photonic Lattices

Peng Zhang, Cibo Lou, Sheng Liu, Fajun Xiao, Jianlin Zhao, Jingjun Xu and Zhigang Chen

Light propagation in periodic structures offers new opportunities to control the flow of light.[1] Much of the previous research was based on optically induced photonic lattices, an ideal platform for exploring discretizing light behaviors.[2] We have shown that a new type of photonic lattice can be established in nonconventionally biased (NCB) photorefractive crystals.[3-5] This enables the reconfiguration of desired photonic structures and Brillouin zones (BZs) for bandgap engineering and light manipulation. Some examples include bandgap closure and Bragg reflection suppression, soliton transition between bandgaps, and the interplay between normal and anomalous diffraction/refraction under identical excitation conditions.[4,5]

With an anisotropic photorefractive model,[3] we have theoretically investigated nonlinear beam propagation in both homogeneous and periodic media under the NCB condition. We found that a self-focusing and self-defocusing nonlinearity can exist simultaneously in the same material, depending solely on the orientation of the probe beam; this is remarkably different from the conventional bias condition.[2] This "hybrid nonlinearity" enables a transition between discrete and gap solitons without the need of bias reversal, as observed in our experiment.[4]

In addition, under the NCB condition, the enhanced anisotropy and nonlocality lead to unusual index structures for reshaping soliton beams. For example, an elliptical discrete soliton can be created experimentally with its ellipticity and orientation controlled by reconfiguring the lattice structures without changing the soliton beam itself.[4]

More interesting phenomena occur even in the linear regime. Photonic lattice structures and their corresponding BZs can be reconfigured at ease by adjusting the relative orientation of the bias field and the crystalline *c*-axis. Obviously, the location of index maxima, the shape of lattice sites, and even the period of the induced lattices can be varied dramatically. Of particular interest are egg-crate lattices, where both periodic positive and negative index changes are induced in the same material. Such lattices resemble ionic crystal lattices with alternating positive and negative charges, which should lead to novel wave transmission properties compared to conventional lattices.[2]

One example is the closing of a bandgap and thus suppressing or stopping the Bragg reflection in a particular direction. As seen from the BZ spectra in the figure, some lines of the BZs are "missing" due to alternating positive and negative index changes in a row corresponding to that k-space direction, suggesting a new approach for bandgap engineering. The same probe beam experiences no Bragg reflection in the vertical direction in lattice (a) but strong reflection in lattice (d). Another surprising outcome for such lattice reconfiguration is that the first BZ for lattice (c) happens to be overlapping with the 2nd BZs for other lattices, enabling another host of new phenomena such as transitions between Bloch modes associated with different high-symmetry points, between normal and anomalous diffraction, and between positive and negative refraction by the same probe beam excitation.[5]

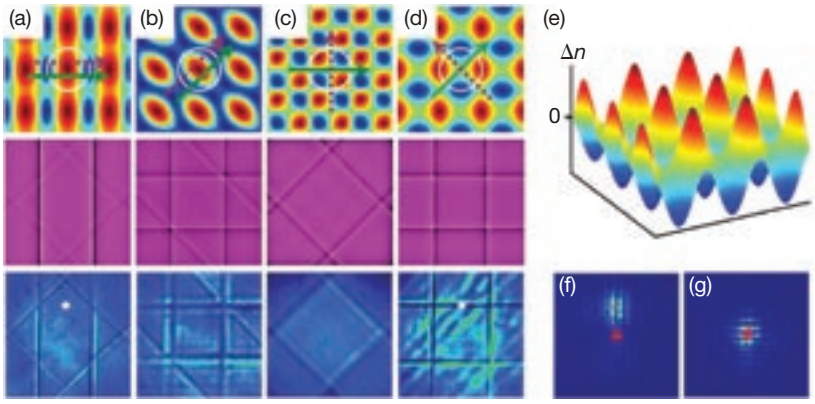

(a-d) Calculated refractive index profiles (first row) and corresponding BZ spectra from simulation (second row) and experiment (third row) for lattice structures optically induced by an identical beam under different bias conditions, where the center of the white circle indicates one of the intensity maxima of the optical beam and the dashed and solid arrows show the directions of the c-axis and bias field, respectively. (e) 3D display of index pattern of (d) a typical egg-crate lattice structure. (f, g) Observed output patterns of a tilted probe beam with its excitation location in k-space marked by a white dot in (a, d), respectively, showing tunneling (f) and Bragg-reflection (g) in lattices. The red cross in (f, g) indicates the input position of the probe beam.

This work was supported by the NPU Foundation for Fundamental Research, the Doctorate Foundation of NPU, the 973 program, 111 project, NSFC, PCSIRT, NSF and AFOSR.

P. Zhang, S. Liu, F. Xiao and J. Zhao are with Shaanxi Key Laboratory of Optical Information Technology, School of Science, Northwestern Polytechnical University, Xi'an, China. C. Lou, J. Xu and Z. Chen (zchen@stars.sfsu.edu) are with The Key Laboratory of Weak-Light Nonlinear Photonics, Ministry of Education and TEDA Applied Physics School, Nankai University, Tianjin, China. Z. Chen is also with the department of physics and astronomy, San Francisco State University, Calif., U.S.A.

References

1. D.N. Christodoulides et al. Nature **424**, 817 (2003).
2. N.K. Efremidis et al. Phys. Rev. E **66**, 046602 (2002); J. W. Fleischer et al. Nature **422**, 147 (2003).
3. P. Zhang et al. Opt. Express **15**, 536 (2007).
4. P. Zhang et al. Opt. Lett. **33**, 878 (2008); Opt. Express **16**, 3865 (2008).
5. P. Zhang et al. submitted to Phys. Rev. Lett. (2008).

Defect-Free Surface Waves

Ivan L. Garanovich, Alexander Szameit, Andrey A. Sukhorukov, Stefan Nolte, Thomas Pertsch, Andreas Tünnermann and Yuri S. Kivshar

Interfaces between physical media can support a special type of localized mode known as surface waves. In solids, electronic surface waves generated in crystals at the edge of truncated periodic potential are commonly explained as the manifestation of either Tamm[1] or Shockley[2] localization mechanisms. Optical analogs of Tamm and Shockley states have also been studied extensively in different types of periodic photonic structures, where such optical surface waves are particularly attractive for optical sensing, measurement and characterization applications. Usually, a surface defect is required for surface waves to exist in straight photonic lattices composed of identical waveguides. Discrete optical surface solitons have been recently observed in nonlinear arrays, where such a defect is induced due to nonlinearity.[3]

Recently, we revealed that boundaries of modulated photonic lattices can support a new type of surface wave without any introduced or induced surface defects.[4] In a lattice composed of identical straight waveguides, surface waves cannot exist and light always experiences strong repulsion from the surface and diffraction. In contrast, we predicted that, in a modulated lattice composed of waveguides with periodically curved axes, well-localized linear surface modes can exist, despite the fact that all the waveguides are still identical, and there are no defects.[4]

The appearance of these novel surface modes is a result of nontrivial modification of the diffraction properties in the vicinity of the lattice edge, which is introduced by the lattice modulation, and is completely different from the diffraction management studied previously in infinite lattices. We developed a general analytical theory of such novel surface modes, demonstrating their unique properties, which are distinct from both Tamm and Shockley surface waves.[4]

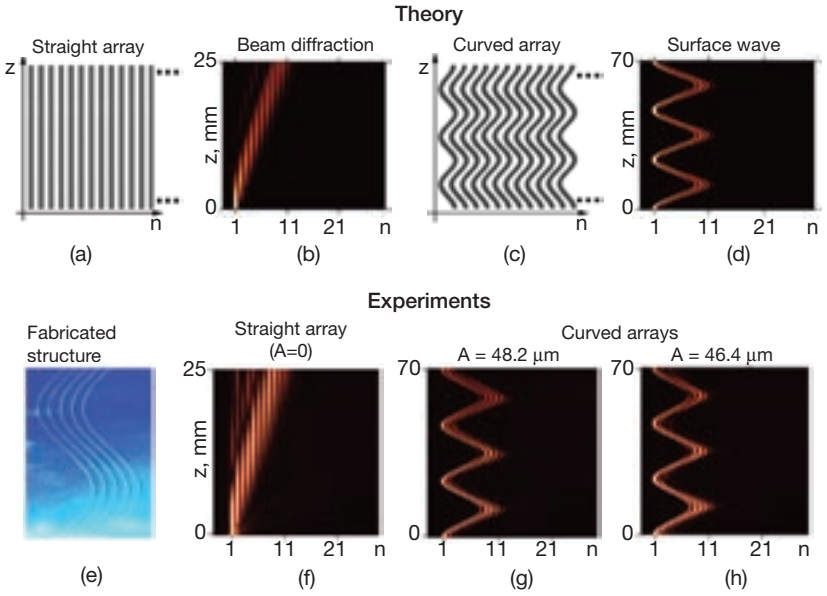

Theoretical prediction (top) and experimental observation (bottom) of defect-free linear surface states in modulated semi-infinite photonic lattices. In (a) straight lattices without surface defects, beam always experiences (b) repulsion form the surface and diffraction. In contrast, we predict that in (c) modulated lattices, (d) a new type of surface wave is possible. (e) Microscope image of the fabricated curved array and (f-h) fluorescent images of beam propagation in arrays with different modulation amplitude A.

We have also observed such defect-free surface waves experimentally.[5] We used the femtosecond laser direct-writing technique to create periodically curved waveguide arrays in silica glass samples. A special type of silica with high OH content was used, resulting in the formation of fluorescent color centers during the writing process. This makes it possible to measure fluorescence by launching into array light from a HeNe laser at 633 nm, and to directly visualize the beam propagation. Since the color centers are formed exclusively inside the arrays, a high signal-to-noise ratio is obtained. We confirmed the absence of any surface defects in our samples, and then studied the generation of surface waves in curved waveguide arrays. We showed that the degree of surface wave localization can be controlled by selecting the waveguide bending amplitude (g,h).

The ability to generate these novel surface waves in optics can aid the development of tools for studying of various surface phenomena. Similar effects can also occur for other types of modulated lattices in different physical systems.

I.L. Garanovich (ilg124@rsphysse.anu.edu.au), A.A. Sukhorukov and Yu.S. Kivshar are with CUDOS at the Australian National University, Canberra, Australia. A. Szameit, S. Nolte, T. Pertsch and A. Tünnermann are with Friedrich-Schiller-University, Jena, Germany.

References

1. I.E. Tamm. Z. Phys. **76**, 849 (1932).
2. W. Shockley. Phys. Rev. **56**, 317 (1939).
3. S. Suntsov et al. Phys. Rev. Lett. **96**, 063901 (2006).
4. I.L. Garanovich et al. Phys. Rev. Lett. **100**, 203904 (2008).
5. A. Szameit et al. Phys. Rev. Lett. (in press).

Evolutions of polarization and nonlinearities in an isotropic nonlinear medium

Zhi-Bo Liu, Xiao-Qing Yan, Wen-Yuan Zhou, and Jian-Guo Tian*

The Key Laboratory of Weak Light Nonlinear Photonics, Ministry of Education, Teda Applied Physics School, Nankai University, Tianjin 300457, China
Corresponding author: jjtian@nankai.edu.cn

Abstract: The evolutions of polarization and nonlinearities in an isotropic medium induced by anisotropy of third-order nonlinear susceptibility were studied experimentally and theoretically. The anisotropy of imaginary part of third-order susceptibility was verified to exist by the change of ellipticity of polarization ellipse in the isotropic nonlinear medium CS_2. The changes of nonlinear refraction and nonlinear absorption depending upon the ellipticity of polarization ellipse are also presented. The numerical simulations based on two coupled nonlinear Schrödinger equations (NLSE) provide an excellent quantitative agreement with experimental results.

OCIS codes: (190.0190) Nonlinear optics; (190.4400) Nonlinear optics, materials; (190.3270) Kerr effect; (190.4180) Multiphoton processes.

References and links

1. P. D. Maker, R. W. Terhune, and C. M. Savage, "Intensity-dependent changes in the refractive index of liquids," Phys. Rev. Lett. **12**, 507-509 (1964).
2. P. D. Maker and R. W. Terhune, "Study of optical effects due to an induced polarization third order in the electric field strength," Phys. Rev. **137**, A801-818 (1965).
3. P. X. Nguyen and G. Rivoire, "Evolution of the polarization state of an intense electromagnetic field in a nonlinear medium," Opt. Acta. **25**, 233-246 (1978).
4. P. X. Nguyen, J. L. Ferrier, J. Gazengel, and G. Rivoire, "Polarization of picosecond light pulses in nonlinear isotropic media," Opt. Commun. **46**, 329-333 (1983).
5. A. J. van Wonderen, "Influence of transverse effect on self-induced polarization changes in an isotropic Kerr medium," J. Opt. Soc. Am. B **14**, 1118-1130 (1997).
6. M. Lefkir and G. Rivoire, "Influence of transverse effects on measurement of third-order nonlinear susceptibility by self-induced polarization state changes," J. Opt. Soc. Am. B **14**, 2856-2864 (1997).
7. M. V. Tratnik and J. E. Sipe, "Nonlinear polarization dynamics. I. The single-pulse equations," Phys. Rev. A **35**, 2965-2975 (1987).
8. D. David, D. D. Holm, and M. V. Tratnik, "Hamiltonian chaos in nonlinear optical polarization dynamics," Phys. Rep. 187, 281-367 (1990).
9. A. L. Gaeta and R. W. Boyd, "Transverse instabilities in the polarizations and intensities of counterpropagating light waves," Phys. Rev. A **48**, 1610-1624 (1993).
10. M. Delqué, G. Fanjoux, and T. Sylvestre, "Polarization dynamics of the fundamental vector soliton of isotropic Kerr media," Phys. Rev. E **75**, 016611 (2007).
11. M. Delqué, T. Sylvestre, H. Maillotte, C. Cambournac, P. Kockaert, and M. Haelterman, "Experimental observation of the elliptically polarized fundamental vector soliton of isotropic Kerr media," Opt. Lett. **30**, 3383-3385 (2005).
12. C. Cambournac, T. Sylvestre, H. Maillotte, B. Vanderlinden, P. Kockaert, Ph. Emplit, and M. Haelterman, "Symmetry-Breaking Instability of Multimode Vector Solitons," Phys. Rev. Lett. **89**, 083901 (2002).
13. R. DeSalvo, M. Sheik-Bahae, A. A. Said, D. J. Hagan, and E. W. Van Stryland, "Z-scan measurements of anisotropy of nonlinear refraction and absorption in crystals," Opt. Lett. **18**, 194-196 (1993).
14. Sean J. Wagner, J. Meier, A. S. Helmy, J. Stewart Aitchison, M. Sorel, and D. C. Hutchings, "Polarization-dependent nonlinear refraction and two-photon absorption in GaAs/AlAs superlattice waveguides below the half-bandgap," J. Opt. Soc. Am. B **24**, 1557-1563 (2007).
15. Z. B. Liu, Y. L. Liu, B. Zhang, W. Y. Zhou, J. G. Tian, W. P. Zang, and C. P. Zhang, "Nonlinear absorption and optical limiting properties of carbon disulfide in short-wavelength region," J. Opt. Soc. Am. B **24**, 1101-1104 (2007).
16. R. W. Boyd, *Nonlinear Optics*, second edition (Academic Press, San Diego, 2003).
17. M. Sheik-Bahae, A. A. Said, T. H. Wei, D. J. Hagan, and E. W. Van Stryland, "Sensitive measurement of optical nonlinearities using a single beam," IEEE J. Quantum Electron **26**, 760-169 (1990).

1. Introduction

Since the pioneering experimental work of Maker, *et al.*, [1], the dynamical evolution of polarization state of light due to the anisotropy of real part of third-order nonlinear susceptibility ($\chi^{(3)} = \chi^{(3)}_{xxyy} + \chi^{(3)}_{xyxy} + \chi^{(3)}_{xyyx}$) has been studied extensively in isotropic media as well as anisotropic media [2-7]. The existence of $\chi^{(3)}_{xyyx}$ can induce a rotation of axis position as a polarization ellipse propagates through the medium. Some nonlinear effects relating to nonlinear polarization rotation, such as bistable, unstable, and chaotic behaviors were realized [8, 9]. A fundamental elliptically polarized vector soliton was also observed in the spatial domain in a CS_2 liquid slab planar waveguide [10-12]. However, reports on the anisotropy of imaginary part of $\chi^{(3)}$ are few. Although several theoretical analyses [3-5] predicted that the anisotropy of imaginary part of $\chi^{(3)}$ can lead to the ellipticity change of an elliptically polarized beam in isotropic media, to the best of our knowledge no experimental observation has supported such a prediction, and most of experimental reports were only involved in anisotropic media [13, 14].

The anisotropy of $\chi^{(3)}$ can lead to dynamical evolution of the polarization state of light, meanwhile, the change of the polarization state also has a drastic effect on third-order susceptibility. However, most of reports on polarization dependent nonlinear refraction and nonlinear absorption were concentrated on anisotropic media [13, 14]. In this letter, we present the anisotropy of imaginary parts of $\chi^{(3)}$ and the ellipticity dependent nonlinear refraction and nonlinear absorption in the isotropic medium CS_2. Like the anisotropy of real part of $\chi^{(3)}$, the anisotropy of imaginary part is very important to the evolution of nonlinear polarization dynamics.

2. Experimental details

Our experimental setup is shown in Fig. 1. A commercial optical parametric oscillator (Continuum Panther Ex OPO) pumped by the third harmonic (355 nm) from Continuum Surelite-II is used to generate 4-5 ns pulses with a repetition rate of 10 Hz and tunable in the range of 420-2500 nm. A Glan prism (G1) was used to generate a linearly polarized light. The elliptic polarization state of the input beam was adjusted by angle (φ) between G1 and a quarter-wave plate. The input beam has nearly Gaussian transverse shape and was focused by a 150 mm focal length lens to form a beam waist of 19 μm. To determine the axis position and *e* of the global polarization state, we directly measured the transmitted energy as the analyzer G2 rotates. The experiment is carried out on the isotropic nonlinear medium CS_2. This molecule has been thoroughly studied in nonlinear ellipse rotation and exhibits a large molecular reorientation nonlinearity. The nonlinear susceptibility tensor of CS_2 at 440 nm, 470 nm, and 532 nm was studied because CS_2 exhibits a large nonlinear absorption at 440 nm and 470 nm in the nanosecond regime [15]. The 5 mm length CS_2 cell was fixed on the focus.

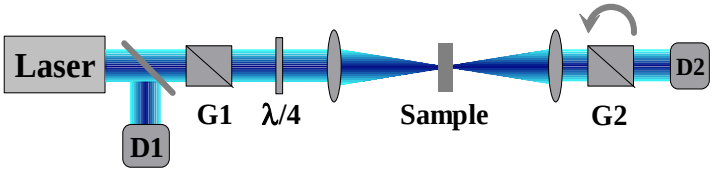

Fig. 1. Schematic of experimental Setup. G1 and G2 are Glan prisms, D1 and D2 are detectors.

3. Results and discussions

Figures 2(a)-2(c) show the experimental normalized transmittance T as a function of orientation of G2 (ϕ) for nonlinear output and linear output at 440 nm, 470 nm, and 532 nm. The values of e of polarization ellipse can be obtained by using the relationship of $e^2=T_{min}/T_{max}$, where T_{min} and T_{max} are the minimum and maximum of transmittance T, respectively. The x-coordinates relative to T_{min} and T_{max} represent the positions of major and minor axis of polarization ellipse. Relative to the case of linear output, an obviously shift of axis position of polarization ellipse in nonlinear output can be observed at these wavelengths, which indicates the existence of the anisotropy of $\mathrm{Re}(\chi^{(3)})$. This is consistent with large molecular reorientation nonlinearity of CS_2 observed in the subnanosecond and nanosecond regimes [16]. The $\mathrm{Re}(\chi^{(3)}_{xyyx})$ mainly contributes to the shift of axis position, i.e., the rotation of polarization ellipse. Additionally, the change of T_{max} is much larger than that of T_{min} as shown in Figs. 2(a) and 2(b) at 440 nm and 470 nm. Therefore, the ellipticity e changes as an elliptical polarized beam propagates through the medium, and nonlinear absorption is anisotropic due to $\mathrm{Im}(\chi^{(3)}_{xyyx})\neq 0$.

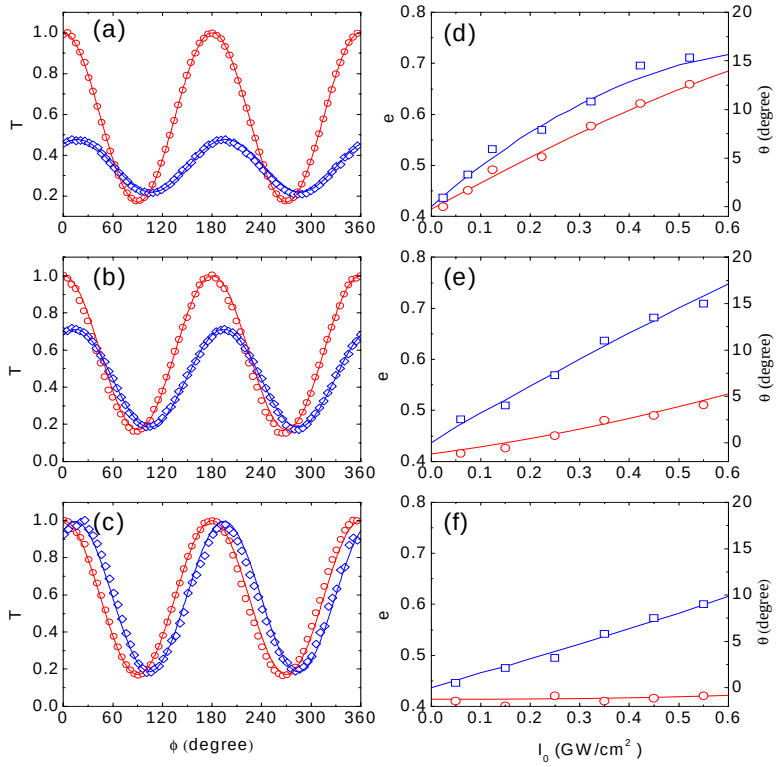

Fig. 2. Experimental and theoretical results: (a), (b), (c): transmittance for nonlinear output (open diamonds) and linear output (open circles) at 440 nm, 470 nm, and 532 nm, respectively. (d), (e), (f): the ellipticity e (open circles) and the rotation angle θ (open squares) as a function of input intensity I_0 at 440 nm, 470 nm and 532 nm. The solid lines are theoretical simulations with Re(A)=13, 8, 3.5×10^{-20} m^2/V^2, Im(A)=7, 2.5, 0×10^{-20} m^2/V^2, Re(B)=27, 20, 14×10^{-20} m^2/V^2, and Im(B)=19, 6, 0×10^{-20} m^2/V^2 for 440nm, 470nm, and 532nm, respectively.

To picture the evolutions of polarization state more clearly, the ellipticity e and the rotation angle θ as a function of input intensity I_0 at 440 nm, 470 nm and 532 nm are given in Figs. 2(d), 2(e), and 2(f), respectively. Rotation angle θ increases with I_0 at these wavelengths

due to $\mathrm{Re}(\chi^{(3)}_{xyyx}) \neq 0$. At 440 nm and 470 nm, the value of e also increases with I_0, and the slope of curve $\theta(I_0)$ at 440 nm is larger than that at 470 nm. However, the value of e almost keeps unchanged at 532 nm since CS_2 has no obvious nonlinear absorption. The increasing e with I_0 further verifies the existence of the anisotropy of $\mathrm{Im}(\chi^{(3)})$ of CS_2 at 440 nm and 470 nm.

To model the evolutions of polarization and nonlinearities as an elliptically polarized beam propagates in a nonlinear medium, the following coupled NLSEs are employed:

$$\frac{1}{r}\frac{\partial}{\partial r}\left(r\frac{\partial E_+}{\partial r}\right) - 2ik\frac{\partial E_+}{\partial z} + \frac{4\pi k^2}{n_0^2}\left[A|E_+|^2 + (A+B)|E_-|^2\right]E_+ = 0, \quad (1)$$

$$\frac{1}{r}\frac{\partial}{\partial r}\left(r\frac{\partial E_-}{\partial r}\right) - 2ik\frac{\partial E_-}{\partial z} + \frac{4\pi k^2}{n_0^2}\left[A|E_-|^2 + (A+B)|E_+|^2\right]E_- = 0, \quad (2)$$

where r is the radial coordinate, z is the longitudinal coordinate, n_0 is the linear refractive index, $k=2\pi n_0/\lambda$ is the wave vector and λ is the wavelength. E_+, E_- are the left- and right-hand circularly polarized components of the electric field. Following the notation of nonlinear polarization of Maker, *et al*., [1], the effective nonlinear susceptibilities of two circular components can be written as [16]:

$$\chi^{(NL)}_{\pm} = A|E_{\pm}|^2 + (A+B)|E_{\mp}|^2, \quad (3)$$

where $A = 3\chi^{(3)}_{xyxy} + 3\chi^{(3)}_{xxyy}$, $B = 6\chi^{(3)}_{xyyx}$. The solid lines in Fig. 2 are the results of numerical simulations using Eqs. (1) and (2). The parameters used in the simulations are Re(A)=13, 8, 3.5×10^{-20} m^2/V^2, , Im(A)=7, 2.5, 0×10^{-20} m^2/V^2, Re(B)=27, 20, 14×10^{-20} m^2/V^2, and Im(B)=19, 6, 0×10^{-20} m^2/V^2 at 440 nm, 470 nm, and 532 nm, respectively. The total third-order nonlinear susceptibility $|\chi^{(3)}|$ ($\chi^{(3)} = A/3 + B/6$) are 10.1, 6.3, and 3.5×10^{-20} m^2/V^2 at 440 nm, 470 nm, and 532 nm, respectively. The value of $|\chi^{(3)}|$ at 532 nm agrees well with that in previous report [17].

As mentioned above, nonlinear susceptibility component B induces the evolution of ellipticity and axis position of polarization ellipse. Meanwhile, different polarization state also affects the change of nonlinear refraction and nonlinear absorption [18]. Using the relationship between the dielectric constant ε and nonlinear susceptibility $\chi^{(NL)}$ with $\varepsilon = \varepsilon_0 + 4\pi\chi^{(NL)}$, where ε_0 is the linear dielectric constant, we can write the differences in refractive index ($\Delta n_{\pm}$) and absorption ($\Delta\alpha_{\pm}$) due to nonlinear reaction as follows:

$$\Delta n_{\pm} = \frac{2\pi}{n_0}\mathrm{Re}\left[A|E_{\pm}|^2 + (A+B)|E_{\mp}|^2\right], \quad (4)$$

$$\Delta\alpha_{\pm} = \frac{4\pi k}{n_0}\mathrm{Im}\left[A|E_{\pm}|^2 + (A+B)|E_{\mp}|^2\right]. \quad (5)$$

Note that the differences of refraction and absorption depend upon only the coefficient B but not the coefficient A.

Be different from anisotropic medium, the changes of nonlinear refraction and absorption in an isotropic medium are dependent on only the ellipticity of polarization ellipse, but not the polarization orientation. First, for circularly polarized light with e=1, only one of two circular components is present, and the changes in refractive index and absorption can be given by $\Delta n = 2\pi/n_0\,\mathrm{Re}(A)|E|^2$, and $\Delta\alpha = 4\pi k/n_0\,\mathrm{Im}(A)|E|^2$. Second, for linearly polarized light with e=0, we can see that the changes of refractive index and absorption can be given by $\Delta n = 2\pi/n_0\,\mathrm{Re}(A+B/2)|E|^2$, and $\Delta\alpha = 4\pi k/n_0\,\mathrm{Im}(A+B/2)|E|^2$, since linearly polarized light is a combination of equal amounts of left-and right-hand circular components (i.e. $|E_+|^2 = |E_-|^2$),

where E denotes the total field amplitude of the linearly polarized radiation with $|E|^2 = 2|E_+|^2 = 2|E_-|^2$.

Open and closed aperture Z-scan [17] experiments were carried out to determine the ellipticity dependent nonlinear refraction and absorption. The experimental results at 440 nm are shown in Fig. 3. The on-axis intensity I_0 used in our Z-scan experiments is 3.2×10^8 W/cm^2. For a linearly polarized light as a light source in our Z-scan measurements, nonlinear refraction coefficient n_{2lin} and absorption coefficient β_{lin} were determined to be 13.5×10^{-14} cm^2/W and 17.4×10^{-9} cm/W, respectively, which are over one time larger than those of circular polarization with $n_{2cir}=6.1\times10^{-14}$ cm^2/W and $\beta_{cir}=6.5\times10^{-9}$ cm/W. Moreover, from the results of Z-scan with circularly polarized light, one can obtain the value of complex nonlinear susceptibility component A because the changes of refractive index and absorption depend on only A in the case of circular polarization. The real and imaginary parts of A are 13×10^{-20} m^2/V^2 and 8.0×10^{-20} m^2/V^2, respectively. And then, the coefficient B can be determined from the Z-scan experimental results of linear polarization or elliptical polarization, and the values of Re(B) and Im(B) are 24×10^{-20} m^2/V^2 and 18×10^{-20} m^2/V^2 respectively, which agree well with the results obtained from nonlinear polarization experiments shown in Fig. 2.

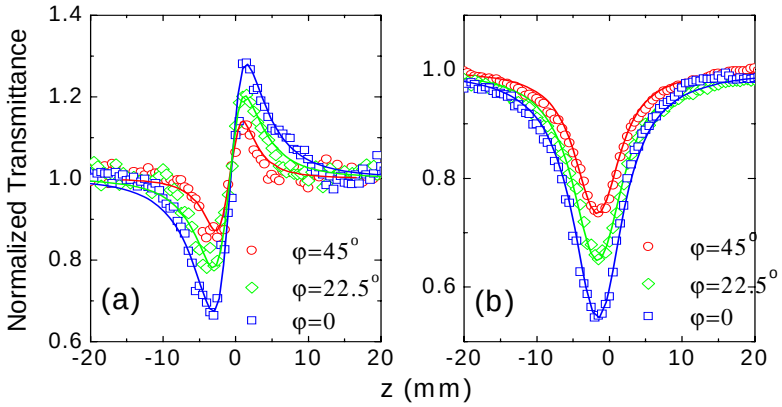

Fig. 3. Z-scan curves of nonlinear refraction and nonlinear absorption in the cases of linearly, elliptical and circular polarized input laser at 440nm. The solid lines are the theoretical fits with $n_{2lin}=13.5\times10^{-14}$ cm^2/W, $n_{2ell}=8.4\times10^{-14}$ cm^2/W, $n_{2cir}=6.1\times10^{-14}$ cm^2/W, and $\beta_{lin}=17.4\times10^{-9}$ cm/W, $\beta_{ell}=9.5\times10^{-9}$ cm/W, $\beta_{cir}=6.5\times10^{-9}$ cm/W.

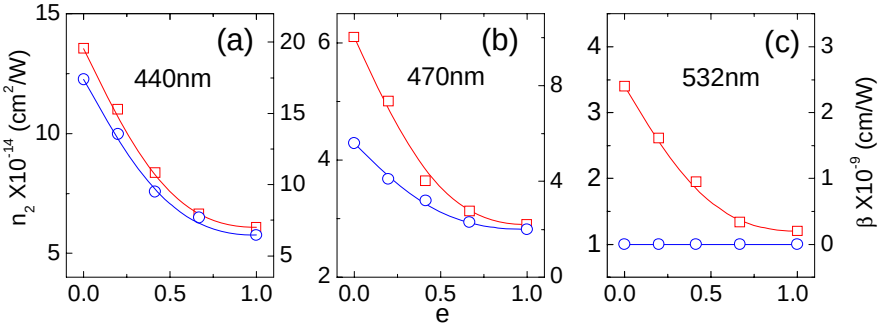

Fig. 4. The n_2 (open squares) and β (open circles) as a function of e at 440nm, 470nm, and 532nm. The solid lines are the theoretical results.

Once n_{2lin} and β_{lin} of linearly polarized light and n_{2cir} and β_{cir} of circularly polarized light are determined, from Eqs. (4) and (5) one can obtain the expressions of n_{2ell} and β_{ell} of elliptical polarized light as a function of ellipticity as follows:

$$n_{2ell} = \frac{(1-q^2)n_{2cir} + 2qn_{2lin}}{1+q^2}, \tag{6}$$

$$\beta_{ell} = \frac{(1-q^2)\beta_{cir} + 2q\beta_{lin}}{1+q^2}, \tag{7}$$

where q=(1-e)/(1+e). The Z-scan curves of nonlinear refraction and absorption with e=0.41 are shown in Fig. 3 and we can get n_{2ell}=8.4×10^{-14} cm^2/W and β_{ell}=9.5×10^{-9} cm/W. Other fitting parameters are the same as those of linearly polarized light. Figure 4 gives experimental and theoretical results of the changes of n_2 and β as a function of e at 440 nm, 470 nm, and 532 nm, respectively. The symbols represent the experimental results, and agree well with the solid lines obtained by theoretical simulations using Eqs. (6) and (7). The change of nonlinearities indicates that nonlinear refraction and nonlinear absorption are tunable by controlling the ellipticity of elliptically polarized beam.

The relative magnitude of A and B depends upon the nature of the physical process of optical nonlinearities. For molecular orientation nonlinearities, the ratio of the real part of B to that of A is 6, this is the case of optical nonlinearities of CS_2 in the nanosecond and picosecond regimes. However, Re(B)/Re(A) and Im(B)/Im(A) obtained in our nanosecond experiments at 440 nm are 2.1 and 2.7, respectively. Re(B)/Re(A)=2.5 and Im(B)/Im(A)=2.4 were obtained at 470 nm, and Re(B)/Re(A)=4 was obtained at 532 nm. The decreasing ratio of B/A indicates that other nonlinear mechanism should exist in the nanosecond regime besides molecular orientation. The origin of the different physical characters of the two contributions (A and B) to nonlinear susceptibility can be understood in terms of the energy level [16]. One-photon-resonant processes contribute only to the coefficient A, while two-photon- resonant processes contribute to both the coefficients A and B. In Ref. [15] we reported that the large nonlinear absorption of CS_2 in a short wavelength region and the nanosecond regime can arise from a combination of two-photon absorption and the excited-state absorption induced by two-photon absorption. Excited state nonlinearity can cause the decrease of B/A since effective third-order nonlinearities are sequential one-photon process and independent upon the change of polarization state.

4. Conclusion

In summary, we present the evolutions of polarization and nonlinearities in an isotropic medium CS_2. In the early sixties, Maker, *et a.,l* planed to simultaneously study the polarization dependence of the intensity-induced absorption and the intensity-induced rotation in order to obtain accurate relative values of Im(A), Re(A), Im(B) and Re(B). In our work the complex third-order susceptibility tensors of CS_2 at 440 nm, 470 nm, and 532 nm were measured. To our knowledge, our results offer the first experimental evidence of Im(B) induced nonlinear polarization dynamics and ellipticity-dependent nonlinearities in an isotropic medium. Further experiments aiming at studying influence of spatial-temporal effects on self-induced polarization changes due to complex third order nonlinear susceptibility are expected to sharpen this analysis. Many interesting extensions are possible, including the tuning of optical limiting, optical switching, and photonic crystal by controlling polarization state.

Acknowledgments

This work is supported by the Natural Science Foundation of China (No. 60708020, 10574075), Chinese National Key Basic Research Special Fund (No. 2006CB921703), and the Program for Changjiang Scholars and Innovative Research Team in University (IRT0149).

Self-trapping of optical vortices in waveguide lattices with a self-defocusing nonlinearity

Daohong Song[1], Cibo Lou[1], Liqin Tang[1], Xiaosheng Wang[2],Wei Li[1], Xingyu Chen[1], Kody J.H. Law[3], Hadi Susanto[3], P. G. Kevrekidis[3], Jingjun Xu[1], and Zhigang Chen[1,2]*

1The Key Laboratory of Weak-Light Nonlinear Photonics, Ministry of Education and TEDA Applied Physical School, Nankai University, Tianjin 300457, China
2Department of Physics and Astronomy, San Francisco State University, San Francisco, California 94132, USA
3Department of Mathematics and Statistics, University of Massachusetts, Amherst, Massachusetts 01003, USA
**Corresponding author: zchen@stars.sfsu.edu*

Abstract: We demonstrate the self-trapping of single- and double-charged optical vortices in waveguide lattices induced with a self-defocusing nonlinearity. Under appropriate conditions, a donut-shaped single-charged vortex evolves into a stable discrete gap vortex soliton, but a double-charged vortex turns into a self-trapped quadrupole-like structure. Spectrum measurement and numerical analysis suggest that the gap vortex soliton does not bifurcate from the edge of the Bloch band, quite different from previously observed gap spatial solitons. Our numerical findings are in good agreement with experimental observations.

OCIS codes: (190.0190) Nonlinear optics; (190.5330) Photorefractive optics; (250.5530) Pulse propagation and temporal solitons

References and links

1. D. N. Christodoulides, F. Lederer, and Y. Silberberg, "Discretetizing light behavior in linear and nonlinear waveguide lattices," Nature **424**, 817 (2003).
2. Y. S. Kivshar and G. P. Agrawal, *Optical Solitons: From Fibers to Photonic Crystals* (Acedemic, San Diego, Calif. 2003).
3. D. N. Christodoulides and R. I. Joseph, "Discrete self-focusing in nonlinear arrays of coupled waveguides," Opt. Lett. **13**, 794 (1988).
4. H. S. Eisenberg, Y. Silberberg, R. Morandotti, A. R. Boyd, and J. S. Aitchison, "Observation of discrete solitons in optical waveguide arrays," Phys. Rev. Lett. **81**, 3383 (1998).
5. J. W. Fleischer, T. Carmon, M. Segev, N. K. Efremidis, and D. N. Christodoulides, "Observation of discrete solitons in optically induced real time waveguide arrays," Phys. Rev. Lett. **90**, 023902 (2003).
6. J. W. Fleischer, M. Segev, N. K. Efremidis, and D. N. Christodoulides, "Observation of two-dimensional discrete solitons in optically induced nonlinear photonic lattices," Nature **422**, 147 (2003).
7. D. Neshev, E. Ostrovskaya, Y. Kivshar, and W. Królikowski, "Spatial solitons in optically induced gratings," Opt. Lett. **28**, 710 (2003).
8. H. Martin, E. D. Eugenieva, Z. Chen, and D. N. Christodoulides, "Discrete solitons and soliton-induced dislocations in partially coherent photonic lattices," Phys. Rev. Lett. **92**, 123902 (2004).
9. D. Mandelik, R. Morandotti, J. S. Aitchison, and Y. Silberberg, "Gap solitons in waveguide arrays," Phys. Rev. Lett. **92**, 093904 (2004).
10. D. Neshev, A. A. Sukhorukov, B. Hanna, W. Krolikowski, and Y. S. Kivshar, "Controlled generation and steering of spatial gap solitons," Phys. Rev. Lett. **93**, 083905 (2004).
11. F. Chen, M. Stepic, C. E. Ruter, D. Runde, D. Kip, V. Shandarov, O. Manela, and M. Segev, "Discrete diffraction and spatial gap solitons in photovoltaic LiNbO3 waveguide arrays," Opt. Express **13**, 4314 (2005).
12. C. Lou, X. Wang, J. Xu, Z. Chen, and J. Yang, "Nonlinear spectum reshaping and gap-soliton-train trapping in optically inducd photonic structures," Phys. Rev. Lett. **98**, 213903 (2007).
13. B. A. Malomed and P. G. Kevrekidis, "Discrete vortex solitons," Phys. Rev. E **64**, 026601 (2001).
14. J. Yang and Z. H. Musslimani, "Fundamental and vortex solitons in a two-dimensional optical lattice," Opt. Lett. **28**, 2094 (2003).
15. D. N. Neshev, T. J. Alexander, E. A. Ostrovskaya, Y. S. Kivshar, H. Martin, I. Makasyuk, Z. Chen, "Observation of discrete vortex solitons in optically-induced photonic lattices," Phys. Rev. Lett. **92**, 123903 (2004).

16. J. W. Fleischer, G. Bartal, O. Cohen, O. Manela, M. Segev, J. Hudock, and D. N. Christodoulides, "Observation of vortex-ring discrete solitons in 2D photonic lattices," Phys. Rev. Lett. **92**, 123904 (2004).
17. G. Bartal, O. Manela, O. Cohen, J. W. Fleicher, and M. Segev, "Observation of second-band vortex solitons in 2D photonic lattices," Phys. Rev. Lett. **95**, 053904 (2005).
18. E. A. Ostrovskaya and Y. S. Kivshar, "Matter-wave gap vortices in optical lattices," Phys. Rev. Lett. **93**, 160405 (2004).
19. P. G. Kevrekidis, H. Susanto, and Z. Chen, "High-order-mode soliton structures in two-dimensional lattices with defocusing nonlinearity," Phys. Rev. E **74**, 066606 (2006).
20. T. Richter and F. Kaiser, "Anisotropic gap vortices in photorefractive media," Phys. Rev. A **76**, 033818 (2007).
21. L. Tang, C. Lou, X. Wang, D. Song, X. Chen, J. Xu, Z. Chen, H. Susanto, K. Law, and P. G. Kevrekidis, "Observation of dipole-like gap solitons in self-defocusing waveguide lattices," Opt. Lett. **32**, 3011 (2007).
22. N. K. Efremidis, S. Sears, D. N. Christodoulides, J. W. Fleischer, and M. Segev," Discrete solitons in photorefractive optically induced photonic lattices," Phys. Rev. E **66**, 046602 (2002).
23. A. Bezryadina, E. Eugenieva, and Z. Chen, "Self-trapping and flipping of double-charged vortices in optically induced photonic lattices," Opt. Lett. **31**, 2456 (2006).
24. G. Bartal, O. Cohen, H. Buljan, J. W. Fleischer, O. Manela, and M. Segev, "Brillouin zone spectroscopy of nonlinear photonic lattices," Phys. Rev. Lett. **94**, 163902 (2005).
25. D. Träger, R. Fischer, D. N. Neshev, A. A. Sukhorukov, C. Denz, W. Krolikowski, and Y. S. Kivshar, "Nonlinear Bloch modes in two-dimensional photonic lattices," Opt. Express **14**, 1913 (2006).
26. R. Fischer, D. Träger, D. N. Neshev, A. A. Sukhorukov, W. Krolikowski, C. Denz, and Y. S. Kivshar, "Reduced-symmetry two-dimensional solitons in photonic lattices," Phys. Rev. Lett. **96**, 023905 (2006).
27. J. Yang, I. Makasyuk, A. Bezryadina, and Z. Chen, "Dipole solitons in optically induced two-dimensional photonic lattices," Opt. Lett. **29**, 1662 (2004).
28. J. Wang and J. Yang, "Families of vortex solitons in periodic media," Phys. Rev. A **77**, 033834 (2008).
29. M. Öster and M. Johansson, "Stable stationary and quasiperiodic discrete vortex breathers with topological charge S=2," Phys. Rev. E **73**, 066608 (2006).
30. E. A. Ostrovskaya, T. J. Alexander, and Y. S. Kivshar, "Generation and detection of matter-wave gap vortices in optical lattices," Phys. Rev. A **74**, 023605 (2006).

Optical waves propagating in nonlinear waveguide arrays and photonic lattices have attracted a great deal of interest [1, 2]. One of the key paradigms of discretizing light behavior in periodical structures is the self-trapped states better known as "lattice solitons" [3-8]. Such discrete spatial solitons typically have their propagation constants residing in the semi-infinite gap (arising from the total internal reflection) or inside a true photonic band gap (arising from the Bragg reflection). Although gap solitons were traditionally considered as a temporal phenomenon in one-dimensional (1D) periodic media, spatial gap solitons in both 1D and 2D configurations have been demonstrated recently in a number of experiments with either a self-focusing or a self-defocusing nonlinearity [5, 6, 9-12].

Optical vortex solitons propagating in periodic media form another family of discrete spatial solitons with helical phase structures, as have been predicted earlier [13, 14] and demonstrated in optical induced lattices with a self-focusing nonlinearity [15, 16]. These are semi-infinite-gap vortex solitons. Gap vortex solitons with their propagation constants located inside a photonic bandgap have only been observed so far with a self-focusing nonlinearity where the vortex solitons bifurcate from the band edge of the second band, thus named as second-band vortex solitons [17]. To our knowledge, gap vortex solitons in self-defocusing lattices have never been demonstrated, although they have been predicted in theory to exist as spatially localized topological states in Bose-Einstein Condensates confined by an optical lattice [18] as well as in photorefractive optically-induced photonic lattice [19, 20].

In this paper we report the first experimental demonstration of self-trapping of both single- and double-charged vortex beams by on-axis excitation in a "backbone" photonic lattice induced with a saturable self-defocusing nonlinearity. We show that, under proper nonlinear conditions, a single-charged (m=1) vortex beam can evolve into a gap vortex soliton, while a double-charged (m=2) vortex beam tends to turn into a self-trapped quadrupole-like structure. The spatial power spectra and interferograms (with a tilted plane wave) of the self-trapped vortices from both experiments and numerical simulations are presented, and the stability of the vortex solitons is also studied numerically. Our results show that the gap vortex soliton does not bifurcate from the edge of the first Bloch band, quite different from all previously observed fundamental, dipole or quadrupole spatial gap solitons.

The experimental setup for our study is similar to those used earlier for observation of discrete (semi-infinite gap) vortex solitons in self-focusing lattices [15], except that we now use a self-defocusing nonlinearity to induce the waveguide lattices [12, 21]. The lattice is induced in a photorefractive SBN crystal ($5\times10\times5$ mm^3) by a spatially modulated partially coherent light beam sent through an amplitude mask. The mask is appropriately imaged onto the input face of the crystal, creating a periodic input intensity pattern for lattice induction. The lattice period is about 27 μm. With a negative bias voltage, the intensity pattern induces a "backbone" waveguide lattice, as the crystal turns into a defocusing nonlinear medium [22]. The vortex beam is generated by sending a coherent laser beam through a computer generated vortex hologram. In all experiments, the lattice beam is ordinarily-polarized while the vortex beam is extraordinarily-polarized. Thus the lattice beam will undergo nearly linear propagation in the crystal while the vortex beam will experience a large nonlinearity due to the anisotropic property of the photorefractive crystal [5-8]. An incoherent white light source was used as a background illumination to fine tune the screening nonlinearity. The output beam patterns and Fourier spectra are monitored with CCD cameras. The vortex beam exiting the crystal is also sent into a Mach-Zehnder interferometer for phase measurement as needed.

In our experiment, the off-site excitation scheme is used so that the vortex core is on an index minimum while the donut-like vortex beam covers four adjacent index maxima. To open the first Bragg reflection gap (between the first and second Bloch bands), a relatively high lattice beam intensity and bias field is employed for induction of a deep lattice potential [12, 21]. By fine-tuning the nonlinearity (through the bias field and the lattice-to-background intensity ratio), self-trapping of the vortices can be established. Typical experimental results are presented in Fig. 1, for which the intensity ratio of the vortex beam to the lattice beam is about 1:4, and the bias field is about -1.2 kV/cm. The interferograms of the input vortex beams with a tilted plane wave are shown in Fig. 1(a), where the central fork resulting from the fringe bifurcation indicates the phase singularity (m=1 for top panels, and m=2 for bottom panels) of the vortex beam. When self-trapping is established in the nonlinear regime, both m=1 and m=2 vortices assume an intensity pattern primarily consisting of four spots [Fig. 1(b)], similar to the semi-infinite-gap vortex solitons [15, 16]. Along the directions of the principal axes of the square lattice (which are oriented diagonally rather than horizontally and vertically), long "tails" beyond the central four spots can be seen. Although the intensity patterns of self-trapped m=1 and m=2 vortices look somewhat similar, significant differences can be found in their phase structure and spatial spectrum.

First, we use two different interference techniques to identify the phase structure of self-trapped vortices as used earlier for vortices in self-focusing lattices [23]. One is to send a tilted broad beam (quasi-plane wave) to interfere with the output vortex beam [Fig. 1(c)]. For the limited propagation distance of our crystal length (10 mm), it appears that the vortex singularity (manifested by the central fork in the interferograms) persists after the nonlinear propagation through the crystal, although it seems that charge-flipping (reversal of forks) is associated with the m=2 but not the m=1 vortices at the crystal output. However, as shown below from numerical simulations to longer propagation distance, the singularity can maintain only for the m=1 but not for the m=2 vortices. In fact, our theoretical analysis shows that a "true" double-charged gap vortex soliton does not exist under this excitation condition, and a quadrupole-like soliton structure is found instead for the m=2 vortex. The other technique is to send a co-axial broad Gaussian beam as an interfering beam. We can see clearly that the phase structures for self-trapped m=1 and m=2 vortices are different [Fig.1 (d)]. The two diagonal spots are out-of-phase for the m=1 vortex but in-phase for the m=2 vortex, similar to self-trapped vortices in self-focusing photonic lattices [15, 16, 23].

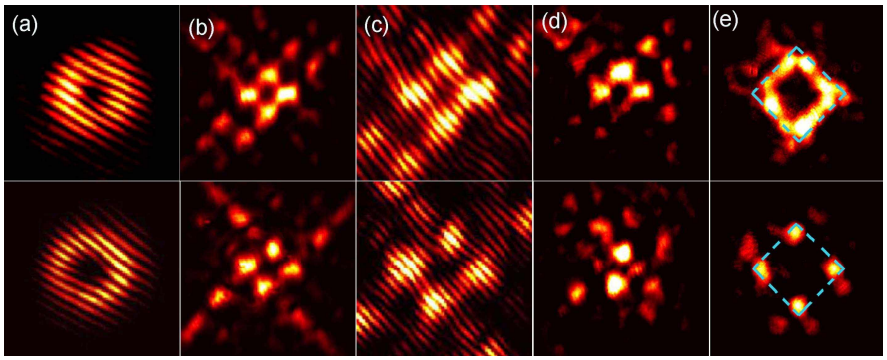

Fig. 1. Experimental results of self-trapping of single-charged (top) and double-charged (bottom) vortices in a defocusing photonic lattice. (a) Interferograms showing the phase of the input vortex beams, (b) intensity patterns of self-trapped vortex beams at lattice output, (c, d) interferograms between (b) and a tilted plane wave (c) and an on-axis Gaussian beam (d), respectively, and (e) the k-space spectra of (b) where the dash squares mark the first Brillouin-zone of the square lattice. (a, c) are zoomed in with respect to (b, d) for better visualization.

Next, we measure the spatial spectrum of self-trapped vortices [Fig. 1(e)] by using the technique of Brillouin Zone (BZ) Spectroscopy [24]. Again, dramatic differences between m=1 and m=2 vortices can be seen in these k-space spectra, indicating quite different physical pictures for self-trapping. For the m=1 vortex, most of the power is located alongside the first BZ, but it would not concentrate just to the four corner points (corresponding to four high-symmetry M points) which mark the edge of the first Bloch band and where the diffraction is anomalous [6, 25]. For the m=2 vortex, however, the nonlinear spectrum reshaping makes the power spectrum settle into the M-points quickly, similar to those of the fundamental gap solitons and gap soliton trains [12]. Numerical simulations (see below) show that such spectrum difference remains for long propagation distance. These results suggest that although the m=1 vortex can evolve into a gap vortex soliton, it does not bifurcate from the edge of the first Bloch band, quite different from all previously observed fundamental, dipole or quadrupole-like gap solitons in self-defocusing lattices [6, 12, 21]. It is also significantly different from the second-band gap vortex solitons [17] or the reduced-symmetry gap solitons [26] in self-focusing lattices, which all bifurcate from the edge of the second band. On the other hand, the m=2 vortex can evolve into a quadrupole-like localized state, which does seem to bifurcate from the edge of the first Bloch band as confirmed by numerical analysis below. We would like to mention that in Fig. 1 we did not show the linear output of the vortex beams simply due to that the linear output pattern does not differ significantly as compared to the nonlinear output of Fig. 1(b) in our experiment. This is because the induced lattice potential is deep (for opening the first gap [12, 21]) and the length of our photorefractive crystal is only 10 mm so the vortex beam does not exhibit strong discrete diffraction as clearly seen in our simulations to longer propagation distances. However, the experimentally measured phase and spectrum of the linear output are apparently different from those of nonlinear output. In the linear region, all adjacent intensity peaks from the vortex beam have an in-phase relationship and the power spectrum covers the entire first BZ with most of the energy concentrated in the center of the BZ.

We now compare the above experimental observations with our numerical results obtained using beam propagation simulations with the initial condition similar to that for the experiment. The numerical model is a nonlinear wave equation with a 2D square lattice potential under self-defocusing photorefractive nonlinearity [6, 27]. Figure 2 shows the typical simulation results corresponding to experimental results of Fig. 1. Excellent agreement can be seen for the 10 mm of propagation distance (i.e. our crystal length) for both m=1 and m=2 vortices. In particular, even for only 10 mm of propagation, clear differences can be seen in

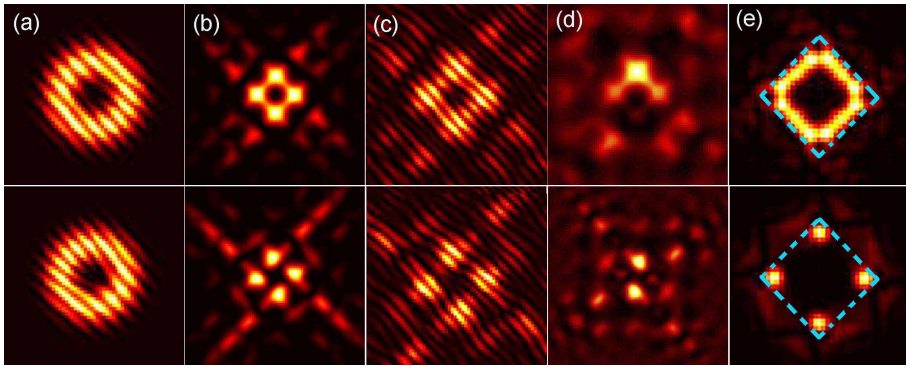

Fig. 2. Numerical results of self-trapping of single-charged (top) and double-charged (bottom) vortices in a defocusing photonic lattice corresponding to experimental results of Fig. 1. The propagation distance is 10 mm corresponding to the length of the crystal used in experiment.

the phase structure [Fig. 2(c, d)] and k-space power spectrum [Fig. 2(e)], as observed in our experiments (Fig. 1). To examine whether the relevant gap soliton structures can persist for longer propagation distances, simulations are also performed with a propagation distance up to 40 mm while all other parameters are left unchanged. The results are shown in the left panels of Fig. 3. Indeed, the corresponding intensity patterns are found to be nearly unchanged even after 40 mm of propagation. However, by interfering the vortex beam with a titled plane wave to observe the phase structure, a major difference is noticed after 40-mm of propagation: while the fork is still in the center of the interferogram for the m=1 vortex (hence showing that the m=1 gap vortex can maintain its helical phase structure), this is not the case for the m=2 vortex. In the latter case, the forks in the center disappear gradually and the vorticity is eventually lost. In fact, the m=2 vortex loses its original angular momentum and transforms itself into a quadrupole-like structure. Before the vorticity completely disappears, a transient state of charge flipping is found from our detailed simulations, but unlike the periodical appearance of m=2 and m=-2 vortices found in the self-focusing case [23], the m=2 vortex singularity cannot maintain in self-defocusing lattices, and the vortex disintegrate into an unstable quadrupole-like structure. (In the self-focusing case, the quadrupole appears only as a transient state for charge flipping of the m=2 vortex under the isotropic photorefractive lattice potential [23]). This dynamical evolution can be seen more clearly in the 3D plot of beam propagation illustrated in the right panels of Fig. 3. Furthermore, our numerical simulations to longer propagation distance also indicate that the tails of the self-trapped m=2 vortex have wave properties typical to Bloch modes located in the vicinity of the first-band M point (being out-of-phase between adjacent sites along directions of the lattice principal axes [25]). This is consistent with the k-space power spectrum that settles onto four M points, indicating that the m=2 vortex evolves into a gap quadrupole soliton bifurcated from the edge of the first Bloch band. On the other hand, similar simulations to 40-mm propagation distance for the m=1 vortex does not show this well-defined phase relation in the tails [Fig. 3(a)], as some neighboring sites are in-phase and some are out-of-phase along directions of the lattice principal axes. The power spectrum concentrates more into the four sides of the first BZ rather than evolves into a well-defined four M-point spectrum as in Fig. 3(b), suggesting that the m=1 gap vortex soliton does not bifurcate from the edge of the first Bloch band.

Finally, we investigate the stability of both m=1 and m=2 self-trapped vortices by means of linear stability analysis for typical parameters corresponding to experimental observations. Our analysis shows that, indeed, the m=1 vortex gap soliton is stable almost throughout the first gap of the defocusing lattice, while the quadrupole gap state is always linearly unstable. Since the latter instability growth rate is relatively small, the quadrupolar structure is observable for certain propagation distances, as demonstrated in our experiment and numerical simulations. The soliton solutions (in real and Fourier space) and the corresponding

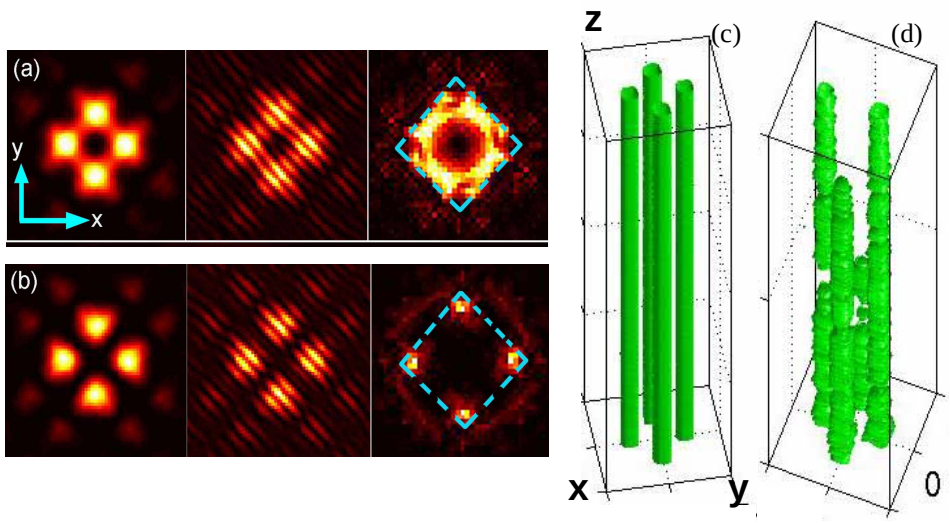

Fig. 3. Simulation results of single-charged (a) and double-charged (b) vortex beams propagating to a longer distance of 40 mm. Left panels show the output transverse (x-y) intensity pattern (left), its interferogram with a titled plane wave (middle), and its k-space spectrum (right) in both (a) and (b). Notice that the vortex singularity maintains in (a) but disappears in (b). Right panels show the propagation of a stable m=1vortex beam (c) and of an unstable quadrupole beam as arising from the breakup of m=2 vortex (d) long the longitudinal z-direction (from bottom to top) through the defocusing lattice.

maximal growth rates [maximum real part Re(λ) of the linearization eigenvalues] as a function of the propagation constant μ are illustrated in Fig 4, where regions of zero growth rate (Max[Re(λ)]=0) indicate the good stability of the gap soliton solutions. We note again that, as seen in Fig. 4 (right panels), while the unstable quadrupolar structure seems to bifurcate from a linear Bloch mode of the first band, the same is not true for the m=1 gap vortex soliton, as the latter stability (and corresponding existence) curve appears to have a turning point before reaching the band edge. Results from our experimental observation and numerical analysis are in good agreement with recent theoretical work on the families of the m=1 gap vortex solitons in periodic media [28], where it also shows that the single-charged vortex families do not bifurcate from edges of Bloch bands, but rather they turn back and move into band gaps before reaching band edges. Although such non-edge bifurcation of vortex gap solitons can be found from the mathematical model of nonlinear propagation of vortices in 2D periodic media, it seems that the underlying physical mechanism for the emergence of such "purely nonlinear" states merits further investigation. Intuitively, this might be attributed to the nontrivial helical phase structure of the vortex, which cannot be expressed as a simple superposition of linear Bloch modes near the band edge. A related interesting issue is to explore the existence and maybe to experimentally demonstrate the genuine m=2 gap vortex solitons with different excitation conditions, such as those gap vortex states proposed in [29]. Although the gap vortices in periodic structures have been previously proposed in literatures [18, 28, 30], the theoretical analysis presented here with a model involving a saturable self-defocusing nonlinearity is particularly relevant to our experiments and helpful for a good understanding of the experimental observations. Furthermore, the features of the nonlinear spectrum reshaping and instability analysis which have not been illustrated before will stimulate further theoretical study of spatial gap vortex solitons in periodic systems beyond optics.

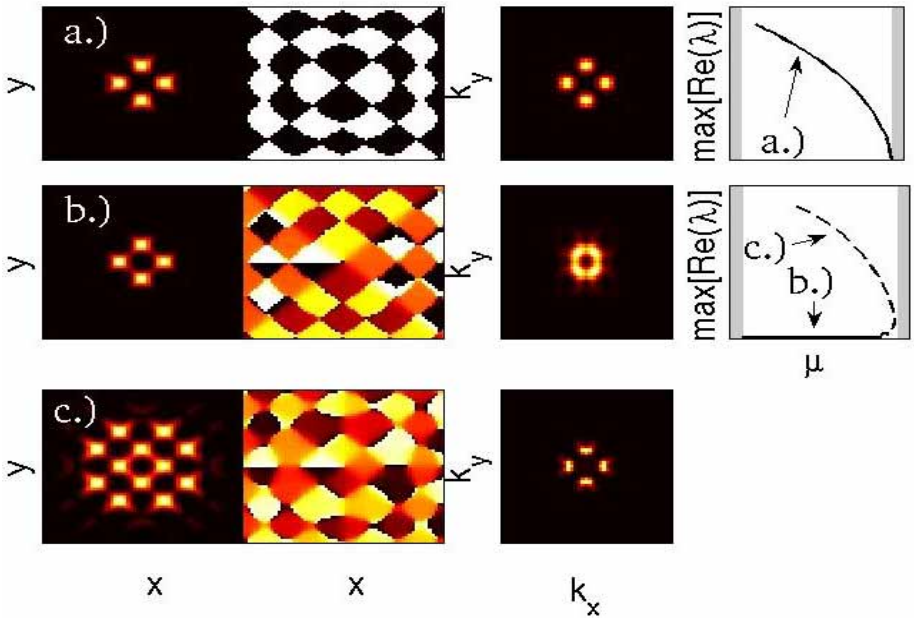

Fig 4. Numerical solutions of self-trapped quadrupole [a.)] and single-charged vortices [b.) and c.)]. Shown are typical stationary patterns (first column), corresponding phase structure (second column), Fourier spectra (third column), and maximal instability growth rates (fourth column). Plots in fourth column are given as a function of the propagation constant μ, while the spectral bands are denoted by shaded areas. The first Bloch band is located to the right, where for the single-charged vortex family the stable node branch [solid line, b.)] collides with the unstable saddle branch [dashed line, c.)] before reaching the band edge. Zero growth rates indicate that the self-trapped structure is linearly stable.

In conclusion, we have demonstrated self-trapping of both single- and double-charged vortex beams in optically induced photonic lattices with a self-defocusing nonlinearity. We have shown that only the single-charged vortex beam can evolve into a gap vortex soliton which does not bifurcate from the band edge, while the double-charged vortex eventually reshapes into a quadrupole-like gap soliton which does bifurcate from the edge of the Bloch band. The single-charged vortex gap soliton can be linearly stable under certain conditions while the double-charged vortex tends to break up into a quadrupole-like structure which is linearly unstable. Our experimental results are corroborated by numerical simulations.

Acknowledgments

This work was supported by the 973 program, NSFC, PCSIRT, NSF, AFOSR, and the Humboldt Foundation. We thank D. Neshev, J. Yang, and Z. Peng for discussions.